

# UC San Diego

## UC San Diego Electronic Theses and Dissertations

### Title

An extended finite element formulation for contact in multi-material arbitrary Lagrangian-Eulerian calculations

### Permalink

<https://escholarship.org/uc/item/1fr314x9>

### Author

Vitali, Efrem

### Publication Date

2007

Peer reviewed|Thesis/dissertation

UNIVERSITY OF CALIFORNIA, SAN DIEGO

**An extended finite element formulation for contact in multi-material  
arbitrary Lagrangian-Eulerian calculations**

A dissertation submitted in partial satisfaction of the  
requirements for the degree

Doctor of Philosophy

in

Engineering Sciences (Mechanical Engineering)

by

Efrem Vitali

Committee in charge:

Professor David J. Benson, Chair  
Professor Petr Krysl  
Professor Enrique J. Luco  
Professor Marc A. Meyers  
Professor Hidenori Murakami

2007

Copyright

Efrem Vitali, 2007

All rights reserved.

The dissertation of Efrem Vitali is approved, and  
it is acceptable in quality and form for publication  
on microfilm:

---

---

---

---

---

Chair

University of California, San Diego

2007

To the memory of my father Vittorio

## TABLE OF CONTENTS

Signature Page . . . . .	iii
Dedication . . . . .	iv
Table of Contents . . . . .	v
List of Figures . . . . .	vii
List of Tables . . . . .	ix
Acknowledgments . . . . .	x
Vita and Publications . . . . .	xi
Abstract of the Dissertation . . . . .	xii
Chapter I Introduction . . . . .	1
I.A History of the Finite Element Method . . . . .	2
I.B Finite Element Method . . . . .	3
I.B.1 Lagrangian and Eulerian formulations . . . . .	3
I.B.2 eXtended Finite Element Method . . . . .	4
I.C Motivation . . . . .	5
I.D Objective . . . . .	6
Chapter II Eulerian Formulation . . . . .	9
II.A Operator Splitting . . . . .	9
II.B Lagrangian Step . . . . .	11
II.B.1 Time integration . . . . .	11
II.B.2 Constitutive equations . . . . .	12
II.C Eulerian Step . . . . .	15
II.C.1 Transport . . . . .	15
II.C.2 Interface reconstruction . . . . .	20
Chapter III Mixture Theories . . . . .	22
III.A Requirements . . . . .	23
III.B Mean Strain Rate . . . . .	23
III.C Pressure and Stress Equilibration . . . . .	25
III.D Contact . . . . .	27
III.D.1 Fully bonded . . . . .	28
III.D.2 Frictionless slip . . . . .	28
III.D.3 Slip with friction . . . . .	29
III.E Separation . . . . .	29

Chapter IV eXtended Finite Element Formulation for MMALE Calculations . . .	30
IV.A Independent Fields . . . . .	31
IV.B Independent Deformations . . . . .	33
IV.C Dependent Deformations . . . . .	34
IV.C.1 Velocity and Acceleration Coupling . . . . .	36
IV.C.2 Nodal Normals . . . . .	42
IV.C.3 Contact Enforcement . . . . .	56
Chapter V Numerical Results . . . . .	66
V.A Bouncing Cylinder . . . . .	67
V.A.1 Example 1 . . . . .	67
V.A.2 Example 2 . . . . .	76
V.B Sliding Block . . . . .	80
V.C Taylor Anvil Test . . . . .	87
V.D Projectile Penetration . . . . .	100
V.E High Velocity Shock Compression of a Steel Powder . . . . .	104
Chapter VI Conclusions and Future Work . . . . .	108
VI.A Summary and Conclusions . . . . .	108
VI.B Future Work . . . . .	109
Bibliography . . . . .	111

## LIST OF FIGURES

Figure II.1:	Lagrangian and Eulerian Steps . . . . .	10
Figure II.2:	Transport concept: one-dimensional example . . . . .	16
Figure II.3:	Linear distribution of $\phi$ in element $E$ . . . . .	17
Figure II.4:	Slopes considered for the linear distribution . . . . .	19
Figure II.5:	Sweeping concept: two-dimensional example . . . . .	20
Figure II.6:	Two dimensional interface tracking scheme . . . . .	21
Figure IV.1:	Overlapping of two materials with independent mesh . . . . .	31
Figure IV.2:	Independent deformation of two materials . . . . .	33
Figure IV.3:	Materials interference . . . . .	35
Figure IV.4:	Nodal support with two materials . . . . .	37
Figure IV.5:	Mixed element normals . . . . .	44
Figure IV.6:	Scheme for intra-element normals . . . . .	45
Figure IV.7:	Elements used to locate the materials at the bottom intra-element interface . . . . .	47
Figure IV.8:	Examples of intra-element interfaces . . . . .	48
Figure IV.9:	Particular cases where the material locator algorithm is inaccurate	49
Figure IV.10:	Examples of nodal support interfaces . . . . .	52
Figure IV.11:	Two colliding materials . . . . .	55
Figure IV.12:	Interface and pairs of elements in nodal support $A$ . . . . .	60
Figure V.1:	Bouncing Cylinder: initial conditions . . . . .	68
Figure V.2:	Bouncing Cylinder: pre-impact (Mixture Theory) . . . . .	69
Figure V.3:	Bouncing Cylinder: pre-impact (X-FEM) . . . . .	70
Figure V.4:	Bouncing Cylinder: full-impact (Mixture Theory) . . . . .	71
Figure V.5:	Bouncing Cylinder: full-impact (X-FEM) . . . . .	73
Figure V.6:	Bouncing Cylinder: separation (Mixture Theory) . . . . .	74
Figure V.7:	Bouncing Cylinder: separation (X-FEM) . . . . .	75
Figure V.8:	Bouncing Cylinder: maximum contact (Mixture Theory) . . . . .	78
Figure V.9:	Bouncing Cylinder: maximum contact (X-FEM) . . . . .	79
Figure V.10:	Sliding Block: initial conditions . . . . .	80
Figure V.11:	Sliding Block: begin calculation . . . . .	82
Figure V.12:	Sliding Block: final condition . . . . .	83
Figure V.13:	Sliding Block: gap between materials with IIVF = 5% . . . . .	85
Figure V.14:	Sliding Block: gap between materials with IIVF = 1% . . . . .	86
Figure V.15:	Taylor Anvil Test: initial conditions . . . . .	87
Figure V.16:	Taylor Anvil Test: frictionless (Mixture Theory) . . . . .	89
Figure V.17:	Taylor Anvil Test: frictionless (X-FEM) . . . . .	90
Figure V.18:	Taylor Anvil Test: frictionless (LS-DYNA) . . . . .	91
Figure V.19:	Taylor Anvil Test: fully bonded (X-FEM) . . . . .	92
Figure V.20:	Taylor Anvil Test: fully bonded (LS-DYNA) . . . . .	93
Figure V.21:	Taylor Anvil Test: 0.75 friction (X-FEM) . . . . .	94
Figure V.22:	Taylor Anvil Test: 0.75 friction (LS-DYNA) . . . . .	95
Figure V.23:	Taylor Anvil Test: 0.5 friction (X-FEM) . . . . .	96



Figure V.24: Taylor Anvil Test: 0.5 friction (LS-DYNA) . . . . .	97
Figure V.25: Taylor Anvil Test: 0.25 friction (X-FEM) . . . . .	98
Figure V.26: Taylor Anvil Test: 0.25 friction (LS-DYNA) . . . . .	99
Figure V.27: Projectile Penetration: initial conditions . . . . .	100
Figure V.28: Projectile Penetration (Mixture Theory) . . . . .	102
Figure V.29: Projectile Penetration (X-FEM) . . . . .	103
Figure V.30: Steel Powder: initial conditions . . . . .	104
Figure V.31: Steel Powder: shock compression . . . . .	105
Figure V.32: Steel Powder: total, internal, and kinetic energies . . . . .	106

## LIST OF TABLES

Table I.1:	Overlapping of two materials with independent mesh . . . . .	7
Table V.1:	Bouncing Cylinder: material constants . . . . .	68
Table V.2:	Sliding Block: material constants . . . . .	81
Table V.3:	Taylor Anvil Test: material constants . . . . .	88
Table V.4:	Projectile Penetration: material constants . . . . .	101
Table V.5:	Steel Powder: material constants . . . . .	107

## ACKNOWLEDGMENTS

I wish to express my gratitude to Professor David Benson for his guidance, understanding, and limitless patience, which allowed me to learn from my mistakes and become a more independent researcher. It was thank to his ideas that this work started, and it has been a privilege being one of his students.

I am grateful to Professor Marc Meyers, Professor Hidenori Murakami, Professor Enrique Luco, and Professor Petr Krysl for serving on my committee and providing valuable suggestions.

I wish to thank Dr. Nathan Barton for his friendship and for his help during his time as a post-doctoral researcher here at the University of California San Diego. I am also thankful to Dr. Parag Dixit for his help in proofreading this work.

I feel fortunate to have been part of the Mechanical and Aerospace Engineering department at the University of California San Diego. During my journey I met many incredible people among faculty and staff that helped me with my questions and concerns; I wish to thank them all.

I am also indebted to the Army Research Office that made this achievement possible by funding my studies and research.

Lastly, but not in order of importance, I wish to thank my mom Jacqueline, my sister Monica, and my brother in law Stefano; their constant love and support certainly contributed to my accomplishment.

## VITA

- 1997 B. S., Mechanical Engineering,  
University of Applied Sciences Biel, Switzerland
- 1998–1999 Mechanical Engineer, R&D Department,  
New Automatic Machine Company S.A., Switzerland
- 1999–2000 Mechanical Engineer, R&D Department,  
Borra S.A., Switzerland
- 2001 Teaching Assistant, Department of Engineering,  
San Francisco State University
- 2002 Instructor, Department of Engineering,  
San Francisco State University
- 2002 Graduate Researcher, Department of Engineering,  
San Francisco State University
- 2003 M. S., Engineering (Mechanical Engineering),  
San Francisco State University
- 2005 Teaching Assistant,  
Department of Mechanical and Aerospace Engineering,  
University of California at San Diego
- 2007 Teaching Assistant,  
Department of Mechanical and Aerospace Engineering,  
University of California at San Diego
- 2003-2007 Graduate Researcher,  
Department of Mechanical and Aerospace Engineering,  
University of California at San Diego
- 2007 Ph. D., Engineering Sciences (Mechanical Engineering),  
University of California at San Diego

## PUBLICATIONS

Vitali E, and Benson D. An extended finite element formulation for contact in multi-material arbitrary Lagrangian-Eulerian calculations. *International Journal for Numerical Methods in Engineering* 2006; **67**(10):1420–1444.

ABSTRACT OF THE DISSERTATION

**An extended finite element formulation for contact in multi-material  
arbitrary Lagrangian-Eulerian calculations**

by

Efrem Vitali

Doctor of Philosophy in Engineering Sciences (Mechanical Engineering)

University of California San Diego, 2007

Professor David J. Benson, Chair

A contact method for the multi-dimensional Lagrangian step in multi-material arbitrary Lagrangian-Eulerian (ALE) formulations is presented. The extended finite element method (X-FEM) is used to create independent fields (i.e. velocity, strain rate, force, mass, etc.) for each material in the problem. The accelerations of the multi-material nodes are obtained by coupling the material force and mass fields as a function of the prescribed contact; similarly, the velocities of the multi-material nodes are recalculated using the conservation of momentum when the prescribed contact requires it. The coupling procedures impose the same nodal velocity on the coupled materials in the direction normal to their interface during the time step update. As a result, the overlap of materials is prevented and unwanted separation does not occur. Three different contacts are treated: perfectly bonded, frictionless slip, and slip with friction. Example impact problems are solved and the numerical solutions are presented.

# Chapter I

## Introduction

The finite element method (FEM) is a numerical method for simulating the physical behavior of continuum bodies. For instance, if the boundary conditions and the material properties of a body are known, the finite element method can compute the stress distribution in a body. This method provides only approximate solutions, however, it is a powerful tool in the treatment of geometrically complex bodies where exact analytical solutions are rarely available. The finite element method is based on approximate solution methods for partial differential equations; the foundations of this method were developed in the first half of the twentieth century [2, 3, 4, 5], however, it was in the second half of that century that the method received broad attention from the scientific and industrial communities due to the invention of digital computers.

The study of contact between materials undergoing non-linear large deformations caused by high strain rates is a current area of research.

## I.A History of the Finite Element Method

The finite element method (FEM) origins can be traced back to the late 19th century. In 1877 Rayleigh [1] applied the available minimization of energy principles to solve structural design problems. Some thirty two years later, Ritz [2] extended the theory by introducing multiple independent functions. In 1915, Galerkin [3] published the method of weighted residuals, which is the foundation of the modern finite element method. By 1941, structural engineers had applied the force-displacement knowledge of bars and beams to solve truss problems. The same year, Hrennikoff [4] began to expand the concept to continuum mechanics. His work on the frame-work method consists of replacing a continuum body with a finite number of bars that express the mechanical properties of the body; the structure of bars is then solved as a truss problem. In 1943 Courant used the work of Ritz to analyze the St. Venant torsion problem [5]. He is credited for the introduction of piecewise continuous functions over a continuum body that was discretized into triangular elements. In 1956, Turner, Clough, Martin, and Topp [6] used triangular elements to obtain the solution of plane stress problems. Their work produced the direct stiffness method, and four years later the nomenclature “finite element method” appears on a paper published by Clough [7]. These successful attempts captured the attention of the engineering and scientific communities, and the finite element method increased in popularity. In 1965 the necessity of greater computer power to solve large matrices was stressed in a conference held at Wright-Patterson Air force base [10]. Soon after this event, as computing power increased and the FEM theory developed, the first commercial code named NASA STRUCTURAL ANALYSIS (NASTRAN) was available. Other commercial codes such as SAP and ANSYS followed [32, 27].

Since then the finite element method, along with computational resources, has been growing to address the various scientific and industrial needs. The aerospace, nuclear, automotive, metal processing, golf, cellphone industries are just few examples of sectors currently using FEM.

## I.B Finite Element Method

The analysis of a continuum body with the finite element method begins with the discretization of the body (or domain). The body is divided (or discretized) into small regions called elements, and each element is defined by a set of points (or nodes) that are shared with the adjacent elements. Each node has one interpolation functions (or shape function)  $\psi_A(\mathbf{x})$ , and these shape functions have to guarantee continuity throughout the entire body. As a result, an approximate function that describes the behavior of a variable over the body is obtained by combining the variable's nodal values with the respective shape functions,  $\phi(\mathbf{x}) = \sum_A \phi_A \psi_A(\mathbf{x})$ . The solution to a given problem is obtained by: 1) introducing the approximate function into the weak form of the appropriate conservation equations, 2) applying the prescribed initial and boundary conditions, and 3) solving for the nodal unknowns.

### I.B.1 Lagrangian and Eulerian formulations

The finite element method is usually applied to the conservation equations in either the Lagrangian or Eulerian form. In the Lagrangian formulation the mesh is tied to the material and the elements move and distort with it. As a consequence, the time derivative of the approximate function is  $\dot{\phi}(\mathbf{x}) = \sum_A \dot{\phi}_A \psi_A(\mathbf{x})$ . In the Eulerian



formulation the mesh is fixed in space and the material flows through the mesh. As a result, the time derivative of the approximation function introduces a transport term requiring further calculations.

Discretizing problems such that each element contains a single material is an advantage for Lagrangian formulations. In Eulerian formulations, however, the transport term causes materials to flow in and out of the elements, and as a consequence, Eulerian formulations need an algorithm to track the material interfaces.

In Lagrangian formulations, the mesh can deform considerably when bodies undergoing large deformations are studied. Therefore, elements can reach zero or negative volume resulting in element failure. This does not occur in Eulerian formulations since the mesh, being fixed in space, is not conditioned by the amount of deformation.

Contact problems, for instance two body separating or colliding, present more challenges. Lagrangian formulations increase in complexity when new interfaces need to be created or contact conditions must be enforced. However, the transport algorithm of Eulerian formulation automatically satisfies these requirements.

### **I.B.2 eXtended Finite Element Method**

The extended finite element method (X-FEM) was developed by Belytschko et al. [22, 24, 26, 28, 31, 33, 37] in the 1990s to solve problems with discontinuities within elements. For example, Belytschko used this method in Lagrangian formulations to solve fracture mechanics problems [22, 26, 28, 31]. Each discontinuity in an element requires the addition of a set of extra degrees of freedom to the element's nodes, which are associated to an enrichment function. The enrichment function is chosen based on

the type of discontinuity present in the element. For instance, a Heavyside function can be used to describe a crack that cuts an element in two, and asymptotic functions can be used to describe the behavior of an element containing a crack tip [28].

## **I.C Motivation**

In the past, trial and error methods in the laboratory were used to study the behavior of materials and structures. With the advent of the finite element method, much of the laboratory testing has been replaced by computer simulations, considerably reducing the testing time and costs. Moreover, the ability to simulate the behavior of complex shapes provides a more accurate and detailed analysis of the problem. The finite element method can solve a wide range of problems such as: static loading, dynamic loading, fracture mechanics, impact, thermodynamics, etc. This research focuses on non-linear deformations found in high strain rate contact problems (e.g. high velocity impacts).

Contact problems involving high strain rate deformations are common in various scientific and industrial fields. For instance, an active field of research in material science aims to improve bulletproof vests by developing new materials and structures. A finite element analysis can provide valuable information for this problem, such as material fragmentation and energy dissipation. In the transportation industry, vehicles (e.g. cars, trains, helicopters, etc.) must satisfy prescribed impact tests (or crash tests) before they can be sold. Computer simulations can spot structural weaknesses at the development stage, and the design can be improved before production. Another example is found in the metal stamping industry where products are obtained by striking a die

on a sheet of metal placed on another die. The sheet of metal undergoes large plastic deformations and the design of the dies is critical to obtain the required properties such as the product thickness. The behavior of the metal during the stamping can be reproduced with a finite element model and the dies can be modified beforehand. The finite element method is also very valuable when used in projects that employ expensive materials such as titanium. Moreover, it can simulate problems at magnitudes and environments where laboratory testing is difficult due to the limitations of data acquisition devices, for instance, applying strain gauges at the micrometer magnitude, or operating devices at  $-164\text{ }^{\circ}\text{F}$  (i.e. average temperature on Mars).

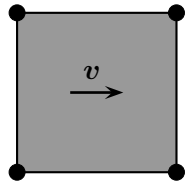
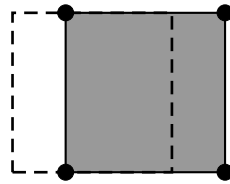
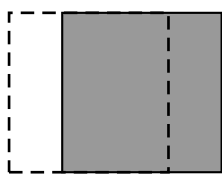
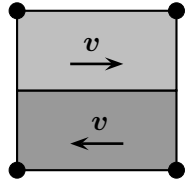
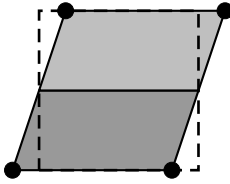
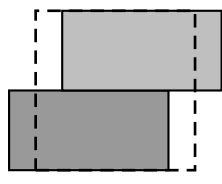
## I.D Objective

Multi-material Eulerian formulations were initially introduced to solve hydrodynamic problems. Their ability to solve non-linear large deformation problems and automatically generate new interfaces make these formulations very attractive for solving solid mechanics problems. Eulerian codes, by their nature, require a relatively elaborate interface tracking. However, the biggest challenge resides in the development of a contact formulation, which has to describe the materials' behavior in elements containing two or more materials (or multi-material elements). Little work has been done in this direction and the literature is scarce. The main contribution in this field is attributed to Benson [18, 20, 21] with his pioneering work on contact mixture theories. Mixture theories have proved to work well with multi-material problems that have fully bonded interfaces between materials. However, there are limitations on these theories when the frictionless slip or slip with friction are required. The failure to correctly model the behavior of

these contact types is due to a single velocity field across all the materials. Consider the four node rectangular element displayed in table I.1 example a), the element contains one material with a horizontal rigid body displacement. Since the finite element method uses the movement of the element's nodes to describe the displacement of the material, the four nodes will move in the same horizontal direction and by the same amount. In this case, the prediction agrees with the expected result. Now consider the element containing two materials in example b), where one material fills the bottom half and a second material fills the top half. In addition, the two materials have a horizontal rigid body motion opposite with respect to each other. In this example, the element is unable to express both movements since the nodes, having one set of degrees of freedom, can describe the rigid body motion of only one material. As a consequence, the prediction differs from the expected result, and errors, such as shear stress, are introduced in the formulation.

The objective of this research is to develop a contact algorithm for Eulerian formu-

Table I.1: Overlapping of two materials with independent mesh

	<b>Problem</b>	<b>Prediction</b>	<b>Expected</b>
a)			
b)			

lations that overcomes the problems encountered in the mixture theories. The contact algorithm must handle the following contact types: fully bonded, frictionless slip, and slip with friction. In order to counter the mixture theory problems, additional degrees of freedom for each material are assigned to the nodes having more than one material in their support (i.e. multi-material nodes), where the nodal support is defined as the elements connected to the node. The new algorithm is integrated into Raven, a multi-material Eulerian research code developed at UCSD.

Chapter II offers an overview of the Eulerian formulation, where the conservation equations are separated into a Lagrangian step and an Eulerian step by operator splitting. The Lagrangian step section describes the time integration and reviews some of the constitutive equations. The material transport and the interface reconstruction is presented in the Eulerian step section. Chapter III describes how the three contact types are enforced in the mean strain rate, pressure equilibration, stress equilibration, and contact mixture theories. The details on the development of the new contact algorithm for Eulerian formulations are developed in chapter IV. The concept of independent fields is introduced first, then followed by the analysis of independent deformations. The last section of the chapter, dependent deformations, describes the algorithm used to couple nodal accelerations and velocities as a functions of the three contact types. Chapter V presents the numerical results for example problems including bouncing cylinder, sliding block, Taylor anvil test, projectile penetration, and high velocity shock compression of a steel powder. The final chapter is dedicated to conclusions and future work.

## Chapter II

# Eulerian Formulation

This chapter covers the basic concepts of the Eulerian formulation used in this research. In the first section operator splitting is used to separate the Eulerian conservation equations into a Lagrangian and an Eulerian step. Unsplit methods are also available and can achieve higher accuracy than operator splitting, however, their implementation is more complicated and expensive. Operator splitting is often preferred because of its simplicity, robustness, and efficiency. The second section reviews the Lagrangian step, including the time integration, some common constitutive equations, and the contact enforcement. The third section explains the material transport and interface tracking used in the Eulerian step.

### II.A Operator Splitting

Operator splitting separates the Eulerian conservation equations into source and convective equations. The source equations correspond to the Lagrangian conservation equations, therefore, they are referred to as the Lagrangian step. The convective

equations correspond to the transport through space and are referred to as the Eulerian step. The two steps are solved independently and sequentially.

The Eulerian conservation equations have the general form

$$\frac{\partial \phi}{\partial t} + \nabla \cdot \Phi = S \quad (\text{II.1})$$

where  $\phi$  is a solution variable,  $\Phi$  is a flux function, and  $S$  is the source term. Operator splitting [13] divides equation (II.1) in two separate equations.

$$\frac{\partial \phi}{\partial t} = \frac{\partial \phi^L}{\partial t} + \frac{\partial \phi^E}{\partial t} \quad (\text{II.2})$$

$$\frac{\partial \phi^L}{\partial t} = S \quad (\text{II.3})$$

$$\frac{\partial \phi^E}{\partial t} + \nabla \cdot \Phi = 0 \quad (\text{II.4})$$

Equation (II.3) corresponds to the Lagrangian step and equation (II.4) corresponds to the Eulerian step. Figure II.1 presents a physical interpretation of the two steps.

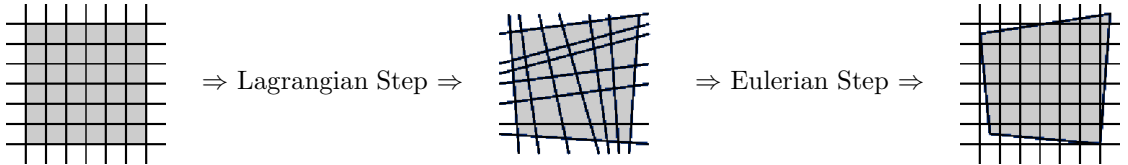


Figure II.1: Lagrangian and Eulerian Steps

The Eulerian equations for the conservation of mass, momentum, and energy are:

$$\frac{\partial \rho}{\partial t} + \nabla \cdot (\rho \mathbf{v}) = 0 \quad (\text{II.5})$$

$$\frac{\partial(\rho \mathbf{v})}{\partial t} + \nabla \cdot (\rho \mathbf{v} \otimes \mathbf{v}) = \nabla \cdot \boldsymbol{\sigma} + \rho \mathbf{b} \quad (\text{II.6})$$

$$\frac{\partial(\rho e)}{\partial t} + \nabla \cdot (\rho e \mathbf{v}) = \boldsymbol{\sigma} : \dot{\boldsymbol{\epsilon}} \quad (\text{II.7})$$

where  $\rho$  is the density,  $\mathbf{v}$  is the velocity,  $\boldsymbol{\sigma}$  is the Cauchy stress,  $\dot{\boldsymbol{\epsilon}}$  is the strain rate,  $\mathbf{b}$  is the body force,  $e$  is the internal energy, and  $t$  is the time. Equations (II.5), (II.6), and (II.7) are split into the Lagrangian step:

$$\frac{\partial \rho}{\partial t} = 0 \quad (\text{II.8})$$

$$\frac{\partial(\rho \mathbf{v})}{\partial t} = \nabla \cdot \boldsymbol{\sigma} + \rho \mathbf{b} \quad (\text{II.9})$$

$$\frac{\partial(\rho e)}{\partial t} = \boldsymbol{\sigma} : \dot{\boldsymbol{\epsilon}} \quad (\text{II.10})$$

and into the Eulerian step:

$$\frac{\partial \rho}{\partial t} + \nabla \cdot (\rho \mathbf{v}) = 0 \quad (\text{II.11})$$

$$\frac{\partial(\rho \mathbf{v})}{\partial t} + \nabla \cdot (\rho \mathbf{v} \otimes \mathbf{v}) = 0 \quad (\text{II.12})$$

$$\frac{\partial(\rho e)}{\partial t} + \nabla \cdot (\rho e \mathbf{v}) = 0 \quad (\text{II.13})$$

## II.B Lagrangian Step

The time integration, the constitutive equations, and contact enforcement take place during the Lagrangian step. The contact enforcement depends on whether a mixture theory or the extended finite element method is implemented. Since these approaches are different and require an in depth consideration, they are treated separately in chapters three and four.

### II.B.1 Time integration

The central difference method is a simple and efficient way to update the time dependent variables. This time integration scheme is implemented in Raven and pre-



sented here.

$$\mathbf{a}^n = [\mathbf{M}^n]^{-1} \{ \mathbf{F}_{ext.}^n - \mathbf{F}_{int.}^n \} \quad \text{where} \quad \mathbf{F}_{int.}^n = \int \mathbf{B}^T \boldsymbol{\sigma}^n dV \quad (\text{II.14})$$

$$\mathbf{v}^{n+\frac{1}{2}} = \mathbf{v}^{n-\frac{1}{2}} + \Delta t \mathbf{a}^n \quad (\text{II.15})$$

$$\mathbf{x}^{n+1} = \mathbf{x}^n + \Delta t \mathbf{v}^{n+\frac{1}{2}} \quad (\text{II.16})$$

$$\dot{\boldsymbol{\epsilon}}^{n+\frac{1}{2}} = \mathbf{B} \mathbf{v}^{n+\frac{1}{2}} \quad (\text{II.17})$$

$$\boldsymbol{\sigma}^{n+1} = \text{Constit.Eq.}(\boldsymbol{\sigma}^n, \dot{\boldsymbol{\epsilon}}^{n+\frac{1}{2}}, \Delta t, \text{etc.}) \quad (\text{II.18})$$

where  $\mathbf{a}$  is the acceleration,  $\mathbf{M}$  is the mass,  $\mathbf{F}_{ext.}$  is the external force,  $\mathbf{B}$  is the matrix containing the shape functions derivatives,  $\int \cdot dV$  is the integration over the volume,  $\mathbf{x}$  is the material coordinate,  $n$  is the current time step number, and  $\Delta t$  is the time step.

## II.B.2 Constitutive equations

Various constitutive equations are available in Raven. However, this section presents only the equations used in this research, namely: linear elasticity,  $J_2$  plasticity with linear hardening (for low strain rate problems), and the Steinberg-Guinan constitutive model (for high strain rate problems). The materials analyzed in this research are assumed to be isotropic.

The stress tensor is separated into two terms:

$$\boldsymbol{\sigma} = \boldsymbol{\sigma}' - \mathbf{I}P \quad (\text{II.19})$$

where  $\boldsymbol{\sigma}'$  is the deviatoric part of the Cauchy stress tensor,  $\mathbf{I}$  is the identity matrix, and  $P$  is the hydrostatic pressure. Equation (II.19) is updated as follows:

$$\boldsymbol{\sigma}^{n+1} = \boldsymbol{\sigma}^n + (\dot{\boldsymbol{\sigma}}' - \mathbf{I}\dot{P}) \Delta t \quad (\text{II.20})$$

where  $\dot{\boldsymbol{\sigma}}'$  is the deviatoric stress rate, and  $\dot{P}$  is the pressure rate, give by

$$\dot{P} = -K \operatorname{tr}(\dot{\boldsymbol{\epsilon}}) \quad (\text{II.21})$$

where  $K$  is the bulk modulus,  $\operatorname{tr}(\cdot)$  is the trace, and  $\dot{\boldsymbol{\epsilon}}$  is the strain rate.

The material constitutive relations use the objective Jaumann stress rate for the deviatoric stress,

$$\boldsymbol{\sigma}^{\nabla J} = \dot{\boldsymbol{\sigma}}' - \mathbf{W} \cdot \boldsymbol{\sigma}' - \boldsymbol{\sigma}' \cdot \mathbf{W}^T \quad (\text{II.22})$$

where  $\boldsymbol{\sigma}^{\nabla J}$  is the objective Jaumann stress rate, and  $\mathbf{W}$  is the spin tensor.

### Linear elasticity

The deviatoric stress rate for the linear elasticity model corresponds to

$$\boldsymbol{\sigma}^{\nabla J} = 2G\dot{\boldsymbol{\epsilon}}' \quad (\text{II.23})$$

where  $G$  is the shear modulus, and  $\dot{\boldsymbol{\epsilon}}'$  is the deviatoric strain rate.

### Plasticity

The strain hardening for the plasticity models is linear and follows the isotropic  $J_2$  flow theory:

$$\boldsymbol{\sigma}^{\nabla J} = 2G(\dot{\boldsymbol{\epsilon}}' - \dot{\boldsymbol{\epsilon}}^p) \quad (\text{II.24})$$

$$\dot{\boldsymbol{\epsilon}}^p = \frac{3\boldsymbol{\sigma}'}{2\bar{\sigma}} \dot{\bar{\epsilon}}^p \quad (\text{II.25})$$

$$\bar{\sigma} = \sqrt{\frac{3}{2}\boldsymbol{\sigma}' : \boldsymbol{\sigma}'} \quad (\text{II.26})$$

$$\dot{\bar{\epsilon}}^p = \frac{3\boldsymbol{\sigma}' : \mathbf{C}_{el} : \dot{\boldsymbol{\epsilon}}}{2\bar{\sigma}(H(\bar{\epsilon}^p) + 3\mu)} \quad (\text{II.27})$$

$$H(\bar{\epsilon}^p) = \frac{\partial \sigma_y(\bar{\epsilon}^p)}{\partial \bar{\epsilon}^p} \quad (\text{II.28})$$

$$\bar{\sigma} - \sigma_y(\bar{\epsilon}^p) = 0 \quad (\text{II.29})$$

$$\bar{\epsilon}^p = \int \dot{\bar{\epsilon}}^p dt \quad (\text{II.30})$$

where  $\dot{\bar{\epsilon}}^p$  is the plastic strain rate,  $\bar{\sigma}$  is the Von Mises effective stress,  $\dot{\bar{\epsilon}}^p$  is the effective plastic strain rate,  $C_{el}$  is the fourth order elastic moduli,  $\mu$  is a Lamé constant,  $\sigma_y$  is the yield stress, and equation (II.29) is the yield condition. The radial return method is used for the numerical integration [9]. The reader is encouraged to review Belytchko et al. [29] for more details on the  $J_2$  theory and implementation.

For low strain rates, linear hardening is used,

$$\sigma_y(\bar{\epsilon}^p) = \sigma_{y_o} + H_1 \bar{\epsilon}^p \quad (\text{II.31})$$

where  $H_1$  is the strain hardening parameter, and  $\sigma_{y_o}$  is the initial yield stress.

For high strain rate problems (i.e.  $\dot{\epsilon} > 10^5 \frac{1}{s}$ ) the Steinberg-Guinan model [14, 15] is used,

$$G = G_o \left[ 1 + \frac{bP}{\left(\frac{\rho}{\rho_o}\right)^{\frac{1}{3}}} + h(T - 300) \right] \exp \left[ \frac{-fe}{e_{melt} - e} \right] \quad (\text{II.32})$$

$$\sigma_y = \sigma'_{y_o} \left[ 1 + \frac{b'P}{\left(\frac{\rho}{\rho_o}\right)^{\frac{1}{3}}} + h(T - 300) \right] \exp \left[ \frac{-fe}{e_{melt} - e} \right] \quad (\text{II.33})$$

$$\sigma'_{y_o} = MIN(\sigma_{max}, \sigma_{y_o} [1 + \beta(\bar{\epsilon}_o^p + \bar{\epsilon}^p)]^\alpha) \quad (\text{II.34})$$

where the subscript  $o$  indicates the initial state of the variable,  $P$  is the pressure,  $T$  is the temperature,  $\alpha$  and  $\beta$  are strain hardening parameters,  $e$  is the internal energy,  $e_{melt}$  is the melting energy, and  $f$  is the thermo softening parameter. Constants  $b$ ,  $b'$ , and  $h$ , are found experimentally and are defined as follows:

$$b = \frac{1}{G_o} \left. \frac{\partial G}{\partial P} \right|_0 \quad (\text{II.35})$$

$$b' = \frac{1}{\sigma_{y_o}} \frac{\partial \sigma_y}{\partial P} \Big|_0 \quad (\text{II.36})$$

$$h = \frac{1}{G_o} \frac{\partial G}{\partial T} \Big|_0 \quad (\text{II.37})$$

The Steinberg-Guinan model assumes the yield stress to be rate independent because the rate effects have typically saturated out at the high strain rate where this model is used. However, at these rates the pressure and temperature dependency becomes important.

## II.C Eulerian Step

This section describes the transport and interface tracking algorithms used in this research. These methods are simple and effective when a structured mesh is employed. However, if an unstructured mesh is utilized, the formulation becomes more elaborate.

### II.C.1 Transport

The transport through space in Raven is implemented with the monotone upstream-centered schemes for conservation laws (MUSCL). The MUSCL algorithm was developed by Bram Van Leer [12], it is second order accurate in the smooth regions of the solution and it is monotonic. The change in the solution variable  $\phi$  in an element is determined from the material entering and leaving it over the time step:

$$\phi_+^{n+1} = \frac{1}{V_+^{n+1}} \left[ V_-^{n+1} \phi_-^{n+1} + \sum_{i=1}^N \Delta V_i \phi_i^{n+1} \right] \quad (\text{II.38})$$

where the + and - subscripts indicate the state of the variable before and after the transport respectively,  $n + 1$  indicates that the time dependent variables have been updated,  $V$  is the element's volume,  $\Delta V_i$  is the volume swept in or out by the nodes

defining the  $i$ -th face of the element during the deformation, and  $\phi_i^{n+1}$  is the mean value of  $\phi^{n+1}$  in  $\Delta V_i$ . The value of  $\Delta V_i$  is positive when it is swept inside the element and negative when it is swept out. For multi-material elements, an interface reconstruction or interface tracking method [16, 18, 23, 25, 30, 34, 35] provides the location of the material's interfaces, and partition  $\Delta V_i$  among the different materials. The transport is illustrated in the one-dimensional example of figure II.2.

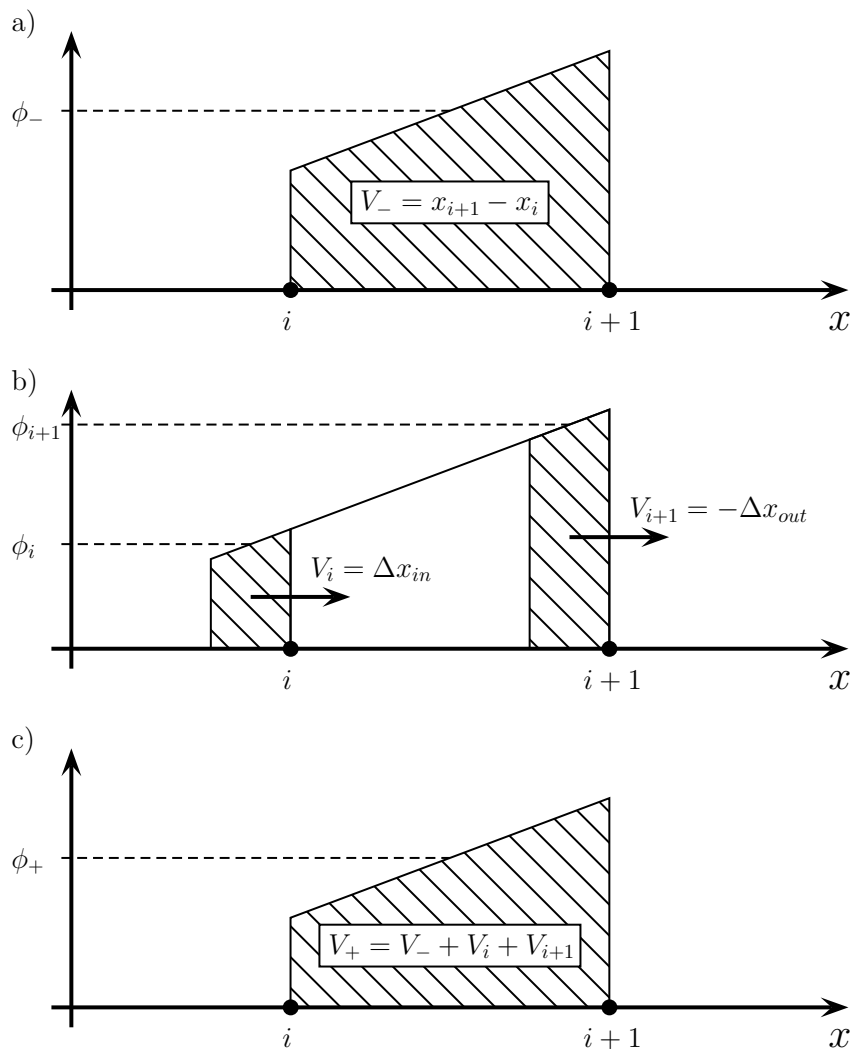


Figure II.2: Transport concept: one-dimensional example

Figure II.2 a) displays an element before the transport occurs. The element is defined by nodes  $i$  and  $i + 1$ . For one-dimensional problems, the volume can be considered as the distance between the two nodes. The value of  $\phi$  inside the element is interpreted as the average value within the element (the volume-weighted variable is represented by the shaded area). Figure II.2 b) shows the element during the transport. The volume entering the element (i.e. swept in) through the face  $i$  is  $\Delta x_{in}$  while  $-\Delta x_{out}$  corresponds to the volume exiting the element (i.e. swept out) through the face  $i + 1$ . Note that also in this case the shaded areas represent the volume-weighted variable being swept. Figure II.2 c) shows the element after the transport. The new volume is calculated and the transported value is obtained according to equation (II.38).

$$\phi_+^{n+1} = \frac{1}{V_+^{n+1}} (V_-^{n+1} \phi_-^{n+1} + \Delta V_i \phi_i^{n+1} + \Delta V_{i+1} \phi_{i+1}^{n+1}) \quad (\text{II.39})$$

MUSCL generates a linear distribution of  $\phi$  within the element to replace the finite element piecewise constant value of  $\phi$  per element, which is evaluated in the middle of the element. Consider element  $E$  in figure II.3,

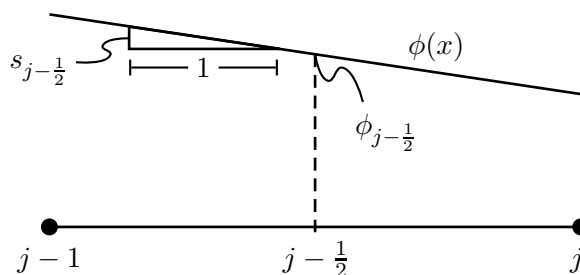


Figure II.3: Linear distribution of  $\phi$  in element  $E$

where  $j - 1$  and  $j$  are the nodes defining the element,  $\phi_{j-\frac{1}{2}}$  is the value evaluated by the algorithm and being transported, and  $s_{j-\frac{1}{2}}$  is the slope of the linear distribution to be

defined. The distribution of  $\phi$  for the element in the figure is

$$\phi(x) = s_{j-\frac{1}{2}}(x - x_{j-\frac{1}{2}}) + \phi_{j-\frac{1}{2}} \quad (\text{II.40})$$

The slope is obtained from the values of  $\phi$  in the surrounding elements. Figure II.4 displays the three slopes (gray lines) considered for  $s_{j-\frac{1}{2}}$ , where the full circles represent the position of the nodes a time  $n$ , the empty circles represent the position of the nodes at time  $n + 1$ , and the horizontal lines represent the constant value of  $\phi$  calculated by the algorithm for each element. The second order accuracy in the smooth regions of the solution is obtained by creating second order accurate slopes. Figure II.4 a) is the center slope and it is given by:

$$s_{j-\frac{1}{2}}^c = \frac{\phi_{j+\frac{1}{2}} - \phi_{j-\frac{3}{2}}}{x_{j+\frac{1}{2}} - x_{j-\frac{3}{2}}} \quad (\text{II.41})$$

The left slope, which is represented in figure II.4 b), follows:

$$s_{j-\frac{1}{2}}^l = \frac{\phi_{j-\frac{1}{2}} - \phi_{j-\frac{3}{2}}}{x_{j-\frac{1}{2}} - \tilde{x}_{j-1}} \quad (\text{II.42})$$

where  $\tilde{x} = x + \frac{1}{2}v \Delta t$ . Similarly, for the right slope in figure II.4 c),

$$s_{j-\frac{1}{2}}^r = \frac{\phi_{j+\frac{1}{2}} - \phi_{j-\frac{1}{2}}}{\tilde{x}_j - x_{j-\frac{1}{2}}} \quad (\text{II.43})$$

The monotonicity of MUSCL is achieved by preventing the slope from creating values at the faces of the element (i.e.  $j - 1$  and  $j$  for the middle element) that are outside the range of the value in the adjacent elements (i.e.  $\phi_{j-\frac{3}{2}} - \phi_{j+\frac{1}{2}}$  for the middle element), therefore, the smallest of the three slopes is selected.

$$s_{j-\frac{1}{2}} = \frac{1}{2} [SIGN(s_{j-\frac{1}{2}}^l) + SIGN(s_{j-\frac{1}{2}}^r)] \quad (\text{II.44})$$

$$MIN(|SIGN(s_{j-\frac{1}{2}}^l)|, |SIGN(s_{j-\frac{1}{2}}^c)|, |SIGN(s_{j-\frac{1}{2}}^r)|)$$

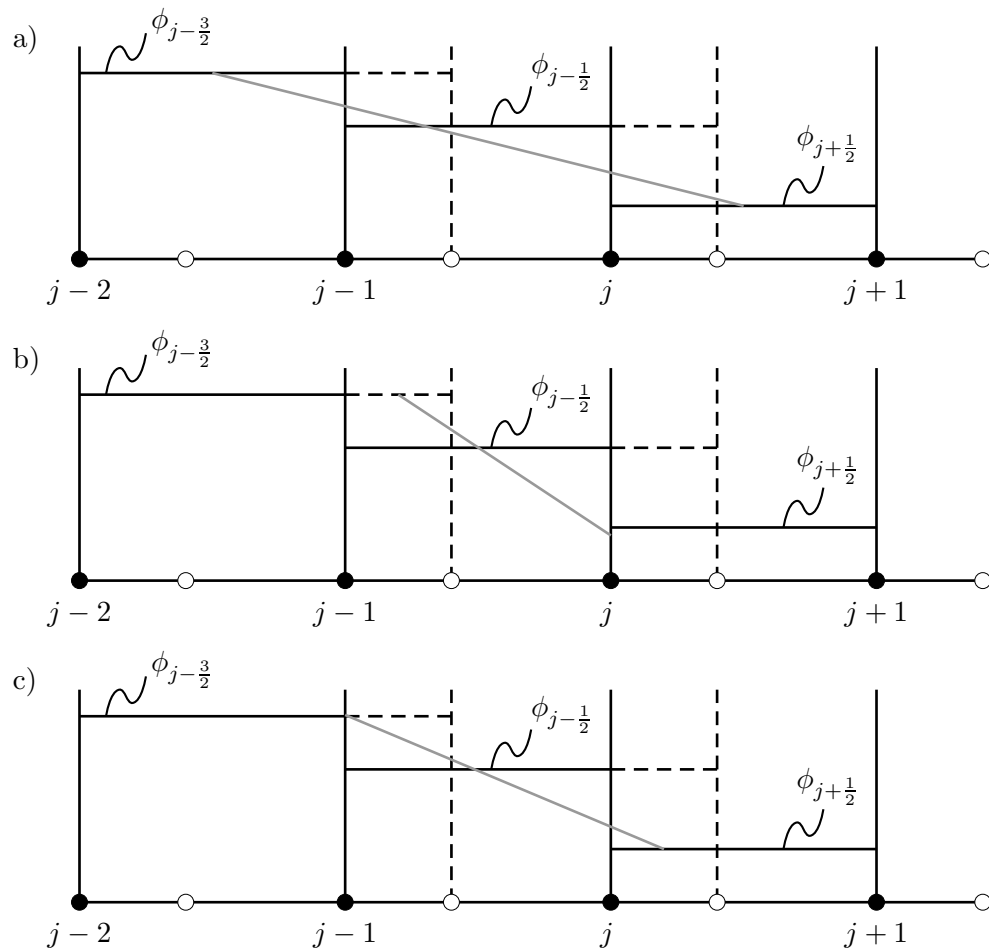


Figure II.4: Slopes considered for the linear distribution

In two-dimensional problems the transport is performed by operator splitting, first performing the one-dimensional transport in the x-direction and then in the y-direction. The order is alternated every time step in order to minimize errors due to aliasing. In figure II.5, a variable is swept outside the shaded element. In this case, the volume weighted variable is first swept out in the x-direction and then swept out in the y-direction. This method is easily implemented in structured meshes, in addition, it incorporates corner coupling. Corner coupling is the flow of the variable being



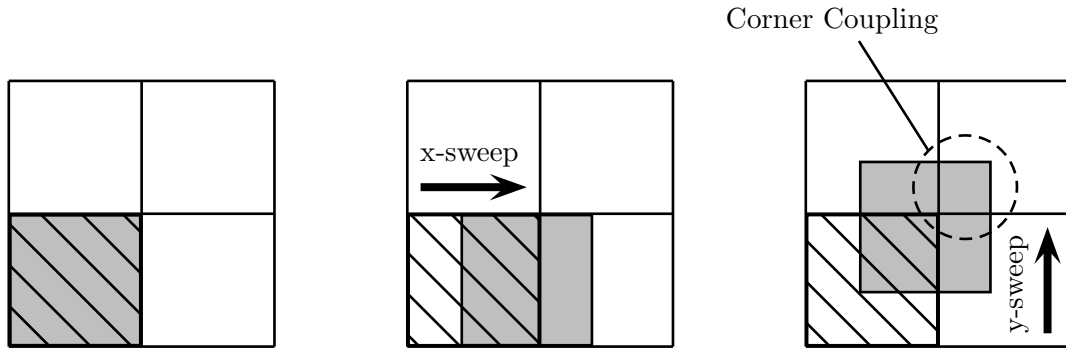


Figure II.5: Sweeping concept: two-dimensional example

transported (e.g. volume) from an element to one of its adjacent diagonal elements (see figure II.5). If the transport were carried out in one sweep, the corner coupling would not be accounted because the transport needs a face between two elements in order to transport a variable. For instance, in the example of figure II.5 the transport is diagonal. Therefore, since the face between the lower left element and the upper right element does not exist, the variable would not be transported into the upper right element.

### II.C.2 Interface reconstruction

The interface reconstruction, or tracking, is based on the work of Youngs [16]. The number of interfaces in a multi-material element corresponds to the number of materials present in the element minus one. Each interface separates the element in two regions,  $\alpha$  and  $\beta$ , and each region contains one or more materials. The slope of an interface is determined by the volume fraction of  $\alpha$  and  $\beta$  inside the element being considered and its surrounding elements. Consider element  $E$  in figure II.6 and its surrounding elements: A, B, C, D, F, G, H, and I; moreover, let the shaded region define  $\alpha$  and the blank region define  $\beta$ . In this case, the general equation to calculate the slope

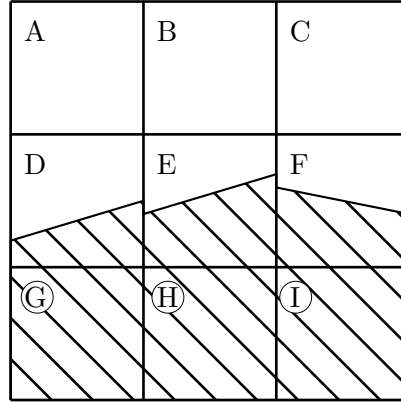


Figure II.6: Two dimensional interface tracking scheme

between  $\alpha$  and  $\beta$  is:

$$\text{slope}_E^{(\alpha,\beta)} = \frac{b_{(E,F)}^{(\alpha,\beta)} - b_{(D,E)}^{(\alpha,\beta)}}{b_{(E,H)}^{(\alpha,\beta)} - b_{(B,E)}^{(\alpha,\beta)}} \quad (\text{II.45})$$

where  $\text{slope}_E^{(\alpha,\beta)}$  is the slope of the interface that separates volume  $\alpha$  from volume  $\beta$  inside element E, and  $b_{(E,F)}^{(\alpha,\beta)}$  indicates the volume fraction for the interface  $(\alpha, \beta)$  at the side  $(E, F)$ , which is obtained from volumes  $\alpha$  and  $\beta$  inside elements  $E$  and  $F$ . A detailed description of the calculation of  $b$  is found in Benson [18, 34]. Once the slope is determined, the interface is moved parallel to itself until the correct volumes of  $\alpha$  and  $\beta$  are obtained. Note that when more than two materials are present, it is necessary to specify a layering order for the materials.

## Chapter III

# Mixture Theories

Mixture theories redistribute the strain rate of each mixed element among the materials inside the element. The nomenclature “mixed” and “multi-material” will be used interchangeably throughout this work. Among the mixture theories available are the mean strain rate, the pressure equilibration, the stress equilibration, and the contact mixture theories. The most appropriate theory is selected according to the problem and the prescribed contact type. After the strain rates are redistributed, the stress of each material inside the element is calculated using the material’s constitutive equation. Finally, the stress of the element, which is needed for the time integration, is obtained from the stress of its materials.

The first section of this chapter presents the equations common to all mixture theories, namely the constraint on the strain rates, and the calculation of the element’s stress from those in its materials. The next three sections describe the theories used to partition the strain rate of the mixed element among its materials, and the last section reviews the separation condition.

### III.A Requirements

All mixture theories constrain the volume weighted average strain rate of the materials inside the mixed element to equal the strain rate of the element,

$$\dot{\epsilon}_E = \mathbf{B}_E \{v_1 \dots v_i \dots v_N\}^T \quad (\text{III.1})$$

$$\sum_{m=1}^{nmat} \dot{\epsilon}_E^m \frac{V_E^m}{V_E} = \dot{\epsilon}_E \quad (\text{III.2})$$

where  $\dot{\epsilon}_E$  is the strain rate for element  $E$ ,  $\mathbf{B}_E$  is the matrix containing the shape function derivatives for element  $E$ ,  $v_i$  is the velocity of node  $i$ ,  $N$  is the number of the nodes per element,  $nmat$  is the number of materials inside the element,  $\dot{\epsilon}_E^m$  is the strain rate of material  $m$  in element  $E$ ,  $V_E^m$  is the volume of material  $m$  in element  $E$ , and  $V_E$  is the volume of element  $E$ .

The stress of mixed elements is the volume weighted average of the stress in its materials,

$$\sigma_E = \sum_{m=1}^{nmat} \sigma_E^m \frac{V_E^m}{V_E} \quad (\text{III.3})$$

where  $\sigma_E$  is the stress tensor of mixed element  $E$ , and  $\sigma_E^m$  is the Cauchy stress tensor for material  $m$  in element  $E$ .

### III.B Mean Strain Rate

The mean strain rate is the simplest mixture theory. This theory assigns the mean strain rate of the mixed element to all of its materials,

$$\dot{\epsilon}_E^{m_1} = \dot{\epsilon}_E \quad \forall m_1 \in Mat_E \quad (\text{III.4})$$

where  $Mat_E$  is the set of all the materials inside element  $E$ .

Equation (III.4) assigns the same strain rate to all the materials inside the element, therefore, all materials are compressed identically and preserve their volume ratio. As a consequence, stress is generated when two solid materials separated by a void material move perpendicular with respect to each other. Moreover, the two solid materials will never share the same interface because the void material is never compressed out of the element. In order to eliminate the stress issue when the two solid materials move apart from each other, the volume of the two solid materials is relaxed until the stress in the direction normal to the respective interface with the void material becomes zero, in the meantime, the volume of the void material is modified to accommodate the volume change. On the other hand, when the two materials move towards each other, the following equations address the problem:

$$R = MAX \left\{ \frac{V^+}{V^-}, \frac{MIN \left( V^+, \sum_m^{nsolid} V_m^- \right)}{\sum_m^{nsolid} V_m^-} \right\} \quad (III.5)$$

$$V_m^+ = V^+ - R \sum_i^{nsolid} V_i^- - \sum_{\substack{i \\ i \neq m}}^{nvoid} V_i^+ \quad \forall m \in nvoid \quad (III.6)$$

$$V_m^+ = R V_m^- \quad \forall m \in nsolid \quad (III.7)$$

where  $nsolid$  is the number of solid materials inside the element,  $nvoid$  is the number of void materials inside the element,  $R$  is the compression ratio,  $V^-$  is the element volume before the time integration, and  $V^+$  is the volume of the element after the time integration. When the element begins to undergo compression (i.e.  $V^- > V^+ > \sum_m^{nsolid} V_m^-$ ), equation (III.6) starts to compress out the void materials one by one, until they are all evacuated from the element. During this process, the volume, along with the hydrostatic pressure of the solid materials, remains unchanged. When all the void

materials are compressed out (i.e.  $V^- > \sum_m^{n_{solid}} V_m^- > V^+$ ), equation (III.7) begins to compress all the solid materials by the same ratio. Note that equation (III.6) must be constrained so that the void materials do not become negative.

This modification results in an inequality between the work done by the element and the work done by the material inside the element.

$$\mathbf{v} \cdot \int \mathbf{B}^T \boldsymbol{\sigma}_E dV \neq \sum_m \boldsymbol{\sigma}_E^m : \dot{\boldsymbol{\epsilon}}_E^m \Delta V_E^m \quad (\text{III.8})$$

In other words, the work of the element compressing out void materials does not generate pressure, or work, in the materials left inside the element. This error is attributed to the hydrostatic pressure since the above equations modify only the volumetric strain.

### III.C Pressure and Stress Equilibration

The pressure and stress equilibration mixture theories are used when an element is filled primarily with void material and contains a small fragment of solid material. Because of the large volume of void material, the small fragment may experience extremely large stresses. Assume that the velocities in equation (III.1) are such that the element is compressing at a high rate. Equation (III.4) assigns the same high strain rate to the fragment and the void material. According to the respective constitutive equations, the fragment experiences high stress while the stress in the void material remains small. Because of the volume weighted averaging of equation (III.3), the stress in the element is similar to the one in the void material (i.e. small). As a consequence, the internal forces, and therefore the accelerations, of equation (II.14) are also small and have little effect on reducing the nodal velocities of equation (III.1). As a result, the strain rate in the

next time step will still be high and the stress in the small fragment of solid material will have another large increment. This problem can be solved by equilibrating the pressure or the stress.

The equations for pressure equilibration are:

$$P_E^{m_1} = P_E^{m_2} \quad \forall \{m_1, m_2\} \in Mat_E \quad (\text{III.9})$$

$$\sum_m^{nmat} tr(\dot{\epsilon}_E^m) \frac{V_E^m}{V_E} = tr(\dot{\epsilon}_E) \quad (\text{III.10})$$

where the superscripts indicate the material, and  $tr(\dot{\epsilon}_E)$  corresponds to the volumetric strain rate of element  $E$ . Since the pressures in equation (III.9) are a function of their respective volumetric strain rate, the two equations above provide  $nmat$  equations for  $nmat$  unknown volumetric strain rates. When equation (III.10) is subtracted from equation (III.2) the following is obtained.

$$\sum_{m=1}^{nmat} \dot{\epsilon}'_E{}^m \frac{V_E^m}{V_E} = \dot{\epsilon}_E - \frac{1}{3} tr(\dot{\epsilon}_E) \mathbf{I} = \dot{\epsilon}'_E \quad (\text{III.11})$$

where  $\dot{\epsilon}'$  indicates the deviatoric strain rate. This provides one equation for  $nmat$  unknown deviatoric strain rates. The missing  $nmat - 1$  equations are obtained similarly to equation (III.4),

$$\dot{\epsilon}'_E{}^{m_1} = \dot{\epsilon}'_E{}^{m_2} \quad \forall \{m_1, m_2\} \in Mat_E \quad (\text{III.12})$$

The stress equilibration constraint is defined by

$$\sigma_E^{m_1} = \sigma_E^{m_2} \quad \forall \{m_1, m_2\} \in Mat_E \quad (\text{III.13})$$

In this case, equation (III.13) combined with equation (III.2) replaces equations (III.9) through (III.12) to produce the required number of equations to solve for the  $nmat$  strain rates.

These solutions impose the same stress, or pressure, on all materials inside the element by adjusting their strain rates. As a consequence, the strain rate of the fragment is considerably reduced, lessening the stress and solving the issue. The pressure equilibration and stress equilibration theories may encounter energy conservation problems. The reader is encouraged to review Benson [21] for more details on the energy properties of these theories.

Note that the above methods do not require a void collapse algorithm. In the mean strain rate mixture theory all the materials inside an element compress identically, and therefore void materials are never compressed out of the element. However, the pressure, or stress, equilibration mixture theories increase the otherwise small stress of the void material when the element is compressed. As a result, the strain rate of the void material increases, inducing its volume to shrink at a rate higher than the one of solid materials. When a certain minimum volume value is met, the void material is eliminated from the element.

### **III.D Contact**

The purpose of the contact mixture theory is to obtain strain rate of the materials by imposing interface jump conditions, which are selected as a function of the appropriate contact type. Fully bonded, frictionless slip, and slip with friction contact types are analyzed in this section.



### III.D.1 Fully bonded

For the fully bonded case, the equations are:

$$[\boldsymbol{\sigma}_E^{m_1} - \boldsymbol{\sigma}_E^{m_2}] \mathbf{n}_i = 0 \quad (\text{III.14})$$

$$[\boldsymbol{\sigma}_E^{m_1} - \boldsymbol{\sigma}_E^{m_2}] \mathbf{t}_i = 0 \quad (\text{III.15})$$

where  $m_1$  and  $m_2$  are the materials separated by interface  $i$ ,  $\mathbf{n}$  is the normal to the interface, and  $\mathbf{t}$  is the interface's tangent. Equation (III.14) and equation (III.15) enforce equilibrium at the interface, moreover, they generate  $nmat - 1$  number of equations to solve for the strain rate of the materials; the missing equation is provided by (III.2).

### III.D.2 Frictionless slip

For the frictionless contact type, two constraints are added to the above equations.

$$\mathbf{t}_i \cdot \boldsymbol{\sigma}_E^m \mathbf{n}_i = 0 \quad (\text{III.16})$$

$$\sum_m \dot{\boldsymbol{\epsilon}}_E^m \frac{V_E^m}{V_E} + \sum_i^{nmat-1} \{\mathbf{t}_i \otimes \mathbf{n}_i + \mathbf{n}_i \otimes \mathbf{t}_i\} s_i = \dot{\boldsymbol{\epsilon}}_E \quad (\text{III.17})$$

The frictionless contact type is enforced in equation (III.16) by setting the shear stress at the interface to zero. In order to accommodate the  $nmat - 1$  set of new constraints, an equal number of unknowns is needed. These unknowns are provided by  $s$  in equation (III.17), where  $s_i$  can be considered as the relative slip for interface  $i$ . Note that equation (III.2) is already incorporated in equation (III.17).

### III.D.3 Slip with friction

For the slip with friction, equation (III.16) is replaced by

$$|\mathbf{t}_i \cdot \boldsymbol{\sigma}_E^m \mathbf{n}_i| = \mu |\mathbf{n}_i \cdot \boldsymbol{\sigma}_E^m \mathbf{n}_i| \quad (\text{III.18})$$

where  $\mu$  is the coefficient of friction.

### III.E Separation

Separation occurs when two solid materials sharing the same interface pull apart from each other. During this process, if separation is allowed, a void material is introduced between the two solid materials. As a consequence, the existing interface is reassigned to be shared by the void material and one solid material. Also, a new interface, parallel to the existing, one is generated and shared by the void material and the second solid material. To establish whether the two materials are pulling apart from each other, a volume weighted average of the two materials' stress is used,

$$\mathbf{n}_i \cdot \frac{(\boldsymbol{\sigma}_E^{m_1} V_E^{m_1} + \boldsymbol{\sigma}_E^{m_2} V_E^{m_2})}{V_E^{m_1} + V_E^{m_2}} \mathbf{n}_i > 0 \quad (\text{III.19})$$

where  $m_1$  and  $m_2$  are the two solid materials sharing interface  $i$ . The two materials separate when equation (III.19) is greater than zero. At this point the volume, and therefore the volumetric strain, of the two solid materials is recalculated to allow the traction at the interface to be zero. As a result, the volume of the solid materials is reduced and the void material fills the missing volume in the element.

## Chapter IV

# eXtended Finite Element

# Formulation for MMALE

# Calculations

The multi-material arbitrary Lagrangian Eulerian (MMALE) formulation presented in this section assigns each node independent displacement, velocity, and acceleration fields for each material surrounding it. The idea of locally introducing extra degrees of freedom emerged from the extended finite element method by Belytschko et al. [22, 24, 26, 31, 33, 37]. For this reason the formulation developed in this chapter adopts the “extended finite element” nomenclature.

The first section of this chapter describes the independent fields used in the finite element formulation. The section following it shows how the transport algorithm in Raven handles independent deformations (or deformations without contact). Section three describes the interactions between the independent deformations, which take place

when materials interact and the deformation of one material affects other materials. This section is the core of the research and it covers velocity and acceleration coupling, nodal interfaces, and contact constraint enforcement. The contact enforcement subsection treats fully bonded, frictionless slip, and slip with friction contacts.

## IV.A Independent Fields

The original idea of the extended finite element method is to add additional degrees of freedom to locally enrich the solution to accurately capture the stress singularity around the tip of the crack [22, 26, 28, 31]. The current application enriches the velocity field to allow independent velocities for each material, allowing the jump discontinuities in the velocities across the interfaces to be accurately modeled. This could be thought as having one independent mesh per material where elements containing the same interface match (or overlap). As a consequence, the number of degrees of freedom associated with a specific node depends on the number of materials present in its nodal support. Figure IV.1 shows this concept.

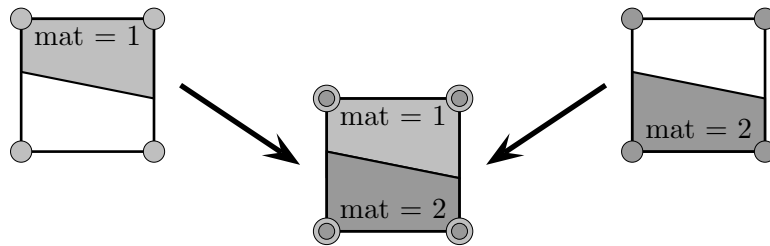


Figure IV.1: Overlapping of two materials with independent mesh

The element on the left is partially filled with material 1, which is represented by the

light gray color. The circles on the corner of the element describe the nodes, and the color of the circles relates the nodes to the material with the same color (in this case material 1). The same description applies to the element on the right of the figure. This element contains material 2, which is represented by the darker gray color, instead of material 1. The two elements are independent from each other, however, they share the same spatial coordinates at the start of the Lagrangian time step. The two elements overlap creating the mixed element in the middle of figure IV.1. As a result, the mixed element has a set of nodes per material, or each node has a set of independent fields per material.

The equations defining the main variables used for the calculations in this chapter are

$$\mathbf{v}_E^m(\mathbf{x}) = \sum_i^N \psi_{E_i}(\mathbf{x}) \mathbf{v}_{E_i}^m \quad (\text{IV.1})$$

$$\dot{\boldsymbol{\epsilon}}_E^m = \mathbf{B}_E \{ \mathbf{v}_{E_1}^m \dots \mathbf{v}_{E_i}^m \dots \mathbf{v}_{E_N}^m \}^T \quad (\text{IV.2})$$

$$\boldsymbol{\sigma}_E^m = \text{Constit.Eq.}(\boldsymbol{\sigma}_E^{old}, \dot{\boldsymbol{\epsilon}}_E^m, \Delta t, \text{etc.}) \quad (\text{IV.3})$$

$$\mathbf{F}_{E_A}^m = -\mathbf{B}_{E_A}^T \boldsymbol{\sigma}_E^m V_E^m \quad (\text{IV.4})$$

$$\mathbf{M}_{E_A}^m = \mathbf{I} \frac{1}{N} \rho_E^m V_E^m \quad (\text{IV.5})$$

where  $m$  is the material number,  $E_A$  indicates node  $A$  in element  $E$ ,  $N$  is the number of nodes per element,  $\psi$  is the shape function,  $\mathbf{I}$  is the identity matrix, and  $V$  is the volume. Equation (IV.1) defines the velocity field for element  $E$  per material, equation (IV.2) is the strain rate of element  $E$  per material, equation (IV.3) is the Cauchy stress of element  $E$  per material, equation (IV.4) is the force vector at node  $A$  generated from

element  $E$  per material, and equation (IV.5) is the mass matrix at node  $A$  generated from element  $E$  per material.

Note that the velocities are evaluated at the nodes, and each node is shared by the elements in its support. Therefore,  $\mathbf{v}_{E_i}^m$  in equation (IV.1) corresponds to  $\mathbf{v}_A^m$ , where  $A$  is the node shared by all the elements in its support including  $E$ .

## IV.B Independent Deformations

The transport algorithm in Raven ensures an accurate simulation when two materials move, or deform, without interfering with each other. For instance, let the elements at the top of figure IV.2 represent the two elements containing material 1 and 2 in figure IV.1. The elements have undergone independent deformations, and the dashed squares represent the undeformed state of the elements.

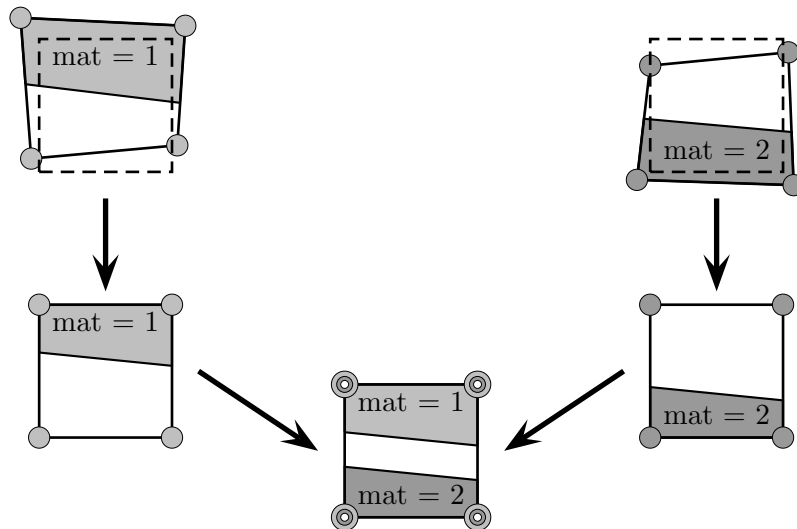


Figure IV.2: Independent deformation of two materials

The second step in the figure displays the two elements after the transport algorithm has reinstated them to their original position. Next, the two elements overlap and create the mixed element at the bottom of the figure. Finally, the total volume of the mixed element is calculated and a void material is added to fill the missing volume. Note that the introduction of a void material implies the generation of an additional material in the element.

The role of the void material is to preserve the element total volume without introducing stresses. Therefore, if a void material already exists in the mixed element and the two solid materials move apart from each other, more void material is added to the element. Similarly, some void material is removed from the element if the two solid materials move towards each other.

## IV.C Dependent Deformations

Dependent deformations occur when materials interact with each other; in other words, when the movement or deformation of one material affects the behavior of another material. The transport algorithm on its own does not handle this deformation correctly because of the independent fields that describe the behavior of each material. For instance, assume that the two elements containing material 1 and material 2 in figure IV.1 deform into the shape of the two element at the top of figure IV.3. The second step in figure IV.3 represents the independent states of the elements after the transport when the two elements are superposed to create the mixed element at the center of the figure, the two materials interfere with each other because the variables that describe the movement of the two materials do not interact during the transport (the shaded region

in the picture represents the interference). To conserve volume, the transport compresses the two materials equally until the total volume of the mixed element is achieved and the mixed element at the bottom of the figure is obtained.

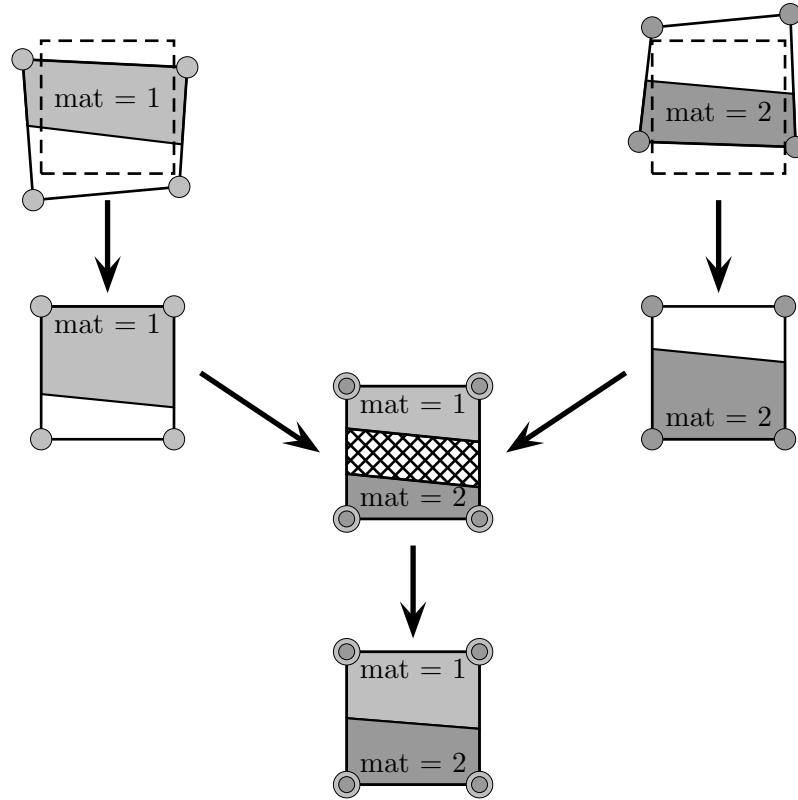


Figure IV.3: Materials interference

The finite element formulation cannot rely on the transport algorithm to avoid interference between the materials because the pressure calculated by the transport is a source of error. In fact, a large interference will generate high pressures, which will lead to large nodal forces and therefore large nodal accelerations. Large accelerations create large velocity changes (i.e.  $\Delta v$ ) during the time step update, and, as a result, the velocity changes can be larger than the initial velocity introducing errors in the



formulation, causing instabilities.

The problem is addressed by constraining, or coupling, the velocities and accelerations of the two materials before the interference occurs. The coupling procedure assigns the same value of acceleration and velocity to both materials in the direction normal to the interface, in the fully bonded case the same value of acceleration and velocity is also assigned to both material in the tangential direction, and when slip with friction is present the two materials partially influence each other tangential accelerations according to the selected friction law. As a consequence, the interference described in the example does not occur if the velocities of the two materials are coupled in the direction normal to their interface. In addition, coupling the accelerations in the same direction ensures that the coupled velocities remain the same through the time step.

#### IV.C.1 Velocity and Acceleration Coupling

The finite element formulation provides the values for the velocities at each node, therefore, the velocity coupling is implemented at the nodal level. Since the purpose of the nodal accelerations is to update the velocities during the time integration, the acceleration coupling is also implemented at the nodal level. In order to couple accelerations and velocities, the normal to the interface between each pair of materials is needed at the nodal level. Therefore, since the interface normals are described at the element level, nodal normals are obtained from the elements present in its support. For instance, figure IV.4 displays the nodal support  $A$  in a two dimensional example where two materials sharing the same interface are present.

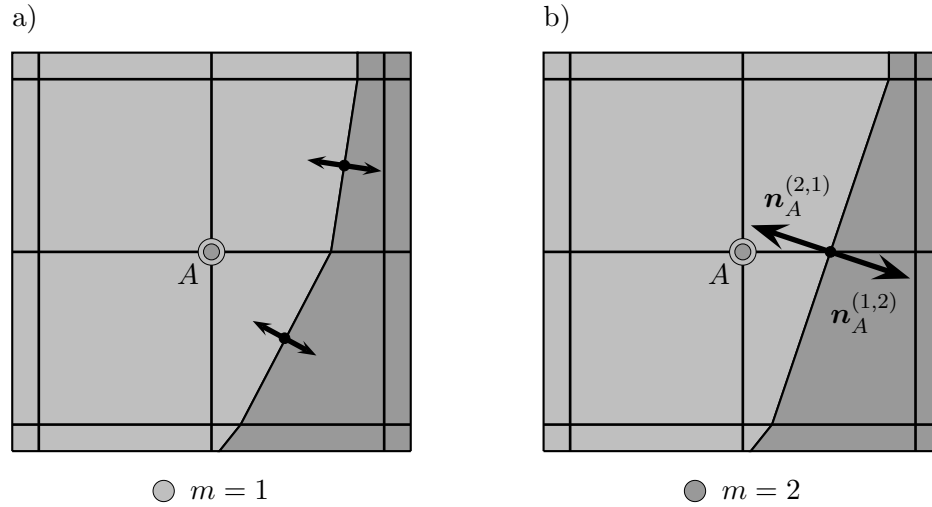


Figure IV.4: Nodal support with two materials

Figure IV.4 a) shows the normals to the interface at the element level, and figure IV.4 b) displays the interface normal at the nodal level. The light gray area corresponds to material 1, the darker gray area corresponds to material 2,  $\mathbf{n}_A^{(1,2)}$  is the nodal normal to the interface between material 1 and material 2 for node  $A$ , and  $\mathbf{n}_A^{(2,1)}$  defines the nodal normal between material 2 and material 1 for node  $A$ . The procedure used to calculate the nodal normals is described in subsection IV.C.2.

Nodal normals are used to obtain projection matrices, for the example in figure IV.4 the projection matrices are

$$\mathbf{P}_A^{(1,2)} = \mathbf{n}_A^{(1,2)} \otimes \mathbf{n}_A^{(1,2)} \quad (\text{IV.6})$$

$$\mathbf{P}_A^{(2,1)} = \mathbf{n}_A^{(2,1)} \otimes \mathbf{n}_A^{(2,1)} \quad (\text{IV.7})$$

where  $\mathbf{P}_A^{(1,2)}$  is the projection matrix between material 1 and material 2 in nodal support  $A$ , and  $\mathbf{P}_A^{(2,1)}$  corresponds to the projection matrix between material 2 and material 1 in nodal support  $A$ . In order to calculate the nodal velocities and accelerations, the masses

(IV.5) and forces (IV.4) of the elements present in the nodal support need to be gathered into nodal masses and forces. The nodal masses and forces are:

$$\mathbf{M}_A^m = \sum_E \mathbf{M}_{EA}^m \quad (\text{IV.8})$$

$$\mathbf{F}_A^m = \sum_E \mathbf{F}_{EA}^m \quad (\text{IV.9})$$

where  $\mathbf{M}_A^m$  is the mass  $\mathbf{M}$  at node  $A$  for material  $m$ ,  $\mathbf{F}$  is the nodal force, and the summation is over the elements present in the nodal support of  $A$ .

Note that the materials present in mixed elements act as springs in parallel since the materials are coupled at the same node.

### Velocity Coupling

The conservation of linear momentum law for inelastic collisions is used for the velocity coupling. In order to avoid interference between two materials, their velocities are coupled in the direction normal to their interface. The momentum is not transmitted between materials in the direction tangent to their interface, for instance, the following is true for materials 1 and 2 at node  $A$  in the example of figure IV.4:

$$\mathbf{M}_A^1(\mathbf{I} - \mathbf{P}_A^{(1,2)}) \mathbf{v}_A^{1-} = \mathbf{M}_A^1(\mathbf{I} - \mathbf{P}_A^{(1,2)}) \mathbf{v}_A^{1+} \quad (\text{IV.10})$$

$$\mathbf{M}_A^2(\mathbf{I} - \mathbf{P}_A^{(2,1)}) \mathbf{v}_A^{2-} = \mathbf{M}_A^2(\mathbf{I} - \mathbf{P}_A^{(2,1)}) \mathbf{v}_A^{2+} \quad (\text{IV.11})$$

where the superscripts  $-$  and  $+$  indicate the velocity before and after coupling, respectively. The normal velocities for the two materials are obtained from the conservation of linear momentum for perfectly plastic impacts,

$$\mathbf{M}_A^1 \mathbf{P}_A^{(1,2)} \mathbf{v}_A^{1-} + \mathbf{M}_A^2 \mathbf{P}_A^{(2,1)} \mathbf{v}_A^{2-} = (\mathbf{M}_A^1 \mathbf{P}_A^{(1,2)} + \mathbf{M}_A^2 \mathbf{P}_A^{(2,1)}) \mathbf{v}_A^{1+} \quad (\text{IV.12})$$

$$= (\mathbf{M}_A^1 \mathbf{P}_A^{(1,2)} + \mathbf{M}_A^2 \mathbf{P}_A^{(2,1)}) \mathbf{v}_A^{2+} \quad (\text{IV.13})$$

which imposes the same velocity for the two materials in the direction normal to their interface. The coupled velocity for material 1 is obtained by adding equations (IV.10), which constrains the tangential velocity, to equation (IV.12), which constrains the normal velocity.

$$\mathbf{M}_A^1 \mathbf{v}_A^{1-} + \mathbf{M}_A^2 \mathbf{P}_A^{(2,1)} \mathbf{v}_A^{2-} = (\mathbf{M}_A^1 + \mathbf{M}_A^2 \mathbf{P}_A^{(2,1)}) \mathbf{v}_A^{1+} \quad (\text{IV.14})$$

The left hand side of the equation is the linear momentum experienced by material 1, where the first term corresponds to the momentum generated by material 1 and the second term is the momentum contribution from material 2. This contribution is the mass of material 2 multiplied by its velocity, which is projected onto material 1 through the interface between the two materials. The right hand side of the equation corresponds to linear momentum after the impact, which equals the masses displaced by material 1 multiplied by its coupled velocity. For material 2, equations (IV.11) and (IV.13) are added,

$$\mathbf{M}_A^1 \mathbf{P}_A^{(1,2)} \mathbf{v}_A^{1-} + \mathbf{M}_A^2 \mathbf{v}_A^{2-} = (\mathbf{M}_A^1 \mathbf{P}_A^{(1,2)} + \mathbf{M}_A^2) \mathbf{v}_A^{2+} \quad (\text{IV.15})$$

The coupled velocities for material 1 and material 2 are obtained from equations (IV.14) and (IV.15):

$$\mathbf{v}_A^{1+} = \left[ \mathbf{M}_A^1 + \mathbf{M}_A^2 \mathbf{P}_A^{(2,1)} \right]^{-1} (\mathbf{M}_A^1 \mathbf{v}_A^{1-} + \mathbf{M}_A^2 \mathbf{P}_A^{(2,1)} \mathbf{v}_A^{2-}) \quad (\text{IV.16})$$

$$\mathbf{v}_A^{2+} = \left[ \mathbf{M}_A^1 \mathbf{P}_A^{(1,2)} + \mathbf{M}_A^2 \right]^{-1} (\mathbf{M}_A^1 \mathbf{P}_A^{(1,2)} \mathbf{v}_A^{1-} + \mathbf{M}_A^2 \mathbf{v}_A^{2-}) \quad (\text{IV.17})$$

The general expression for coupling multi-material velocities is the following:

$$\mathbf{v}_A^{i+} = \left[ \sum_j \mathbf{M}_A^j \mathbf{P}_A^{(j,i)} \right]^{-1} \left( \sum_j \mathbf{M}_A^j \mathbf{P}_A^{(j,i)} \mathbf{v}_A^{j-} \right) \quad (\text{IV.18})$$

where  $i$  and  $j$  are the materials present in the nodal support of node  $A$ , and  $\mathbf{P}^{(i,i)}$  is equal to the identity matrix. The nodal velocities are then updated with the coupled velocities:  $\mathbf{v}_A^i = \mathbf{v}_A^{i+}$ .

### Acceleration Coupling

The acceleration coupling is carried out similar to the velocity coupling; in this case, the accelerations are obtained by analyzing the forces and masses of the materials in contact, and Newton's second law of motion is used to establish the relationship between the three quantities.

Materials do not exchange forces in the tangential direction when friction is not present at the interface (the effects of friction on tangential forces are described in subsection IV.C.3), as a consequence, the accelerations remain unaffected. For instance, the tangential forces for materials 1 and 2 in the example of figure IV.4, along with the respective masses and accelerations, are

$$(\mathbf{I} - \mathbf{P}_A^{(1,2)}) \mathbf{F}_A^{1-} = (\mathbf{I} - \mathbf{P}_A^{(1,2)}) \mathbf{M}_A^1 \mathbf{a}_A^{1-} = (\mathbf{I} - \mathbf{P}_A^{(1,2)}) \mathbf{M}_A^1 \mathbf{a}_A^{1+} \quad (\text{IV.19})$$

$$(\mathbf{I} - \mathbf{P}_A^{(2,1)}) \mathbf{F}_A^{2-} = (\mathbf{I} - \mathbf{P}_A^{(2,1)}) \mathbf{M}_A^2 \mathbf{a}_A^{2-} = (\mathbf{I} - \mathbf{P}_A^{(2,1)}) \mathbf{M}_A^2 \mathbf{a}_A^{2+} \quad (\text{IV.20})$$

In the normal direction, however, the forces are coupled. Equation (IV.21) describes this force and its relation with the mass and acceleration quantities.

$$\mathbf{P}_A^{(1,2)} \mathbf{F}_A^{1-} + \mathbf{P}_A^{(2,1)} \mathbf{F}_A^{2-} = \mathbf{P}_A^{(1,2)} \mathbf{M}_A^1 \mathbf{a}_A^{1-} + \mathbf{P}_A^{(2,1)} \mathbf{M}_A^2 \mathbf{a}_A^{2-} \quad (\text{IV.21})$$

The accelerations of the two materials in the normal direction are also the same, there-

fore, the coupling of the acceleration in the normal direction is

$$\mathbf{P}_A^{(1,2)} \mathbf{F}_A^{1-} + \mathbf{P}_A^{(2,1)} \mathbf{F}_A^{2-} = (\mathbf{P}_A^{(1,2)} \mathbf{M}_A^1 + \mathbf{P}_A^{(2,1)} \mathbf{M}_A^2) \mathbf{a}_A^{1+} \quad (\text{IV.22})$$

$$= (\mathbf{P}_A^{(1,2)} \mathbf{M}_A^1 + \mathbf{P}_A^{(2,1)} \mathbf{M}_A^2) \mathbf{a}_A^{2+} \quad (\text{IV.23})$$

The complete relation between the forces and the coupled accelerations of material 1 is obtained by adding equation (IV.19) to equation (IV.22),

$$\mathbf{F}_A^1 + \mathbf{P}_A^{(2,1)} \mathbf{F}_A^2 = (\mathbf{M}_A^1 + \mathbf{P}_A^{(2,1)} \mathbf{M}_A^2) \mathbf{a}_A^{1+} \quad (\text{IV.24})$$

where the first term on the left hand side of the equation corresponds to the nodal force associated with material 1, while the second term is the force transmitted by material 2 to material 1 through their interface; the respective mass and coupled accelerations are found on the right hand side. The relation for material 2 is obtained by adding equations (IV.20) to (IV.23),

$$\mathbf{P}_A^{(1,2)} \mathbf{F}_A^1 + \mathbf{F}_A^2 = (\mathbf{P}_A^{(1,2)} \mathbf{M}_A^1 + \mathbf{M}_A^2) \mathbf{a}_A^{2+} \quad (\text{IV.25})$$

The coupled accelerations for material 1 and material 2 are obtained from equations (IV.24) and (IV.25):

$$\mathbf{a}_A^{1+} = \left[ \mathbf{M}_A^1 + \mathbf{P}_A^{(2,1)} \mathbf{M}_A^2 \right]^{-1} (\mathbf{F}_A^1 + \mathbf{P}_A^{(2,1)} \mathbf{F}_A^2) \quad (\text{IV.26})$$

$$\mathbf{a}_A^{2+} = \left[ \mathbf{P}_A^{(1,2)} \mathbf{M}_A^1 + \mathbf{M}_A^2 \right]^{-1} (\mathbf{P}_A^{(1,2)} \mathbf{F}_A^1 + \mathbf{F}_A^2) \quad (\text{IV.27})$$

The general form for coupling multi-material accelerations can be expressed as follows:

$$\mathbf{a}_A^{i+} = \left[ \sum_j \mathbf{P}_A^{(j,i)} \mathbf{M}_A^j \right]^{-1} \left( \sum_j \mathbf{P}_A^{(j,i)} \mathbf{F}_A^j \right) \quad (\text{IV.28})$$

The final step in the acceleration coupling consists of updating the nodal accelerations:

$$\mathbf{a}_A^i = \mathbf{a}_A^{i+}.$$

### IV.C.2 Nodal Normals

The finite element formulation needs nodal normals in order to couple velocities and accelerations. These normals are obtained from two types of interfaces present in the nodal support: the mixed element interfaces, and the intra-element interfaces. The interface reconstruction algorithm provides interface normals for the mixed elements, however, intra-element normals need to be established. Element and intra-element normals are then averaged to obtain nodal normals. Note that element and intra-element normals relate pair of materials sharing the same interface, therefore, the resulting nodal normals exist only between adjacent materials.

The nodal normal between two materials that do not share the same interface is needed since these materials exchange momentum and force contributions. This inter-material normal is calculated at the nodal level by first finding the path with the smallest number of interfaces between the two materials, and then by averaging the nodal normals encountered on the path.

In order to simulate dynamic problems, finite element methods requires a time discretization, which can induce material interference despite the implementation of the velocity and acceleration coupling algorithm. For instance, assume that two materials separated by a void material approach each other. At a certain time step the volume of the void material is very small while the two solid materials are still uncoupled. At the end of the following time step, if the time step is too big, the two solid materials will occupy more volume than the void material allows, and as a result, they will overlap and create an interference. In order to solve this issue, the time step is recalculated according to the volume of the void material, the velocities of the two solid materials separated

by the void material, and the size of the elements in the nodal support. However, this solution presents an additional issue, which is associated with the time step size. In fact, while the correct time step size allows for the perfect coupling between the two materials in a nodal support, it can cause the void material of another nodal support to become very small. As a consequence, the size of the next time step will be very small, making the formulation inefficient. In addition, since the calculation of the size of the time step uses approximate values, the same problem can arise in the nodal support where the smallest time step was obtained. This problem is solved by introducing an *interface interception volume fraction* (IIVF) in the formulation. When the volume fraction of the void material is smaller than the interception volume, the two solid materials are considered to be in contact and a nodal normal that relates the two is created. This normal is obtained by averaging the normals of the two solid materials adjacent to the void material.

### Mixed elements normals

The interface reconstruction provides the positions, and therefore the normals, of the interfaces between pairs of materials inside mixed elements. Figure IV.5 displays a mixed element containing four materials with their respective interfaces and normals, where  $\hat{\mathbf{n}}_E^{(1,2)}$  is the normal between material 1 and material 2 in mixed element  $E$ . The nodal vectors associated with the nodes in mixed element  $E$  are updated with the above interfaces normals as follows:

$$\tilde{\mathbf{n}}_A^{(i,j)} = \sum_E [\tilde{\mathbf{n}}_A^{(i,j)} + SIGN(\hat{\mathbf{n}}_E^{(i,j)} \cdot \tilde{\mathbf{n}}_A^{(i,j)}) \hat{\mathbf{n}}_E^{(i,j)}] \quad (\text{IV.29})$$



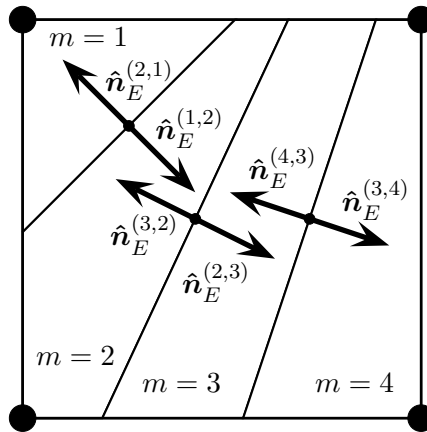


Figure IV.5: Mixed element normals

where  $\sum_E$  is the sum over the element in nodal support  $A$ , and  $\tilde{\mathbf{n}}_A^{(i,j)}$  corresponds to the non-unit nodal normal (or normal vector). The *SIGN* function guarantees that  $\hat{\mathbf{n}}_E^{(i,j)}$  points roughly in the same direction as  $\tilde{\mathbf{n}}_A^{(i,j)}$  before the update, and therefore that the two vectors do not cancel out during the update. Note that non-adjacent materials do not share a normal.

Equation (IV.29) is symmetric in its materials (i.e.  $\tilde{\mathbf{n}}_A^{(i,j)} = -\tilde{\mathbf{n}}_A^{(j,i)}$ ) in order to achieve the required nodal normal symmetry  $\mathbf{n}_A^{(i,j)} = -\mathbf{n}_A^{(j,i)}$ . However, the accuracy of interface normals can be improved by considering the volumes of each pair of materials.

### Intra-element normals

Intra-element normals are present between two pure elements, between two mixed elements, and between one mixed element and one pure element. Figure IV.6 shows element  $E$  with its *bottom*, *right*, *top*, and *left* elements, which are used to establish the intra-element normals. The nodes of element  $E$  are  $N1$ ,  $N2$ ,  $N3$ , and  $N4$ .

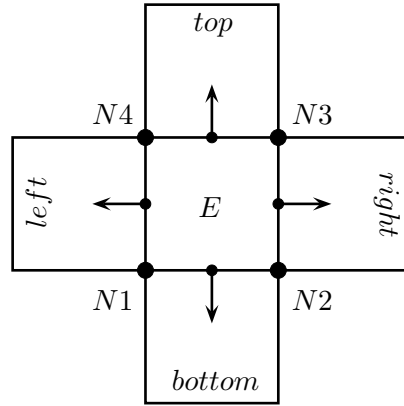


Figure IV.6: Scheme for intra-element normals

Intra-element interface normals between pure elements are obtained by first recognizing which material is present in the two elements that share the interface. If the material in element  $E$  of figure IV.6 differs from the material in one of the adjacent elements, the nodal vectors (i.e.  $\tilde{\mathbf{n}}$ ) of the nodes belonging to the interface are updated. Note that only the vectors of two nodes per intra-element interface are updated. For instance, assume that element  $E$  contains material  $a$  and element  $bottom$  contains material  $b$ . In this case, the nodal vectors are updated as follows:

$$\tilde{\mathbf{n}}_A^{(a,b)} = [\tilde{\mathbf{n}}_A^{(a,b)} + SIGN\left(\begin{pmatrix} 0 \\ -1 \end{pmatrix} \cdot \tilde{\mathbf{n}}_A^{(a,b)}\right) \begin{pmatrix} 0 \\ -1 \end{pmatrix}] \quad (\text{IV.30})$$

where  $\begin{pmatrix} 0 \\ -1 \end{pmatrix}$  represents the two dimensional normal for the interface between element  $E$  and element  $bottom$ , and  $A$  represents node  $N1$  and  $N2$ . The same procedure is applied to nodes  $N2$  and  $N3$  if element  $right$  contains material  $b$ :

$$\tilde{\mathbf{n}}_A^{(a,b)} = [\tilde{\mathbf{n}}_A^{(a,b)} + SIGN\left(\begin{pmatrix} 1 \\ 0 \end{pmatrix} \cdot \tilde{\mathbf{n}}_A^{(a,b)}\right) \begin{pmatrix} 1 \\ 0 \end{pmatrix}] \quad (\text{IV.31})$$

for nodes  $N3$  and  $N4$  in element *top*:

$$\tilde{\mathbf{n}}_A^{(a,b)} = [\tilde{\mathbf{n}}_A^{(a,b)} + SIGN(\begin{pmatrix} 0 \\ 1 \end{pmatrix} \cdot \tilde{\mathbf{n}}_A^{(a,b)}) \begin{pmatrix} 0 \\ 1 \end{pmatrix}] \quad (\text{IV.32})$$

and for nodes  $N4$  and  $N1$  in element *left*:

$$\tilde{\mathbf{n}}_A^{(a,b)} = [\tilde{\mathbf{n}}_A^{(a,b)} + SIGN(\begin{pmatrix} -1 \\ 0 \end{pmatrix} \cdot \tilde{\mathbf{n}}_A^{(a,b)}) \begin{pmatrix} -1 \\ 0 \end{pmatrix}] \quad (\text{IV.33})$$

Note that the procedure generates vectors that are symmetric in their materials, in fact,  $\tilde{\mathbf{n}}_A^{(a,b)}$  is updated with  $\begin{pmatrix} 0 \\ -1 \end{pmatrix}$  when the interface between element  $E$  and element *bottom* is analyzed, and  $\tilde{\mathbf{n}}_A^{(b,a)}$  is updated with  $\begin{pmatrix} 0 \\ 1 \end{pmatrix}$  when the interface between element *bottom* and element  $E$  is examined.

In order to generate an intra-element normal between two mixed elements, the materials that share the interface must be identified. Therefore, each mixed element has to provide the materials at the intra-element interface. Only two materials per mixed element are considered, which are the materials that share only one interface inside the mixed element (e.g. material 1 and material 4 for the example in figure IV.5). The numbers of these materials are stored inside an array when the algorithm creates the normals for the mixed elements (i.e.  $\hat{\mathbf{n}}$ ). Once the materials are identified, the algorithm uses the information from the surrounding elements to determine if they are at the interface being analyzed. Figure IV.7 shows the elements used to locate the material at the intra-element interface between element  $E$  and element *bottom* (see also figure IV.6). Assume that material  $a$  and material  $b$  are the two materials with one interface in mixed element  $E$ . The algorithm uses the following logic to establish the materials at the interface:

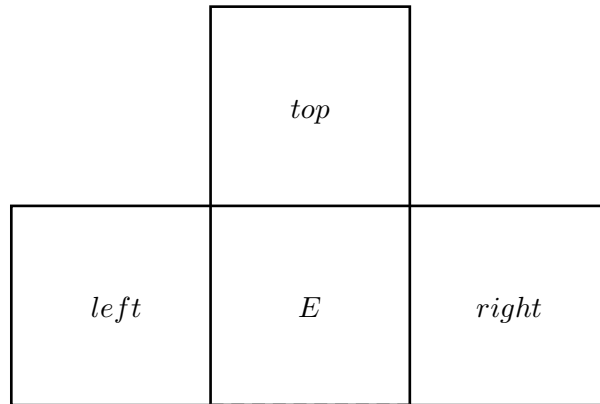


Figure IV.7: Elements used to locate the materials at the bottom intra-element interface

- If element *top* contains material *a* and not material *b*, then material *b* is at the interface.
- Else if element *top* contains material *b* and not material *a*, then material *a* is at the interface.
- Else:
  - $COUNT_a = 0$ .
  - $COUNT_b = 0$ .
  - If element *left* contains material *a*, then  $COUNT_a = COUNT_a + 1$ .
  - If element *left* contains material *b*, then  $COUNT_b = COUNT_b + 1$ .
  - If element *right* contains material *a*, then  $COUNT_a = COUNT_a + 1$ .
  - If element *right* contains material *b*, then  $COUNT_b = COUNT_b + 1$ .
  - If  $COUNT_a > COUNT_b$ , then material *a* is at the interface.
  - Else if  $COUNT_b > COUNT_a$ , then material *b* is at the interface.

- Else material  $a$  and material  $b$  are at the interface.

A similar scheme is applied to the mixed element *bottom* to establish the materials at the interface with element  $E$ . Figure IV.8 presents two examples where nodes  $N1$  and  $N2$  are connected to the intra-element interface between element  $E$  and element *bottom*. In both examples the mixed element *bottom* displays material 2 at the interface. Note that the above algorithm, when adapted to the element *bottom*, correctly predict this material.

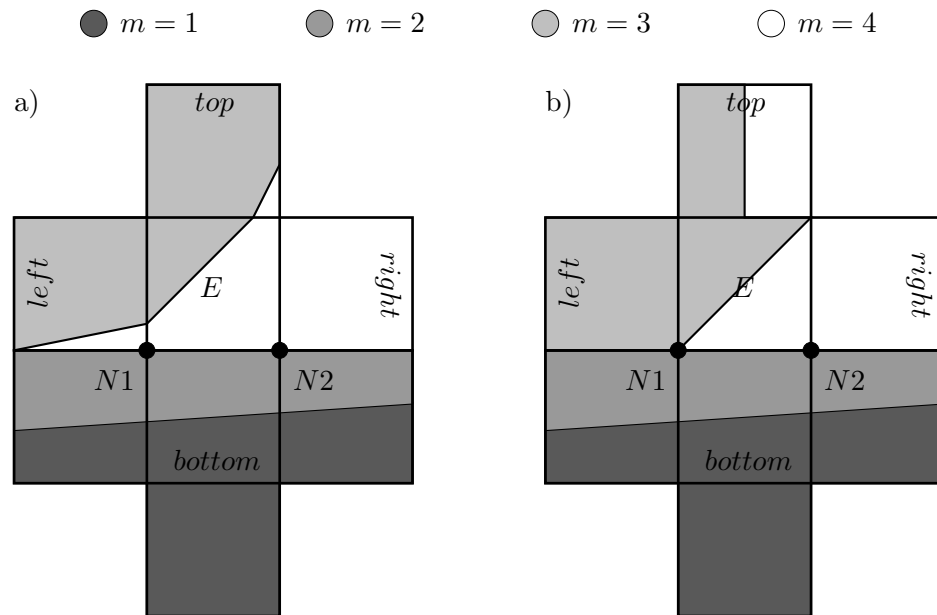


Figure IV.8: Examples of intra-element interfaces

The algorithm also correctly predicts material 4 to be at the interface for element  $E$  in example a). In example b) the algorithm predicts that material 3 and material 4 are at the interface, this is correct despite element  $E$  seems to have only material 4 at the interface. Inaccuracies in the interface geometry are sometimes present in mixed

elements due to the nature of the interface reconstruction, however, the above algorithm is not affected by them. In particular circumstances the prediction of the algorithm is incorrect. Figure IV.9 illustrate the problem with two examples.

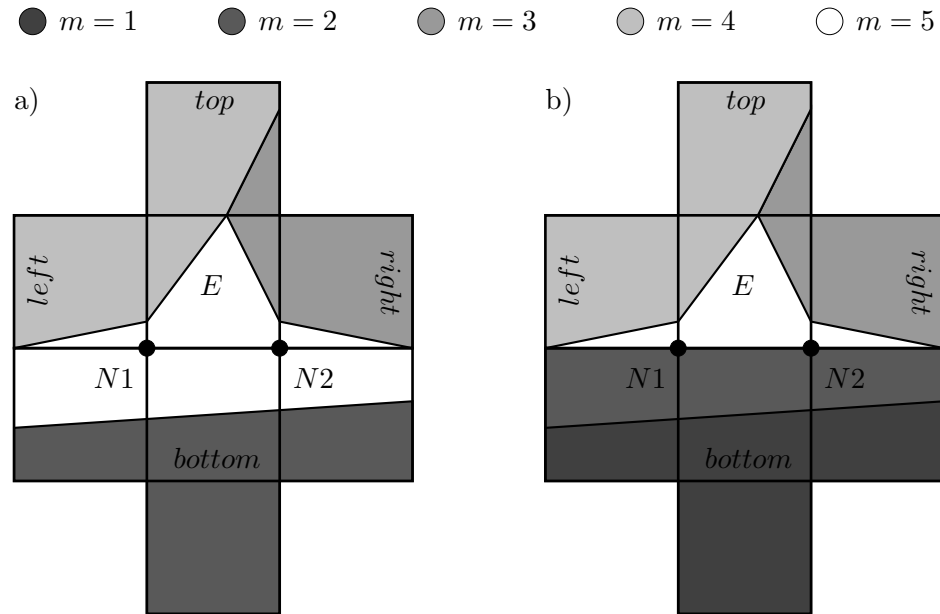


Figure IV.9: Particular cases where the material locator algorithm is inaccurate

In example a), element  $E$  contains materials 3, 4, and 5. In this case, the two materials considered for the intra-element interface are material 3 and material 4 because they have only one interface inside the mixed element. The algorithm predicts material 3 and material 4 to be at the  $N1 - N2$  interface of element  $E$ , while material 5 is at the same interface for element  $bottom$ . As a consequence, the resulting combination of materials at the interface (i.e. 3-5 and 4-5) is not representative. A similar case holds for example b), where the combinations of materials 3-2 and 4-2 is also incorrect. The problem is partially solved by neglecting the interface if the two elements have

at least one material in common. This solution solves the problem in example a) but not in example b), however, this is generally acceptable since the situation displayed in example a) is more common than the one in example b). Moreover, the configuration of example b) generally holds for just few time steps because as soon as one material from element  $E$  enters element *bottom*, or vice versa, the issue vanishes. As a consequence, the error introduced in the formulation is small. Nevertheless, while a smaller mesh size can address the problem, the accuracy of the algorithm can be improved if the following points are examined:

- All the materials inside the mixed elements are candidates to be the intra-element interface materials
- The volume fraction of the materials inside the elements is considered
- The elements on the corners of the mixed element are also analyzed (see figure IV.7)

Once the materials at the intra-element interface are located, the nodal vectors of the nodes connected to the interface are updated for each pair of materials. This is done similarly to equations (IV.30) - (IV.33); for instance, nodes  $N1$  and  $N2$  in the example b) of figure IV.8 are updated as follows:

$$\tilde{\mathbf{n}}_A^{(3,2)} = [\tilde{\mathbf{n}}_A^{(3,2)} + SIGN(\left(\begin{array}{c} 0 \\ -1 \end{array}\right) \cdot \tilde{\mathbf{n}}_A^{(3,2)}) \left(\begin{array}{c} 0 \\ -1 \end{array}\right)] \quad (\text{IV.34})$$

$$\tilde{\mathbf{n}}_A^{(4,2)} = [\tilde{\mathbf{n}}_A^{(4,2)} + SIGN(\left(\begin{array}{c} 0 \\ -1 \end{array}\right) \cdot \tilde{\mathbf{n}}_A^{(4,2)}) \left(\begin{array}{c} 0 \\ -1 \end{array}\right)] \quad (\text{IV.35})$$

where  $A$  represents nodes  $N1$  and  $N2$ . Note that also in this case equations (IV.34) and (IV.35) are symmetric in their materials. Finally, all four intra-element interfaces

follow the above scheme and algorithm to update the nodes of mixed element  $E$  when it is required.

Intra-element normals between a mixed element and a pure element are established when the pure element does not contain any of the mixed element materials. The scheme adopted to obtain intra-element normals between mixed elements is also used in this case, however, when the adjacent element is recognized as pure, also the pure element - mixed element relationship is considered to ensure material symmetry in the nodal vectors. For instance, assume that the bottom element in example b) of figure IV.8 is a pure element containing material 2. In this case, the vectors for nodes  $N1$  and  $N2$  are updated with equations (IV.34) and (IV.35) for the mixed element - pure element relationship, and the following is added for the pure element - mixed element relationship,

$$\tilde{\mathbf{n}}_A^{(2,3)} = [\tilde{\mathbf{n}}_A^{(2,3)} + SIGN\left(\begin{pmatrix} 0 \\ 1 \end{pmatrix} \cdot \tilde{\mathbf{n}}_A^{(2,3)}\right) \begin{pmatrix} 0 \\ 1 \end{pmatrix}] \quad (\text{IV.36})$$

$$\tilde{\mathbf{n}}_A^{(2,4)} = [\tilde{\mathbf{n}}_A^{(2,4)} + SIGN\left(\begin{pmatrix} 0 \\ 1 \end{pmatrix} \cdot \tilde{\mathbf{n}}_A^{(2,4)}\right) \begin{pmatrix} 0 \\ 1 \end{pmatrix}] \quad (\text{IV.37})$$

where  $A$  represents nodes  $N1$  and  $N2$ .

Finally, the nodal normals are obtained from the nodal vectors.

$$\mathbf{n}_A^{(i,j)} = \frac{\tilde{\mathbf{n}}_A^{(i,j)}}{|\tilde{\mathbf{n}}_A^{(i,j)}|} \quad (\text{IV.38})$$

### Inter-material normals

Inter-material normals establish the relationship between materials that do not share the same interface. These normals are needed to account for the momentum and force contributions from all the materials in the nodal support in equations (IV.14),



(IV.15), (IV.24), and (IV.25), which are used by equations (IV.18) and (IV.28) to couple the respective velocities and accelerations. For instance, part of the momentum of material 2 in example a) of figure IV.10 is transmitted to material 1 and vice versa. The average of the normals associated to the interfaces that separate the two materials is used to calculate the relationship:

$$\tilde{\mathbf{n}}_A^{(1,2)} = \mathbf{n}_A^{(1,3)} + \mathbf{n}_A^{(3,4)} + \mathbf{n}_A^{(4,2)} \quad (\text{IV.39})$$

$$\mathbf{n}_A^{(1,2)} = \frac{\tilde{\mathbf{n}}_A^{(1,2)}}{|\tilde{\mathbf{n}}_A^{(1,2)}|} \quad (\text{IV.40})$$

The normal  $\mathbf{n}_A^{(1,2)}$  is set to zero if one of the materials between material 1 and material 2 is a void material. The same is valid if two of the materials that share one of the interfaces between material 1 and material 2 separates. However, this is enforced only if the prescribed contact allows separation. The subsection IV.C.3 treats the separation condition.

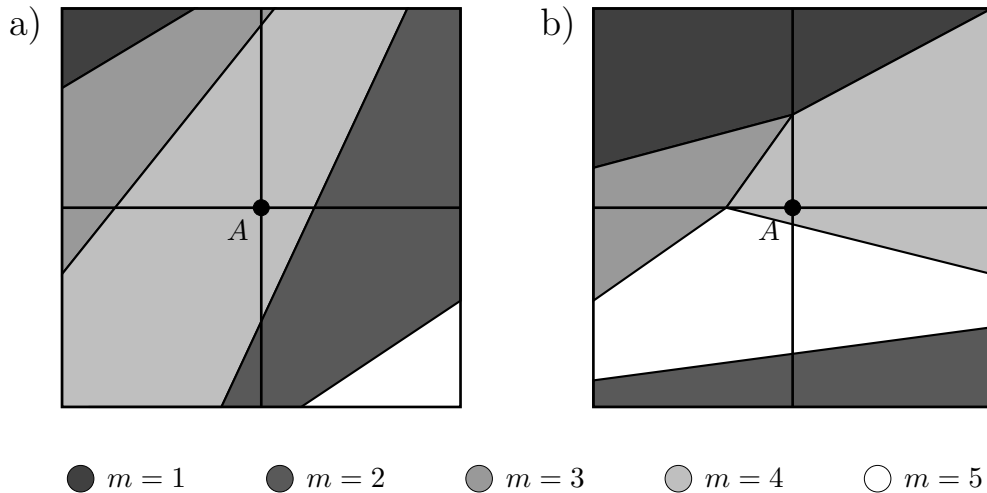


Figure IV.10: Examples of nodal support interfaces

When more than one path is available for two materials to exchange their

contribution, the path that provides the best interfaces alignment is chosen. For example, the normal between material 1 and material 2 in example b) of figure IV.10 can be achieved through materials 3 - 5 or materials 4 - 5. The alignment for the 1 - 3 - 5 - 2 path is:

$$ALIGN_{1352} = \mathbf{n}_A^{(1,3)} \cdot \mathbf{n}_A^{(3,5)} \mathbf{n}_A^{(3,5)} \cdot \mathbf{n}_A^{(5,2)} \quad (IV.41)$$

and for the 1 - 4 - 5 - 2 path is:

$$ALIGN_{1452} = \mathbf{n}_A^{(1,4)} \cdot \mathbf{n}_A^{(4,5)} \mathbf{n}_A^{(4,5)} \cdot \mathbf{n}_A^{(5,2)} \quad (IV.42)$$

If  $ALIGN_{1352} > ALIGN_{1452}$  the normal between materials 1 and material 2 is calculated similarly to equations (IV.39) and (IV.40):

$$\tilde{\mathbf{n}}_A^{(1,2)} = \mathbf{n}_A^{(1,3)} + \mathbf{n}_A^{(3,5)} + \mathbf{n}_A^{(5,2)} \quad (IV.43)$$

$$\mathbf{n}_A^{(1,2)} = \frac{\tilde{\mathbf{n}}_A^{(1,2)}}{|\tilde{\mathbf{n}}_A^{(1,2)}|} \quad (IV.44)$$

The path is not considered if a void material is present or if separation, when allowed, occurs at one of the interfaces. The normal  $\mathbf{n}_A^{(1,2)}$  is set to zero if all the paths contain either a void material or an interface that is separating.

### Interface Interception Volume Fraction

The *interface interception volume fraction* (IIVF) prevents the time step, which estimates the impact time between two colliding materials, from becoming extremely small. This is achieved by controlling the volume fraction of the void material present in the nodal support. If this value is smaller than IIVF the two solid materials separated by the void material are considered to be in contact and their nodal normal is calculated

as follows:

$$if \left( \frac{V_A^{void}}{V_A} < IIVF \right) \quad then \quad \mathbf{n}_A^{(i,j)} = \frac{\mathbf{n}_A^{(i,void)} + \mathbf{n}_A^{(void,j)}}{|\mathbf{n}_A^{(i,void)} + \mathbf{n}_A^{(void,j)}|} \quad (IV.45)$$

where  $i$  and  $j$  represent the two solid materials separated by the void material,  $V_A^{void}$  is the volume of the void material in the nodal support  $A$ , and  $V_A$  is the total volume of the nodal support  $A$ . The void material is eventually compressed out by the transport algorithm when it recalculates the volume of the materials in each element. In fact, any stress generated by the coupling of the two materials is “relaxed” until all the void material disappears from the elements. This is source of negligible error, especially when a small  $IIVF$  is selected by the user. The  $IIVF$  value for the simulations presented in section V is set to 5%.

The impact time is calculated when two materials in a nodal support are separated by a void material with a volume fraction greater than  $IIVF$ . Figure IV.11 shows the nodal support of  $A$  where the solid materials 1 and 2 are separated by the void material 2. The length and height of the nodal support is  $L$  and  $H$ , respectively, and the interfaces are defined by nodal normals (i.e. only one segment defines each interface inside the nodal support). For instance, assume that material 2 in the example of figure IV.11 is a void material, while material 1 and material 3 are solid materials. Vector  $\tilde{\mathbf{d}}$  is the average distance between material 1 and material 3 and it is calculated as follows:

$$\tilde{\mathbf{d}} = \mathbf{d} |\tilde{\mathbf{d}}| \quad (IV.46)$$

$$\mathbf{d} = \frac{\mathbf{n}_A^{(1,2)} + \mathbf{n}_A^{(2,3)}}{|\mathbf{n}_A^{(1,2)} + \mathbf{n}_A^{(2,3)}|} \quad (IV.47)$$

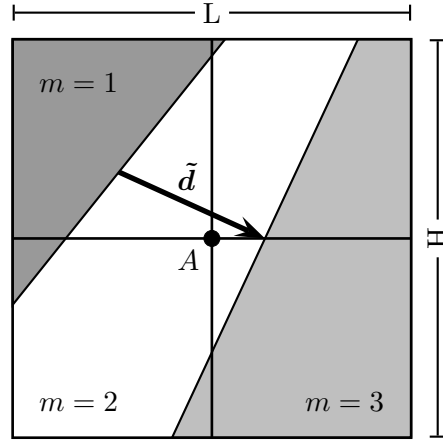


Figure IV.11: Two colliding materials

if  $\left( \left| \mathbf{d} \cdot \begin{pmatrix} 0 \\ 1 \end{pmatrix} \right| < \frac{L}{\sqrt{L^2 + H^2}} \right)$  then

$$|\tilde{\mathbf{d}}| = \frac{V_A^2}{L} \left| \mathbf{d} \cdot \begin{pmatrix} 0 \\ 1 \end{pmatrix} \right| \quad (\text{IV.48})$$

else

$$|\tilde{\mathbf{d}}| = \frac{V_A^2}{H} \left| \mathbf{d} \cdot \begin{pmatrix} 1 \\ 0 \end{pmatrix} \right|$$

where  $V_A^2$  is the volume of material 2 in the nodal support  $A$ . Next, the velocities of the two solid materials are projected onto  $\mathbf{d}$ ,

$$v_1^p = \mathbf{v}_A^1 \cdot \mathbf{d} \quad (\text{IV.49})$$

$$v_3^p = \mathbf{v}_A^3 \cdot \mathbf{d} \quad (\text{IV.50})$$

The following logic is used to calculate the impact time:

1. if  $(\text{SIGN}(v_1^p v_3^p) > 0)$  then

- $\Delta v^p = v_1^p - v_3^p$

- if  $(\Delta v^p > 0)$  then  $\Delta t_i = \frac{|\tilde{\mathbf{d}}|}{\Delta v^p}$

2. else if ( $v_1^p > 0$ ) then

- $\Delta v^p = v_1^p + v_3^p$
- $\Delta t_i = \frac{|\tilde{\mathbf{d}}|}{\Delta v^p}$

3. end if

4.  $\Delta t = \text{MIN}\{\Delta t, \text{MAX}(\Delta t_i, \Delta t_{min})\}$

where  $\Delta v^p$  is the difference in the projected velocity between the two solid materials,  $\Delta t_i$  is the time to impact,  $\Delta t$  is the current time step, and  $\Delta t_{min}$  is the minimum allowable time step that is specified by the user. When the two projected velocities have the same direction, point 1 calculates the difference in velocity between the two materials. If  $\Delta v^p$  is positive the two materials are approaching, therefore, the impact time is calculated. Point 2 calculates the impact time when the two materials travel in opposite directions and the velocity of material 1 is positive. Finally, point 4 updates the time step when necessary. The  $\Delta t_{min}$  value in the expression ensures that the time step does not become too small if an inadequate *IIVF* is prescribed.

Note that in the above calculation the direction of  $\mathbf{d}$ , along with the order in which  $v_1^p$  and  $v_3^p$  are used, must be respected. Also, the distance  $|\tilde{\mathbf{d}}|$  calculated in equation (IV.48) can be smaller than the actual value. However, this occurrence results in a smaller  $\Delta t_i$ , which does not introduce any error in the formulation.

### IV.C.3 Contact Enforcement

The purpose of the contact enforcement is to obtain the correct nodal velocities and accelerations for the prescribed contact. Therefore, equations (IV.18) and (IV.28)

are modified to enforce the separation condition and the fully bonded, frictionless slip, and slip with friction contacts.

### Separation condition

The separation condition is applied to every pair of solid materials in the nodal support, and it establishes if the two materials are separating. When the prescribed contact allows separation, the following is enforced:

$$\text{if } (\mathbf{n}_A^{(i,j)} \cdot \frac{\sum_E (\boldsymbol{\sigma}_{E_A}^i V_{E_A}^i + \boldsymbol{\sigma}_{E_A}^j V_{E_A}^j)}{\sum_E (V_{E_A}^i + V_{E_A}^j)} \mathbf{n}_A^{(i,j)} \geq 0) \text{ then } \mathbf{P}_A^{(i,j)} = \mathbf{0} \quad (\text{IV.51})$$

where  $i$  and  $j$  represent the two materials in contact,  $\boldsymbol{\sigma}_{E_A}^i$  is the stress of material  $i$  in element  $E$  for node  $A$ ,  $V$  is the volume, and  $\sum_E$  is the sum over the element in the nodal support. Equation (IV.51) calculates the traction at the interface using the volume weighted average of the stresses of the two materials in the nodal support, then, if the projection of the traction onto the interface normal is greater than zero, the projection matrix is zeroed. As a consequence, (IV.18) and (IV.28) do not couple the two materials. Finally, the transport algorithm introduces a void material to fill the gap created between the two solid materials when the two are uncoupled and move apart from each other. In case of non-adjacent materials, the projection matrix is also zeroed if one of the interfaces between the two solid materials separates or if a void material is present between the two.

Note that the outcome of the “if” statement in equation (IV.51) is the same for the relationships  $i \rightarrow j$  and  $j \rightarrow i$  since  $\mathbf{n}_A^{(i,j)}$  is equal to  $-\mathbf{n}_A^{(j,i)}$ .

### Fully bonded contact

The fully bonded contact couples the velocities and accelerations of two materials in all directions. This is achieved by setting the normal projection matrix equal to the identity matrix in equations (IV.18) and (IV.28),

$$\mathbf{P}_A^{(i,j)} = \mathbf{I} \quad (\text{IV.52})$$

Note that equation (IV.51) prevails over equation (IV.52) if separation is allowed.

### Frictionless slip contact

The frictionless slip contact enforces coupling only in the direction normal to the interface leaving the tangential direction unconstrained. This contact was used in the acceleration and velocity coupling examples, and the projection matrix for equations (IV.18) and (IV.28) is

$$\mathbf{P}_A^{(i,j)} = \mathbf{n}_A^{(i,j)} \otimes \mathbf{n}_A^{(i,j)} \quad (\text{IV.53})$$

where  $\mathbf{P}_A^{(i,i)} = \mathbf{I}$ . Note that also in this case equation (IV.51) replaces equation (IV.53) if separation is allowed.

### Slip with friction contact

The slip with friction contact modifies only the acceleration coupling of equation (IV.28). The velocity coupling is not modified because the velocities tangent to the interface do not change abruptly, moreover, the coupled accelerations correctly update the velocities during the time integration. Equation (IV.28) is modified as follows:

$$\mathbf{a}_A^{i+} = \left[ \sum_j (\mathbf{P}_A^{(j,i)} \mathbf{M}_A^j + \mu \mathbf{M}_A^{(i,j)}) \right]^{-1} \left[ \sum_j (\mathbf{P}_A^{(j,i)} \mathbf{F}_A^j + \mu \mathbf{F}_A^{(i,j)}) \right] \quad (\text{IV.54})$$

where  ${}^\mu \mathbf{F}_A^{(i,j)}$  is the friction force contribution from material  $j$  to material  $i$ , and  ${}^\mu \mathbf{M}_A^{(i,j)}$  is the friction mass contribution from materials  $j$  to material  $i$ .

The classical, or Coulomb, friction laws for static and kinetic cases are adopted. The static friction case is applied if the relative velocity tangent to the interface between two solid materials is zero, else, the kinetic case is implemented,

$$\mathbf{T}_A^{(i,j)} = \mathbf{I} - \mathbf{P}_A^{(i,j)} \quad (\text{IV.55})$$

$$\Delta^t \mathbf{v}_A^{(i,j)} = \mathbf{T}_A^{(j,i)} \mathbf{v}_A^j - \mathbf{T}_A^{(i,j)} \mathbf{v}_A^i \quad (\text{IV.56})$$

$$\begin{aligned} \text{if } (|\Delta^t \mathbf{v}_A^{(i,j)}| = 0) \text{ then } & \text{STATIC} \\ \text{else } & \text{KINETIC} \end{aligned} \quad (\text{IV.57})$$

where  $\mathbf{T}_A^{(i,j)}$  is the tangent matrix for the  $i - j$  interface, and  $\Delta^t \mathbf{v}_A^{(i,j)}$  is the relative tangential velocity between material  $j$  and material  $i$ .

The friction laws are based on the normal force present at the interface between two solid materials. This force depends on the area of the interface, the stress at the interface, and the direction normal to the interface. Moreover, it is calculated at the nodal level, and therefore the elements in the nodal support are considered. The area of the interface in the nodal support is calculated first. Consider the example in figure IV.12 where the nodal support  $A$  contains materials 1 and 2. The interface runs between the bottom pair of elements (intra-element interface), and it cuts the upper right element (mixed element interface). The area of the interface for the mixed element is obtained from the interface reconstruction, which provides the position of the interface between adjacent materials. The intra-element area exists only between pair of elements and it is equal to the surface that separates the two. In the example of figure IV.12, the nodal



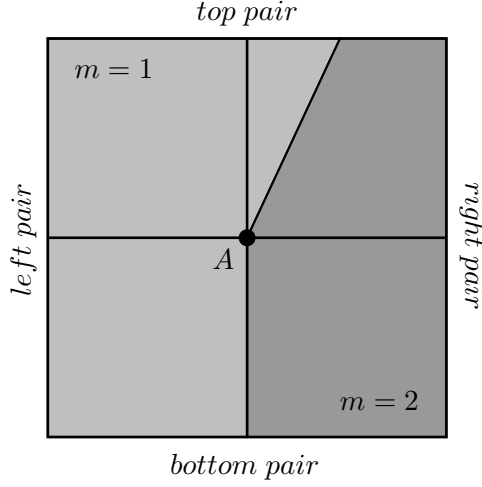


Figure IV.12: Interface and pairs of elements in nodal support  $A$

area of the interface between material 1 and material 2 for node  $A$  is

$$S_{A_{int}}^{(1,2)} = \frac{1}{N} \hat{S}_{A_{ur}}^{(1,2)} + \frac{1}{N_e} \bar{S}_{A_{bp}}^{(1,2)} \quad (\text{IV.58})$$

where  $N$  is the number of nodes per element,  $N_e$  is the number of nodes on the edge of the element,  $\hat{S}_{A_{ur}}^{(1,2)}$  is the area of the mixed element interface between material 1 and material 2 for the upper right element (i.e.  $ur$ ), and  $\bar{S}_{A_{bp}}^{(1,2)}$  represents the area of the intra-element interface between material 1 and material 2 in the nodal support  $A$  that runs between the bottom pair of elements (i.e.  $bp$ ). The general equation for the area of the interface in nodal support  $A$  between material  $i$  and material  $j$  is

$$S_{A_{int}}^{(i,j)} = \frac{1}{N} \sum_E \hat{S}_E^{(i,j)} + \frac{1}{N_e} \sum_p \bar{S}_{A_p}^{(i,j)} \quad (\text{IV.59})$$

$$p = \{\text{bottom pair}, \text{right pair}, \text{top pair}, \text{left pair}\} \quad (\text{IV.60})$$

where  $E$  are the elements in the nodal support. Note that  $\hat{S}_E^{(i,j)} = \hat{S}_E^{(j,i)}$ ,  $\bar{S}_{A_p}^{(i,j)} = \bar{S}_{A_p}^{(j,i)}$ , and  $S_A^{(i,j)} = S_A^{(j,i)}$ . Next, the volume weighted average stress of the two solid materials at the interface is calculated,

$$\sigma_{A_{int}}^{(i,j)} = \frac{\sum_{EM} (\sigma_{EM}^i V_{EM}^i + \sigma_{EM}^j V_{EM}^j) + \sum_p \left( \sum_{EI} \sigma_{EI}^i V_{EI}^i + \sum_{EJ} \sigma_{EJ}^j V_{EJ}^j \right)}{\sum_{EM} (V_{EM}^i + V_{EM}^j) + \sum_p \left( \sum_{EI} V_{EI}^i + \sum_{EJ} V_{EJ}^j \right)} \quad (\text{IV.61})$$

$$EM = \{E \mid \hat{S}_E^{(i,j)} \neq 0\} \quad (\text{IV.62})$$

$$EI = \{E \in p \mid \bar{S}_{A_p}^{(i,j)} \neq 0 \cap \text{Mat}_E^i \neq 0\} \quad (\text{IV.63})$$

$$EJ = \{E \in p \mid \bar{S}_{A_p}^{(i,j)} \neq 0 \cap \text{Mat}_E^j \neq 0\} \quad (\text{IV.64})$$

where  $\sigma_{A_{int}}^{(i,j)}$  is the volume weighted average stress around the interface between material  $i$  and material  $j$  in nodal support  $A$ , and  $\text{Mat}_E^i$  is the material flag that is equal 0 when material  $i$  is not present in element  $E$ . Finally, the normal force at the interface between the two materials is obtained using the nodal normals of equation (IV.38),

$$F_{A_{int}}^{(i,j)} = \mathbf{n}_A^{(i,j)} \cdot \sigma_{A_{int}}^{(i,j)} \mathbf{n}_A^{(i,j)} S_{A_{int}}^{(i,j)} \quad (\text{IV.65})$$

Note that equation (IV.65) is symmetric in its materials (i.e.  $F_{A_{int}}^{(i,j)} = F_{A_{int}}^{(j,i)}$ ). The procedure used to obtain  $F_{A_{int}}^{(i,j)}$  loses in accuracy as the interface in the nodal support becomes more irregular. This inaccuracy is attributed to the interface area calculation, which overestimates the effective area in irregular interfaces; moreover, the calculation is not suitable for three-dimensional problems. Further development is needed to address these issues.

In the *STATIC* case the two materials can either remain coupled or start to slip during the next time step. In order to establish which scenario is present, the forces tangent to the interface between the two solid materials are needed,

$${}^t \mathbf{F}_A^{(i,j)} = \mathbf{T}_A^{(j,i)} \mathbf{F}_A^j \quad (\text{IV.66})$$

where  ${}^t\mathbf{F}_A^{(i,j)}$  is force of material  $j$  tangent to the interface with material  $i$ . Next, the difference between the tangential forces at the interface is calculated.

$$\Delta {}^t\mathbf{F}_A^{(i,j)} = {}^t\mathbf{F}_A^{(i,j)} - {}^t\mathbf{F}_A^{(j,i)} \quad (\text{IV.67})$$

The magnitude of the tangential force difference of equation (IV.67) corresponds to the friction force needed to avoid slip between the two materials. The following equation is the maximal tangential force that can be generated by friction,

$$\mu_s \mathbf{F}_{Amax}^{(i,j)} = |F_{Aint}^{(i,j)}| \mu_s^{(i,j)} \frac{\Delta {}^t\mathbf{F}_A^{(i,j)}}{|\Delta {}^t\mathbf{F}_A^{(i,j)}|} \quad (\text{IV.68})$$

where  $\mu_s^{(i,j)}$  is the static coefficient of friction between material  $i$  and material  $j$ , and the tangential force difference of equation (IV.67) is used to define the direction. The maximal friction forces at the interface between the two materials is

$$\begin{aligned} \Delta \mu_s \mathbf{F}_{Amax}^{(i,j)} &= \mu_s \mathbf{F}_{Amax}^{(i,j)} - \mu_s \mathbf{F}_{Amax}^{(j,i)} \\ &= |F_{Aint}^{(i,j)}| \mu_s^{(i,j)} \frac{\Delta {}^t\mathbf{F}_A^{(i,j)}}{|\Delta {}^t\mathbf{F}_A^{(i,j)}|} - |F_{Aint}^{(j,i)}| \mu_s^{(j,i)} \frac{\Delta {}^t\mathbf{F}_A^{(j,i)}}{|\Delta {}^t\mathbf{F}_A^{(j,i)}|} \\ &= 2 |F_{Aint}^{(i,j)}| \mu_s^{(i,j)} \frac{\Delta {}^t\mathbf{F}_A^{(i,j)}}{|\Delta {}^t\mathbf{F}_A^{(i,j)}|} \end{aligned} \quad (\text{IV.69})$$

If the magnitude of the maximal friction force difference in equation (IV.69) is greater than the magnitude of the tangential force difference in equation (IV.68), the two materials are bonded, else, slip will occur in the next time step.

if  $(|\Delta^{\mu_s} \mathbf{F}_{Amax}^{(i,j)}| > |\Delta^t \mathbf{F}_A^{(i,j)}|)$  then

$$\mu \mathbf{F}_A^{(i,j)} = t \mathbf{F}_A^{(i,j)}$$

$$\mu \mathbf{M}_A^{(i,j)} = \mathbf{M}_A^j \mathbf{T}_A^{(j,i)}$$

(IV.70)

else

$$\mu \mathbf{F}_A^{(i,j)} = \mu_s \mathbf{F}_{Amax}^{(i,j)}$$

end

The bonding is enforced by setting the friction force and friction mass contributions equal to the tangential force and tangential mass of the contacting material, respectively. In fact, equation (IV.54) corresponds to equation (IV.28) with  $\mathbf{P}_A^{(j,i)} = \mathbf{I}$  when the statement of equation (IV.70) is true, which agrees with the fully bonded case presented earlier. This is also the only friction case where  $\mu \mathbf{M}_A^{(i,j)} \neq \mathbf{0}$ . When slip occurs, the normal force at the interface is unable to keep the two materials coupled, and the friction force contribution from material  $j$  to material  $i$  becomes the maximal friction force of equation (IV.68).

Also the *KINETIC* case presents two scenarios: in the next time step the two materials can retain a relative velocity, or the relative velocity can drop to zero. In order to establish which scenario is present, the frictionless relative velocity for the next time step is predicted,

$$\begin{aligned} \Delta^t \mathbf{v}_{Apre}^{(i,j)} &= \Delta^t \mathbf{v}_A^{(i,j)} + \left\{ \mathbf{T}_A^{(j,i)} \mathbf{a}_{Aunc}^j - \mathbf{T}_A^{(i,j)} \mathbf{a}_{Aunc}^i \right\} \Delta t \\ &= \Delta^t \mathbf{v}_A^{(i,j)} + \left\{ \mathbf{T}_A^{(j,i)} [\mathbf{M}_{Aunc}^j]^{-1} \mathbf{F}_{Aunc}^j - \mathbf{T}_A^{(i,j)} [\mathbf{M}_{Aunc}^i]^{-1} \mathbf{F}_{Aunc}^i \right\} \Delta t \end{aligned} \quad (\text{IV.71})$$

where  $\Delta^t \mathbf{v}_{Apre}^{(i,j)}$  is the predicted frictionless relative velocity between material  $j$  and ma-

terial  $i$ , and the subscript  $unc$  refers to the uncoupled quantity. Next, the maximal tangential force that can be generate by friction is calculated,

$$\mu_k \mathbf{F}_{Amax}^{(i,j)} = |F_{Aint}^{(i,j)}| \mu_k^{(i,j)} \frac{\Delta^t \mathbf{v}_{Apre}^{(i,j)}}{|\Delta^t \mathbf{v}_{Apre}^{(i,j)}|} \quad (\text{IV.72})$$

where  $\mu_k^{(i,j)}$  is the kinetic coefficient of friction between material  $i$  and material  $j$ , and the predicted frictionless relative velocity of equation (IV.71) is used to determine the direction. The following equation is the maximal velocity change between material  $i$  and  $j$  at node  $A$  that can be generated by friction.

$$\begin{aligned} \Delta^t \mathbf{v}_{Afrctn}^{(i,j)} &= \left\{ {}^t \mathbf{a}_{Afrctn}^j - {}^t \mathbf{a}_{Afrctn}^i \right\} \Delta t \\ &= \left\{ [\mathbf{M}_{Aunc}^j]^{-1} \mu_k \mathbf{F}_{Amax}^{(i,j)} - [\mathbf{M}_{Aunc}^i]^{-1} \mu_k \mathbf{F}_{Amax}^{(j,i)} \right\} \Delta t \\ &= [\mathbf{M}_{Aunc}^j]^{-1} (\mathbf{M}_{Aunc}^i + \mathbf{M}_{Aunc}^j) [\mathbf{M}_{Aunc}^i]^{-1} \mu_k \mathbf{F}_{Amax}^{(i,j)} \Delta t \end{aligned} \quad (\text{IV.73})$$

If the magnitude of the predicted frictionless relative velocity of equation (IV.71) is greater than the magnitude of the maximal friction velocity change of equation (IV.73), a relative velocity is maintained, else, it drops to zero.

$$\begin{aligned} \text{if } (|\Delta^t \mathbf{v}_{Apre}^{(i,j)}| > |\Delta^t \mathbf{v}_{Afrctn}^{(i,j)}|) \text{ then} \\ \mu \mathbf{F}_A^{(i,j)} &= \mu_k \mathbf{F}_{Amax}^{(i,j)} \\ \text{else} \end{aligned} \quad (\text{IV.74})$$

$$\mu \mathbf{F}_A^{(i,j)} = \frac{1}{\Delta t} \mathbf{M}_{Aunc}^i [\mathbf{M}_{Aunc}^i + \mathbf{M}_{Aunc}^j]^{-1} \mathbf{M}_{Aunc}^j \Delta^t \mathbf{v}_{Apre}^{(i,j)}$$

end

When a relative velocity is retained, the friction force contribution  $\mu \mathbf{F}_A^{(i,j)}$  becomes the maximal tangential force generated by friction. On the other hand, when the relative velocity drops to zero, the friction force contribution is calculated such that during the

next time steps it generates an acceleration for the two materials that combined cancel out the predicted relative velocity. In fact, if only the friction force contribution of the latter scenario is considered, the nodal force becomes

$$\mathbf{F}_A^i = \frac{1}{\Delta t} \mathbf{M}_{Aunc}^i [\mathbf{M}_{Aunc}^i + \mathbf{M}_{Aunc}^j]^{-1} \mathbf{M}_{Aunc}^j \Delta^t \mathbf{v}_{Apre}^{(i,j)} \quad (\text{IV.75})$$

and the relative velocity calculated from the forces generated by equation (IV.75) is

$$\left\{ {}^t \mathbf{a}_A^j - {}^t \mathbf{a}_A^i \right\} \Delta t = \left\{ [\mathbf{M}_{Aunc}^j]^{-1} \mathbf{F}_A^j - [\mathbf{M}_{Aunc}^i]^{-1} \mathbf{F}_A^i \right\} \Delta t = -\Delta^t \mathbf{v}_{Apre}^{(i,j)} \quad (\text{IV.76})$$

which cancels out equation (IV.71) zeroing the relative velocity in the next time step.

Note that the tangential direction is already included in  $\mathbf{F}_A^i$  since it corresponds to the friction force, and that  $\Delta^t \mathbf{v}_{Apre}^{(i,j)} = -\Delta^t \mathbf{v}_{Apre}^{(j,i)}$ .

The friction model presented in this subsection is limited to two solid material per nodal support. The algorithm needs further development in order to obtain the correct relative forces and velocities between more than two solid materials. Finally, note that also in this case  ${}^\mu \mathbf{F}_A^{(i,j)} = \mathbf{0}$  and  ${}^\mu \mathbf{M}_A^{(i,j)} = \mathbf{0}$  when equation (IV.51) is true.

## Chapter V

# Numerical Results

This chapter validates the X-FEM formulation by analyzing few problems including a bouncing cylinder, a sliding block, a Taylor anvil test, projectile penetration, and a high velocity shock compression of a steel powder. The bouncing cylinder problem emphasizes the different coupling and separation behaviors between the X-FEM formulation and the mean strain rate mixture theory; in addition, a small strain impact example is simulated using both theories and the results are compared to the analytical solution. The friction algorithm is tested in the sliding block example, where the results of the simulation are also compared to the analytical solution. The Taylor anvil test problem is simulated with frictionless slip, slip with friction, and fully bonded contact by the X-FEM formulation; three different simulations with different friction coefficients are presented for the slip with friction contact. The X-FEM solutions are then compared with the results of the mean strain rate mixture simulation and the results obtained from LS-DYNA, which employs a Lagrangian formulation. The importance of accurately modeling slip is underlined in the projectile penetration problem. In this case, the results are

compared with the mean strain rate mixture theory. Finally, in the high velocity shock compression of a steel powder problem, the robustness of the X-FEM algorithm is tested and some observations about the energy conservation properties of the formulation are made.

Note: the X-FEM and mixture theories images presented in this chapter are produced by Benson's research and development code Raven, the LS-DYNA images are produced by LS-PREPOST, all the problems are plane strain, and the units employed in the calculations are centimeters ( $cm$ ), microseconds ( $\mu s$ ), and grams ( $g$ ).

## V.A Bouncing Cylinder

### V.A.1 Example 1

The first example in this section compares the coupling and separation behaviors of the X-FEM simulation with the solution obtained from the mean strain rate mixture theory simulation. The problem consists of a cylinder made of copper that bounces on a block of steel situated below. The behavior of the two materials is considered to be purely elastic, and the cylinder travels towards the block with an initial velocity of  $0.1\text{ cm}/\mu s$ . The circular geometry was chosen to produce mixed elements containing interfaces with different slopes, and the velocity was selected to ensure the presence of the copper-steel interface in a good number of elements during the impact. Figure V.1 displays the initial conditions, where the left to right orientation defines axis  $x_1$ , the bottom to top orientation defines axis  $x_2$ ,  $V_2$  is the velocity in direction  $x_2$ , the cylinder has a diameter of  $2\text{ cm}$ , the block is constrained at the boundaries in the normal direction, and the mesh resolution is 10 elements per centimeter in both directions.



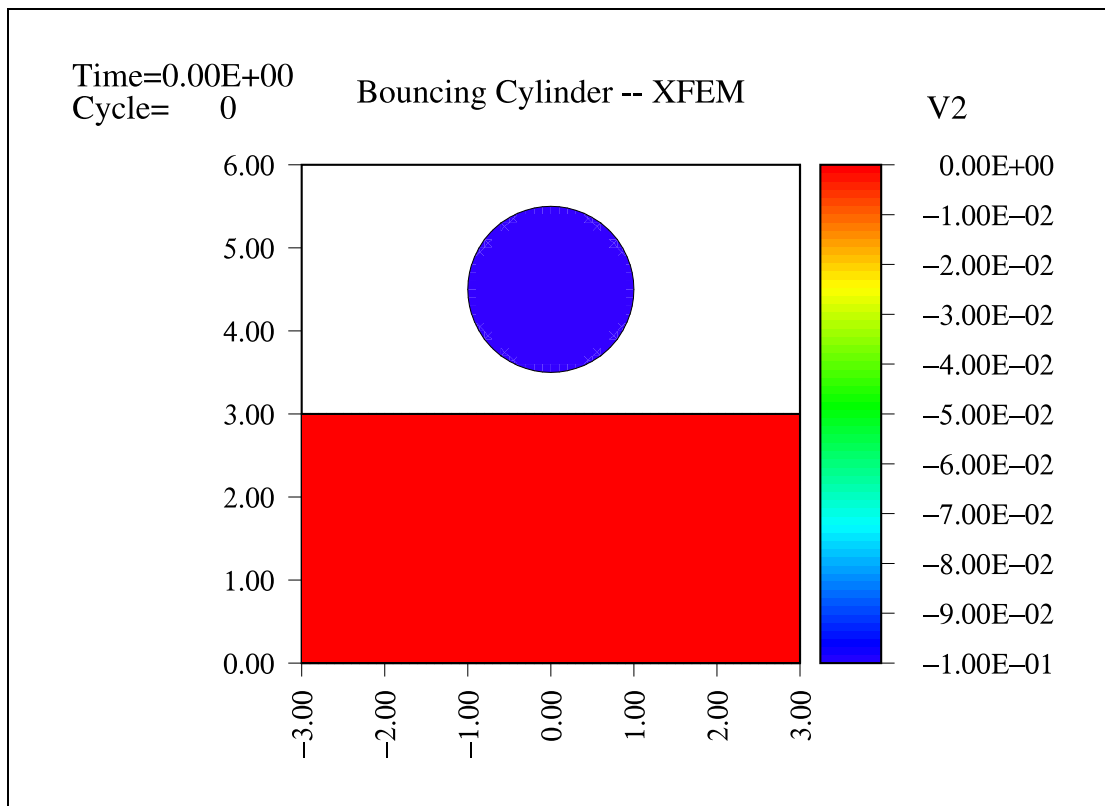


Figure V.1: Bouncing Cylinder: initial conditions

Table V.1: Bouncing Cylinder: material constants

	<b>Copper</b>	<b>Steel</b>
$\rho$	8.96 g/cm <sup>3</sup>	7.87 g/cm <sup>3</sup>
$K$	1.17 g/(cm $\mu$ s <sup>2</sup> )	1.63 g/(cm $\mu$ s <sup>2</sup> )
$G$	0.41 g/(cm $\mu$ s <sup>2</sup> )	0.79 g/(cm $\mu$ s <sup>2</sup> )

Table V.1 shows the values used in the constitutive equations for the two materials.

Figure V.2 displays the velocities in the  $x_2$ -direction for the mean strain rate mixture theory simulation prior to impact. It is noticeable how the velocities of the

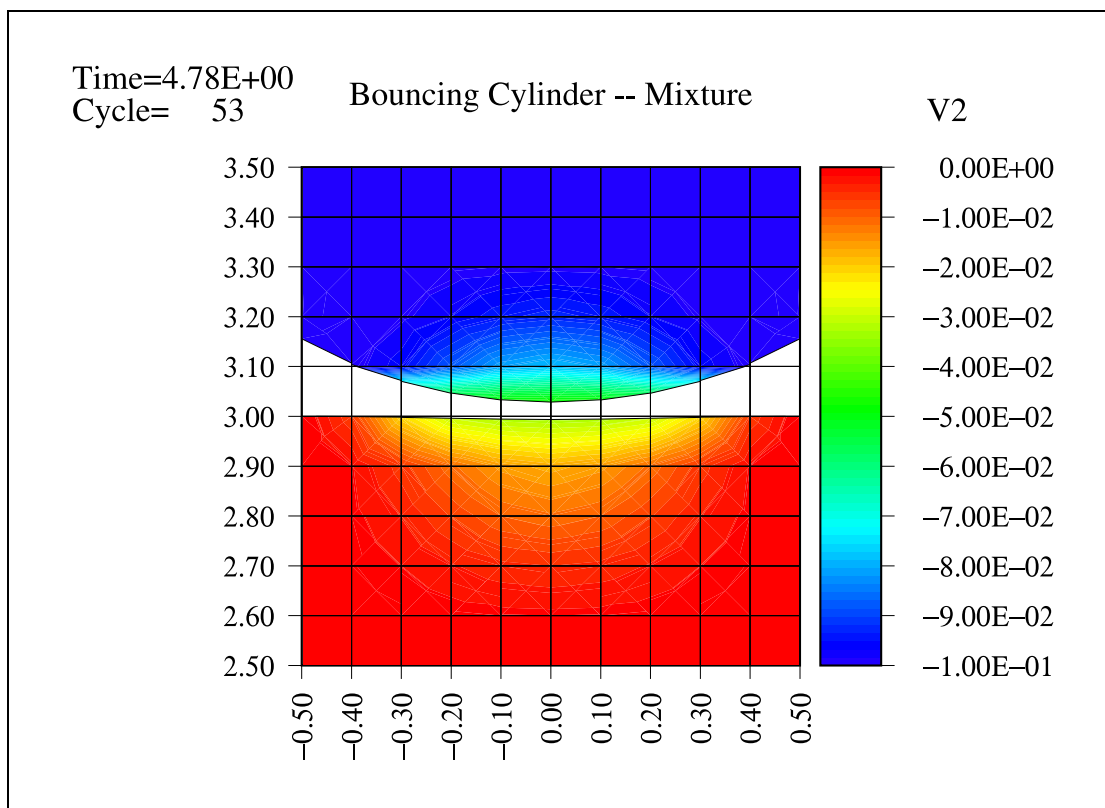


Figure V.2: Bouncing Cylinder: pre-impact (Mixture Theory)

two solid materials near the interface have changed even though the impact between the two has not yet occurred. This effect is caused by the lack of degrees of freedom that is characteristic of the mixture theories. In fact, since mixture theories can describe only one velocity field per node, the same nodal velocity is applied to all the materials present in the nodal support. In other words, the nodal velocity of the steel and copper materials change as soon as the copper material enters the nodal support containing the

steel material. As a result, the simulation loses accuracy.

Figure V.3 presents the same simulation at the same time step for the X-FEM formulation. In this case, the velocities of the two materials are unaffected because

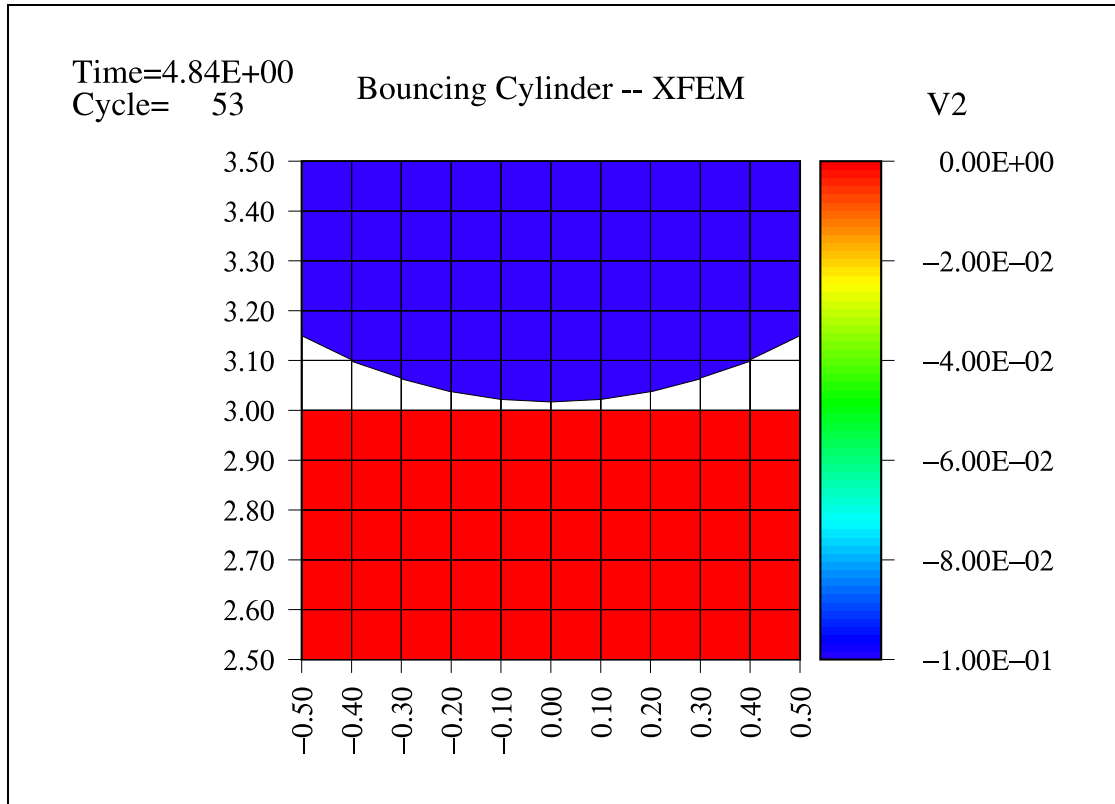


Figure V.3: Bouncing Cylinder: pre-impact (X-FEM)

the extra degrees of freedom allow the X-FEM formulation to describe the independent behavior of multiple materials in the same nodal support. As a consequence, the two materials do not influence each other. Nevertheless, the X-FEM formulation couples the two solid materials according to the prescribed contact when the volume fraction of the void material reaches the IIVF value. This coupling introduces a small error in the formulation because the two solid materials are coupled when they are still separated

by a void material. However, the error introduced in the X-FEM formulation is limited compared to the one found in the mixture theories; moreover, the X-FEM formulation allows the user to modify the IIVF value and therefore control the accuracy of the simulation.

Figure V.4 shows the pressure distribution in the materials for the mean strain rate mixture theory when the velocity at the copper-steel interface is zero (i.e. point of maximum penetration). While the location of maximum pressure is expected to be on

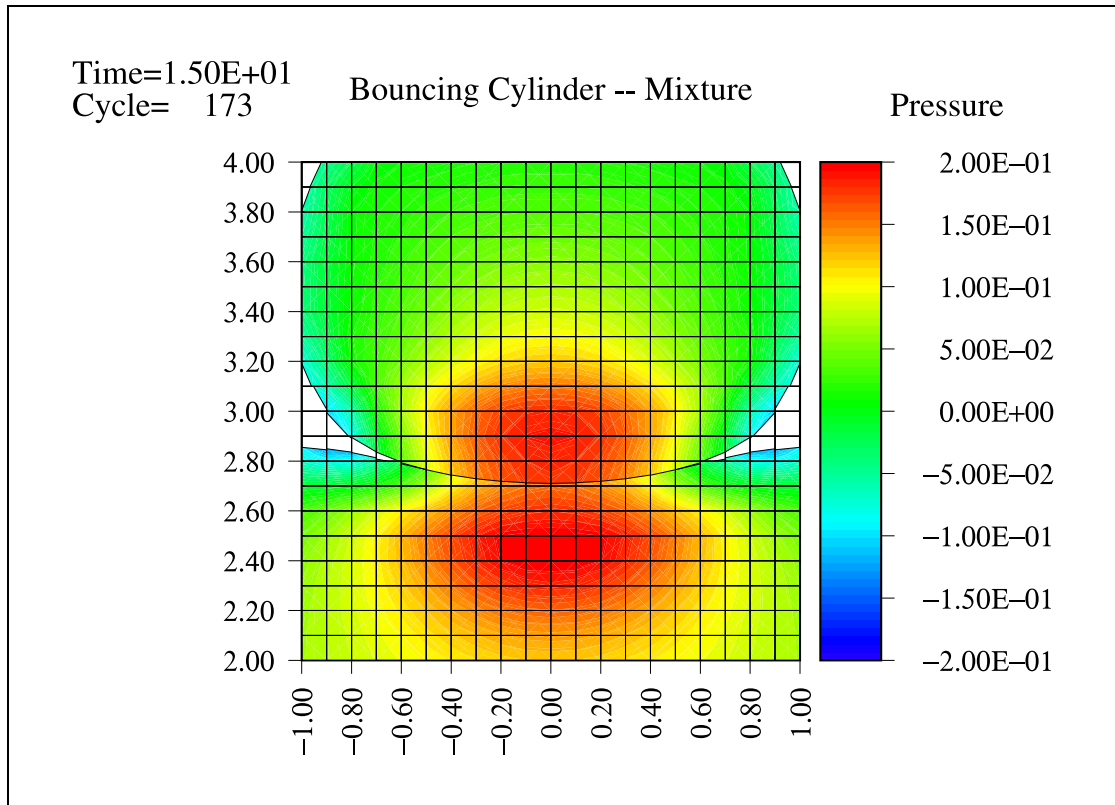


Figure V.4: Bouncing Cylinder: full-impact (Mixture Theory)

the vertical axis (i.e.  $x_1 = 0$ ) crossed with the interface, the figure displays this location to be on the vertical axis but offset by two elements with respect to the interface. This

behavior is due to the limitation of the mixture theory. Consider the mixed elements that contain the steel material and where the copper material is about to enter. As soon as the copper material enters the mixed elements, the velocity of the two materials changes and their pressure increases. Moreover, the pressures of the adjacent pure elements containing the two solid materials also increases. The void collapse algorithm implemented with the mean strain rate mixture theory (see III.B), however, compresses the void material out of the mixed elements by relaxing the stresses, and therefore the pressure, of the two solid materials. As a result, the pressure of the materials inside the mixed elements is lower than the one present in the adjacent pure elements containing the same materials. Note that a similar behavior is also observed during separation. In fact, during separation, the solid materials belonging to the same nodal support remain coupled even when they are divided by a void material; then, the separation algorithm relaxes the stresses inside the mixed elements by introducing more void material. This operation is executed until only one solid material is left in the nodal support, therefore, the two solid materials are independent. As a result, errors are introduced in the mixture theory simulation as long as the two solid materials share the same nodal support.

Figure V.5 shows the same simulation for the X-FEM formulation. This simulation emphasizes how the error introduced in the X-FEM formulation by the IIVF coupling effect is small compared to the error found in the mixture theory simulation. In fact, the results are more accurate and the pressure reaches its peak at the interface as expected. Note that the IIVF coupling effect occurs also during separation, however, the inaccuracies introduced in the simulation are as small as for the impact simulation.

Figure V.6 displays the prediction of the mean strain rate mixture theory with-

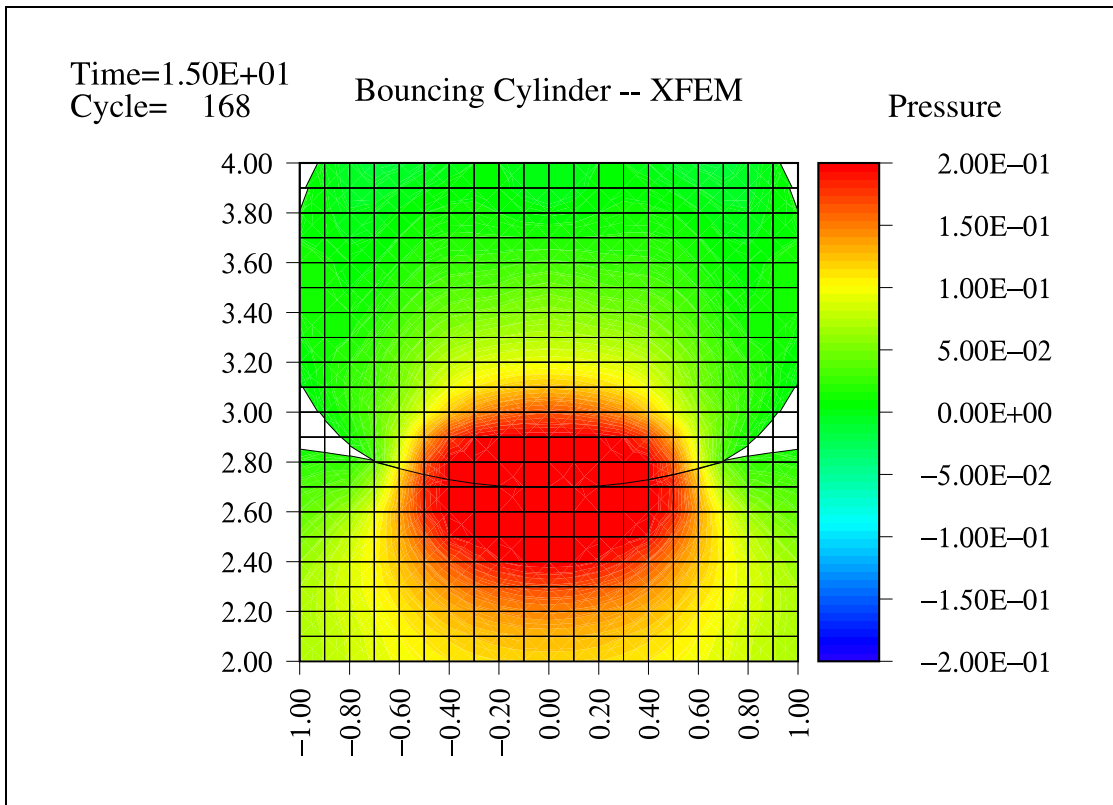


Figure V.5: Bouncing Cylinder: full-impact (X-FEM)

out the separation algorithm when the cylinder moves away from the block. The materials became fully bonded during impact and do not separate when tension is present at the interface.

Finally, figure V.7 shows the same scenario with the X-FEM formulation prediction. In this case, the separation between the two materials is clean and representative. Note that figure V.6 and figure V.7 display the same time step.

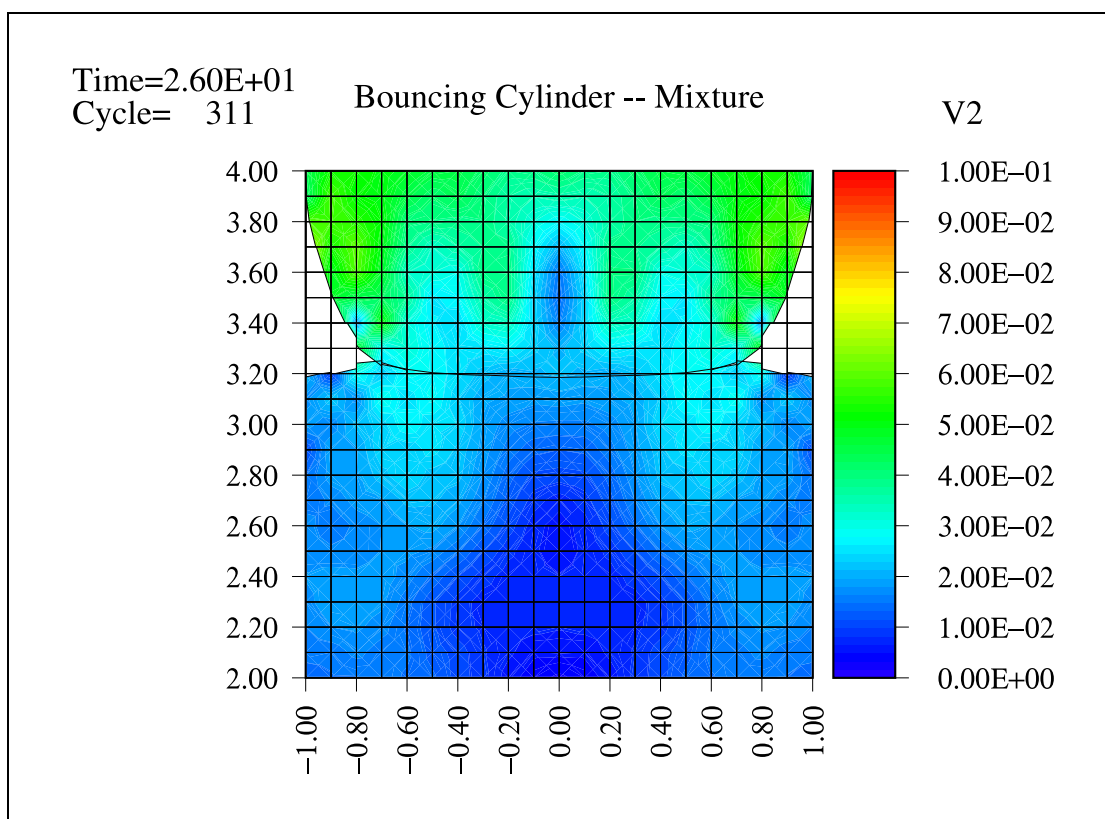


Figure V.6: Bouncing Cylinder: separation (Mixture Theory)

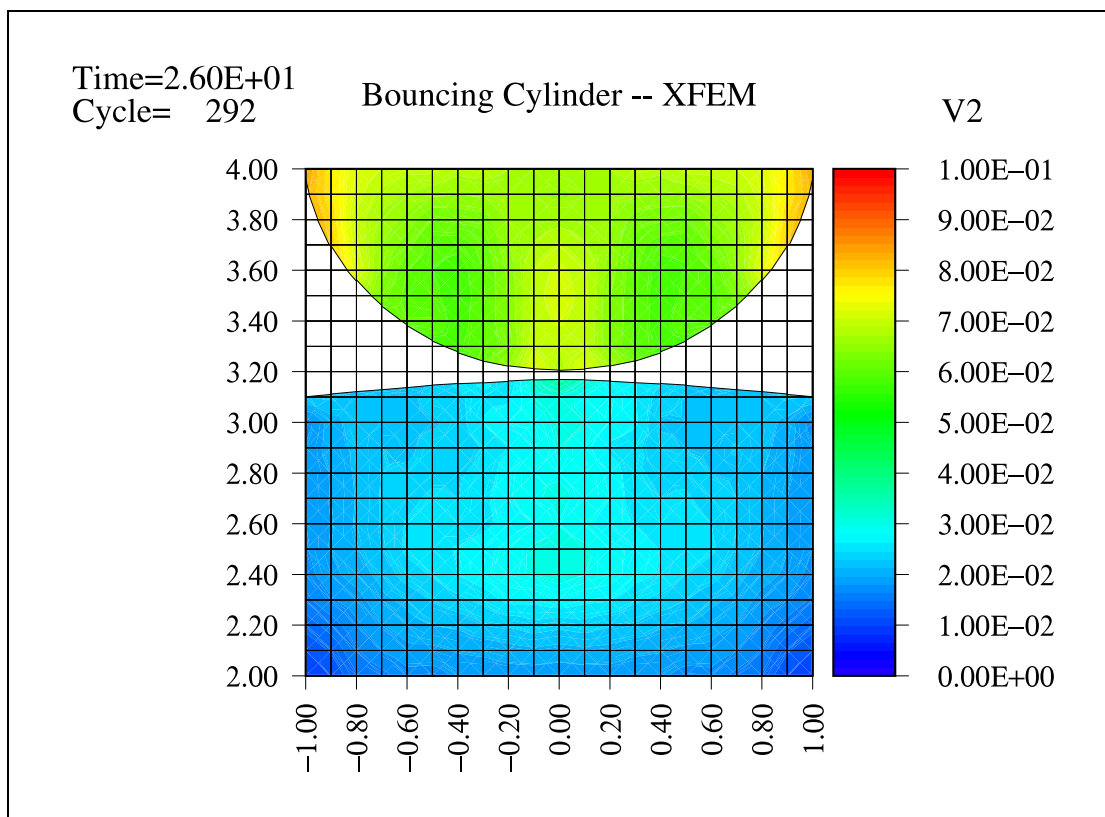


Figure V.7: Bouncing Cylinder: separation (X-FEM)



### V.A.2 Example 2

In the second example, the analytical solution for a line contact between a cylinder and a plate is compared to the X-FEM and the mixture theory simulations. The analytical solution is obtained from the two dimensional contact of cylindrical bodies presented in Johnson [17]. In the solution, the compression  $\delta$  in the  $x_2$ -direction as a function of the  $x_1$  coordinate is considered quadratic. Johnson obtains the Hertz' approximation by treating the displacement of each cylinder as an elastic half-space. Moreover, the theory for a line loading of an elastic half-space is used to calculate the pressure distribution on the contact area. The plate-cylinder contact problem is solved by letting the radius of one cylinder go to infinity. The stresses along the vertical axis of symmetry of the cylinder for plain strain problems provided by Johnson [17] are

$$\sigma_1(x_2, P) = -\frac{p_o(P)}{a(P)} \{(a^2(P) + 2x_2^2)(a^2(P) + x_2^2)^{-\frac{1}{2}} - 2x_2\} \quad (\text{V.1})$$

$$\sigma_2(x_2, P) = -p_o(P)a(P)(a^2(P) + x_2^2)^{-\frac{1}{2}} \quad (\text{V.2})$$

$$p_o^2(P) = \frac{PE^*}{\pi R} \quad (\text{V.3})$$

$$a^2(P) = \frac{4PR}{\pi E^*} \quad (\text{V.4})$$

$$\frac{1}{E^*} = \frac{1 - \nu_{copper}^2}{E_{copper}} + \frac{1 - \nu_{steel}^2}{E_{steel}} \quad (\text{V.5})$$

where  $p_o$  is the maximum pressure,  $a$  is half the contact width,  $P$  is the load on the contact area,  $R$  is the radius of the cylinder,  $\nu$  is the Poisson's ration, and  $E$  is the Young's modulus. The compression in  $x_2$  is found by integrating the strain  $\epsilon_2(x_2)$  over the cylinder diameter,

$$\delta(P) = \int_0^{2R} \epsilon_2(x_2, P) dx_2 \quad (\text{V.6})$$

$$\epsilon_2(x_2, P) = \frac{1 - \nu_{copper}^2}{E_{copper}} \left\{ \sigma_2(x_2, P) - \frac{\nu_{copper}}{1 - \nu_{copper}} \sigma_1(x_2, P) \right\} \quad (\text{V.7})$$

The elastic strain energy is calculated as follows:

$$U_e = \int P d\delta(P) \quad (\text{V.8})$$

The load on the contact area is obtained by iterating equation (V.8) until  $U_e$  matches the kinetic energy  $U_k$ ,

$$U_k = \frac{1}{2} M_{cyl.} v_{cyl.}^2 \quad (\text{V.9})$$

where  $M$  is the mass and  $v$  the velocity of the cylinder. The compression  $\delta$  and the half contact width  $a$  are then obtained from equations (V.6) and (V.4), respectively, and the results are used to validate the simulations. The equations provided by Johnson [17] require the contact to be frictionless and that  $a \ll R$ . The first requirement cannot be satisfied by the mixture theory, however, it is satisfied by the X-FEM formulation by imposing the frictionless contact. In order to satisfy the second requirement, the initial velocity of the cylinder is set to  $0.001 \text{ cm}/\mu\text{s}$ , which results in  $a = 0.08 \text{ cm}$  and  $\delta = -0.0075 \text{ cm}$ . The 8% ratio between the half contact width and the radius is relatively large, however, it still allows a good evaluation of the simulation's results with the employment of a reasonable mesh size. The mesh resolution for the simulations is increased to 50 elements per centimeter in both directions, and the lower boundary is moved to  $-1 \text{ cm}$  to better represent the infinitely thick block.

Figure V.8 displays the pressure distribution in the contact region when the interface reaches the lowest point in the mixture theory simulation. The inaccuracy of the pressure distribution is caused by the error observed in figure V.2, which also influences the result by preventing the contact between the two solid materials. In this

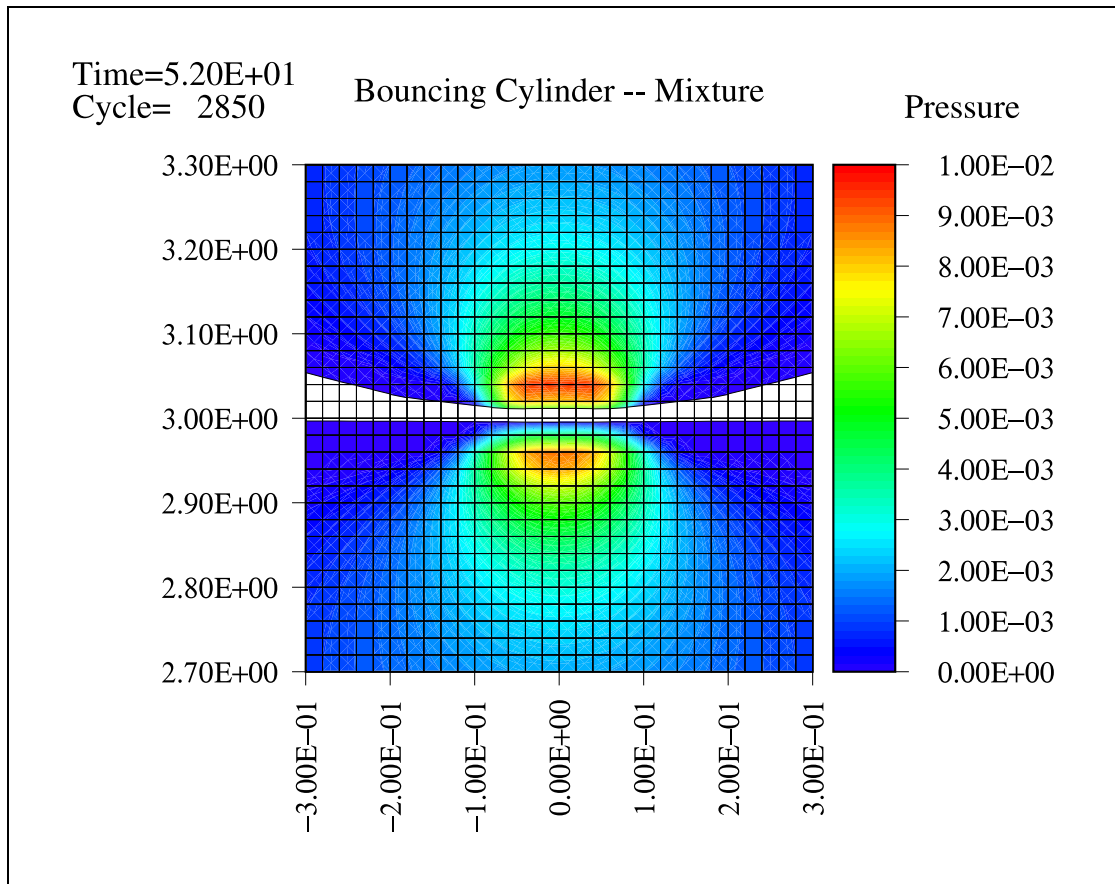


Figure V.8: Bouncing Cylinder: maximum contact (Mixture Theory)

case, the two materials do not come into contact because of the low impact velocity. The value of the deformation  $\delta$  is observed to be  $-0.0075\text{ cm}$  and agrees with the analytical solution, however, the lack of contact makes the reading of  $a$  impracticable.

Figure V.9 shows the results of the X-FEM simulation. In this case, the contact between the two materials is established, and the pressure distribution is well represented. The value of  $\delta$  is  $-0.0076\text{ cm}$ , and the half contact width  $a$  is  $0.08\text{ cm}$ ; both results agree with the analytical solution. Note that because of the low speed of the impact, it was possible to set IIVF to 0.05%, which minimized the coupling effect in the X-FEM

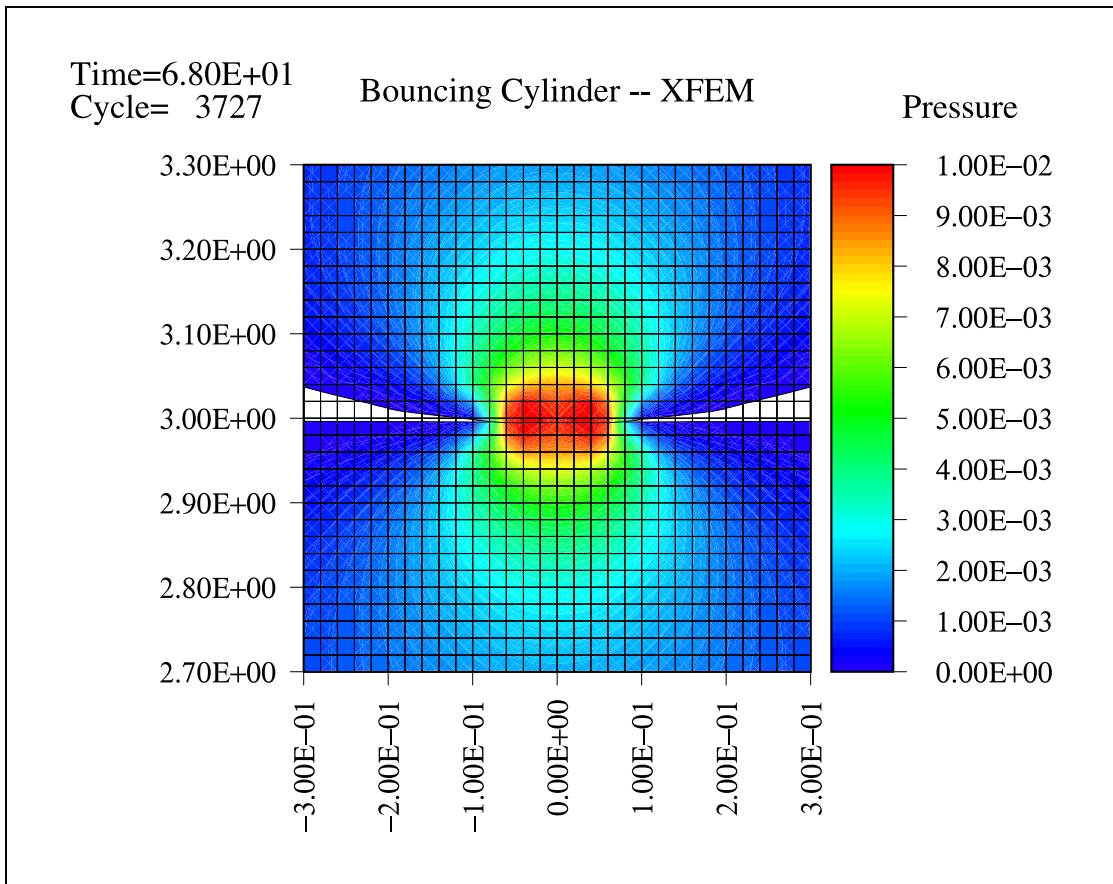


Figure V.9: Bouncing Cylinder: maximum contact (X-FEM)

simulation. Future work, however, aims to reduce the dependency between the coupling effect and the IIVF by compressing out the void material from the nodal support when the prescribed IIVF is reached. It is worth noting that the interface reaches its lowest point earlier in the mixture theory simulation than in the X-FEM simulation. This is a consequence of the impact occurring earlier in the mixture theory because taking place as soon as the two solid materials share the same nodal support. In the X-FEM simulation, however, the coupling occurs when the materials are almost in contact, generating more accurate results. Finally, notice that the values are extrapolated from elements with

length and width of  $0.02\text{ cm}$ , and that the value of  $a$ , in the X-FEM simulation, contains exactly four elements.

## V.B Sliding Block

This example tests the friction portion of the algorithm. A block made of steel travels towards a  $0.98\text{ cm}$  gap made by two parallel rigid plates. The height of the block is  $1\text{ cm}$ , its width is  $5\text{ cm}$ , and the longitudinal extremities are rounded with a diameter of  $1\text{ cm}$ . The ends of the rigid plates that face the block are rounded with a diameter of  $4\text{ cm}$ . The round geometry was chosen in order to avoid sharp corners on the sliding

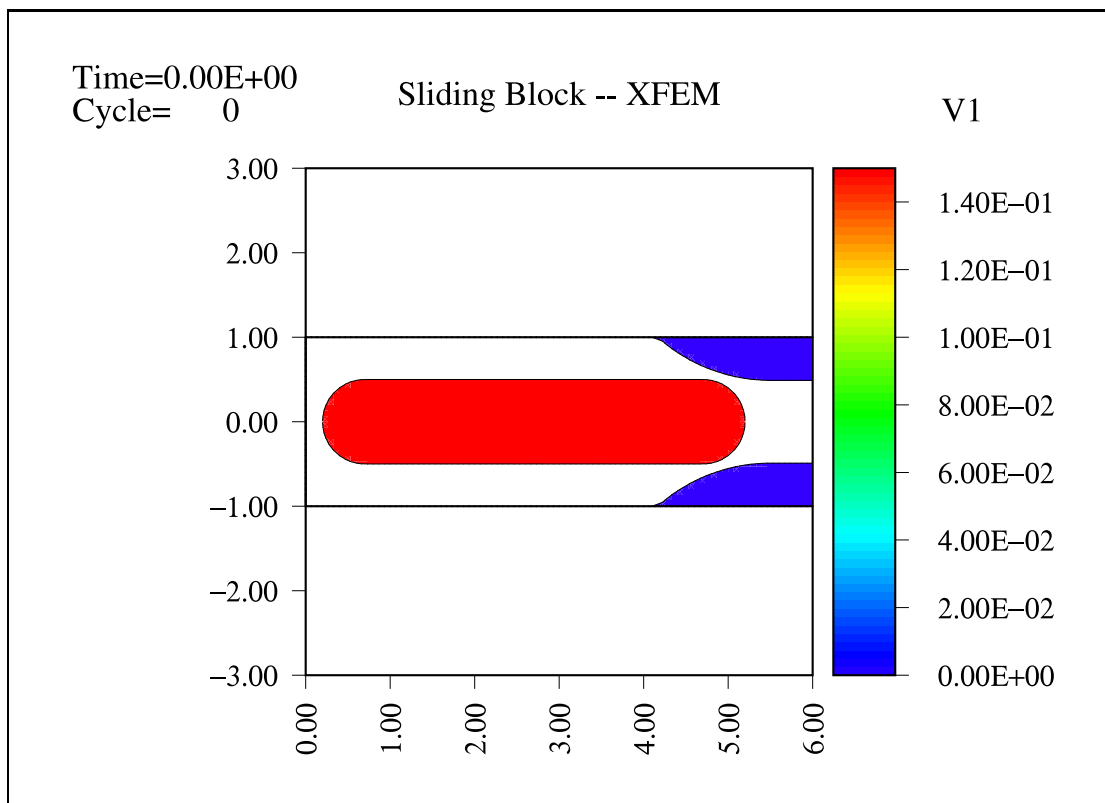


Figure V.10: Sliding Block: initial conditions

surface. The initial velocity of the block is of  $0.15 \text{ cm}/\mu\text{s}$ , and the static and kinetic friction coefficients are  $\mu^s = \mu^k = 0.2$ . Figure V.10 shows the initial conditions, where the top and bottom boundaries are fully constrained, and the mesh resolution is 15 elements per centimeter in both directions. The block and the plates behavior is purely elastic. Table V.2 displays the materials constants for the two solid materials, where the

Table V.2: Sliding Block: material constants

	<b>Steel</b>	<b>Rigid Plates</b>
$\rho$	$7.87 \text{ g}/\text{cm}^3$	$78.7 \text{ g}/\text{cm}^3$
$K$	$1.63 \text{ g}/(\text{cm } \mu\text{s}^2)$	$16.3 \text{ g}/(\text{cm } \mu\text{s}^2)$
$G$	$0.79 \text{ g}/(\text{cm } \mu\text{s}^2)$	$7.9 \text{ g}/(\text{cm } \mu\text{s}^2)$

rigid body behavior of the plates is simulated by setting their constants to ten times the values for the steel.

The calculation of analytical solution begins when the block is entirely between the two rigid plates. Figure V.11 shows the problem after  $38.7 \mu\text{s}$ . At this point, the average velocity of the block is  $0.107 \text{ cm}/\mu\text{s}$ , and its centroid is at  $8.03 \text{ cm}$ . The analytical solution is used to predict the stopping point of the block,

$$\epsilon_{22} = \frac{1 \text{ cm} - 0.98 \text{ cm}}{1 \text{ cm}} = -0.02 \quad (\text{V.10})$$

$$\epsilon_{11} = -\epsilon_{22} \nu = 0.0058274 \quad (\text{V.11})$$

$$\sigma_{22} = -\frac{E \nu}{(1 + \nu)(1 - 2 \nu)}(\epsilon_{11} + \epsilon_{22}) + \frac{E}{(1 + \nu)}\epsilon_{22} = -0.0472375 \frac{\text{g}}{\text{cm } \mu\text{s}^2} \quad (\text{V.12})$$

$$A = 4(1 + \epsilon_{11}) = 4.0233 \text{ cm}^3 \quad (\text{V.13})$$

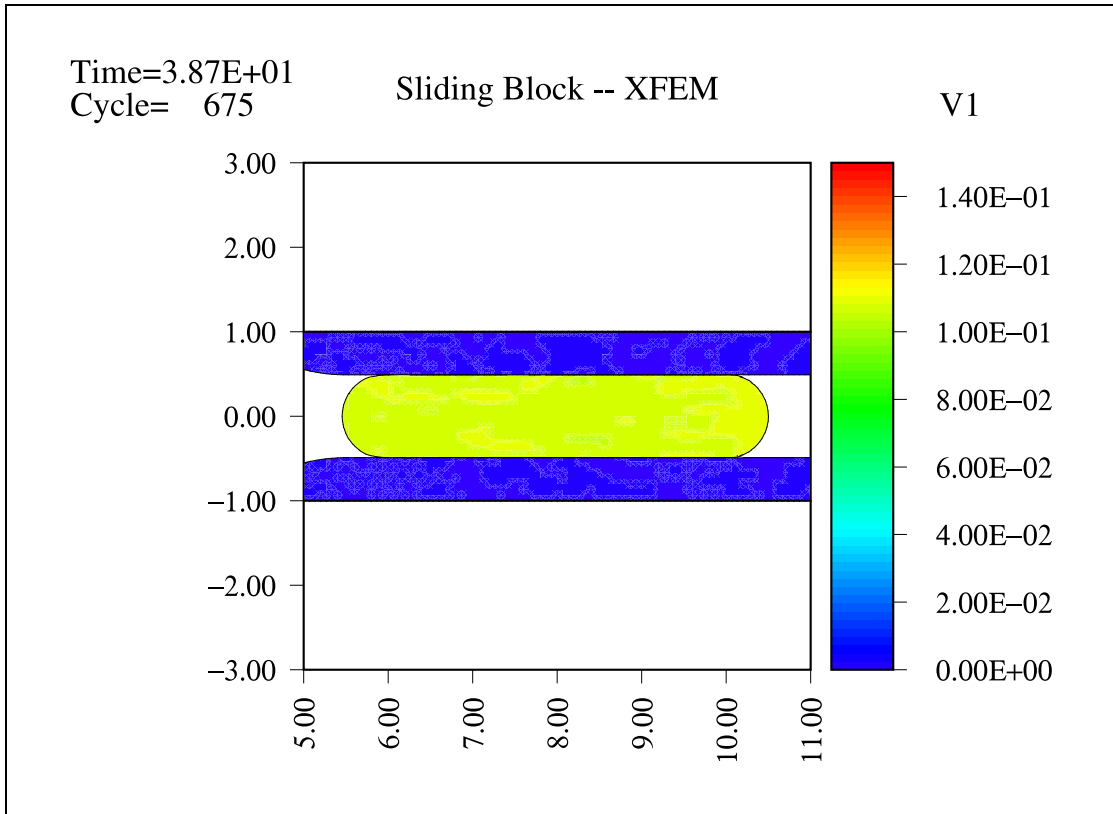


Figure V.11: Sliding Block: begin calculation

$$F^{frctn} = |2 A \sigma_{22} \mu| = 0.07602044 \frac{g \text{ cm}}{\mu s^2} \quad (\text{V.14})$$

$$M = (4 + 0.5^2 \pi) \rho = 37.6610835 \text{ g} \quad (\text{V.15})$$

$$a = \frac{F^{frctn}}{M} = 0.0020185 \frac{\text{cm}}{\mu s^2} \quad (\text{V.16})$$

$$\Delta x_1 = \frac{(0.107 \frac{\text{cm}}{\mu s})^2}{2a} = 2.84 \text{ cm} \quad (\text{V.17})$$

$$x_1^{final} = 8.03 \text{ cm} + \Delta x_1 = 10.87 \text{ cm} \quad (\text{V.18})$$

where  $\epsilon_{11}$  and  $\epsilon_{22}$  are the strains in the respective  $x_1$  and  $x_2$  directions,  $\sigma_{22}$  is the stress in direction  $x_2$ ,  $E$  and  $\nu$  are the Young's modulus and Poisson's ratio, respectively,  $A$  is the contact area on one side of the block,  $F^{frctn}$  is the friction force,  $\mu = \mu^s = \mu^k$  is the

friction coefficient,  $M$  is the mass of the block, and  $x_1^{final}$  is the final middle position of the block in direction  $x_1$ .

Figure V.12 shows the block after it stopped. The simulation predicts that the

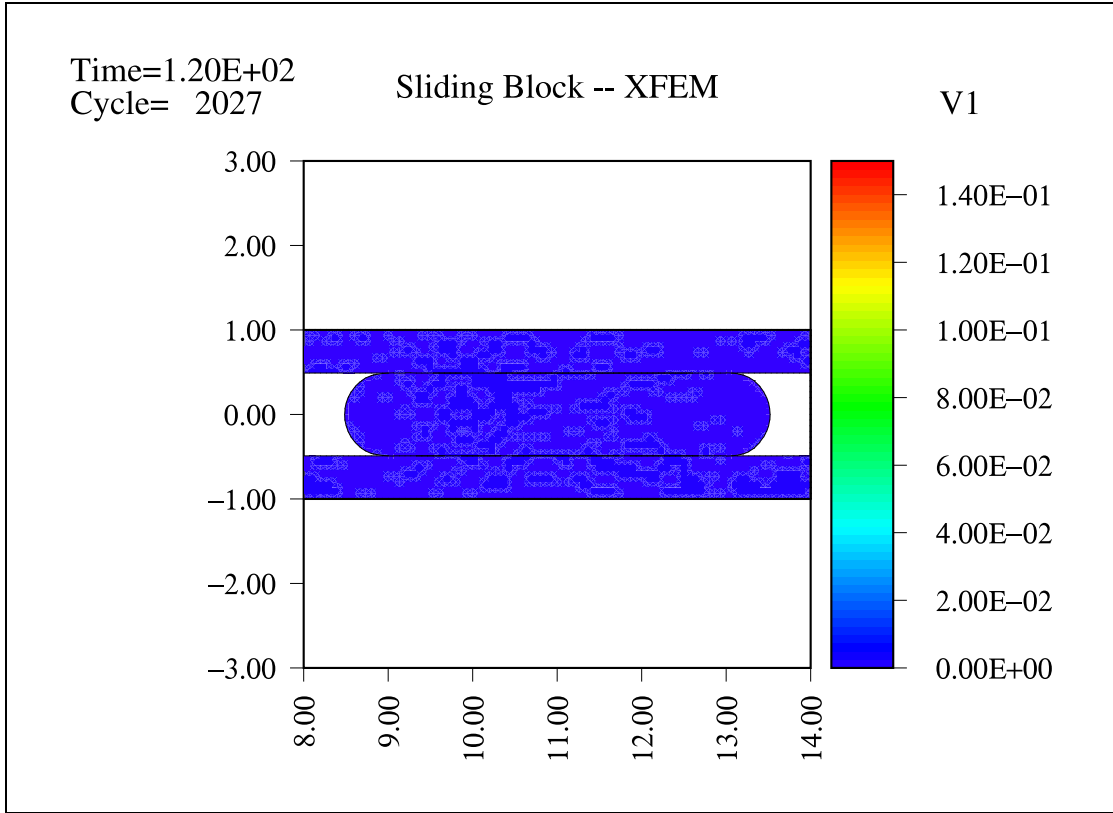


Figure V.12: Sliding Block: final condition

middle of the block stops at 11.03  $cm$ , which gives an error of

$$Error_{x_1} = \frac{11.03 \text{ cm} - 10.87 \text{ cm}}{2.84 \text{ cm}} = 5.75\% \quad (\text{V.19})$$

The average of the absolute values of the stresses at the interface (see equation (IV.61))

during the simulation from  $time = 38.7 \mu s$  until the block stopped are

$$|\bar{\sigma}_{11}| = 0.0223842 \frac{g}{cm \mu s^2} \quad (\text{V.20})$$



$$|\bar{\sigma}_{22}| = 0.0471512 \frac{g}{cm \mu s^2} \quad (V.21)$$

$$|\bar{\sigma}_{12}| = 0.0097610 \frac{g}{cm \mu s^2} \quad (V.22)$$

The stress error in direction  $x_2$  is

$$Error_{\sigma_{22}} = \frac{|\bar{\sigma}_{22}| - |\sigma_{22}|}{|\sigma_{22}|} = -0.18 \% \quad (V.23)$$

The error in the friction coefficient is

$$Error_{frctn} = \frac{\frac{|\bar{\sigma}_{12}|}{|\bar{\sigma}_{22}|} - \mu}{\mu} = 3.51 \% \quad (V.24)$$

The average contact area per side during the simulation is  $3.875 \text{ cm}^2$ , which results in the following error:

$$Error_A = \frac{3.874 \text{ cm}^2 - A}{A} = -3.67 \% \quad (V.25)$$

All the errors with respect to the analytical solutions are within a reasonable margin.

In this simulation, IIVF was set to 1% to avoid the generation of an excessive  $\epsilon_{22}$ , which results from an effect similar to the one encountered in section V.A. When the void material reaches the IIVF value, the two solid materials inside the element are considered in contact. Therefore, the velocities and accelerations of the two solid materials are coupled in the normal direction. As a result, a gap between 0% and IIVF of the volume of the nodal support is locked between the two solid materials, imposing an extra strain on the materials in the normal direction. This effect increases with the IIVF, and it is displayed in figure V.13 with an IIVF value of 5%. Figure V.14 shows how the gap is reduced when an IIVF of 1% is applied. The amount of error introduced in the simulation by the IIVF is problem dependent. In this problem, the IIVF value has to be chosen carefully. A value that is too large produces the effect observed in figure

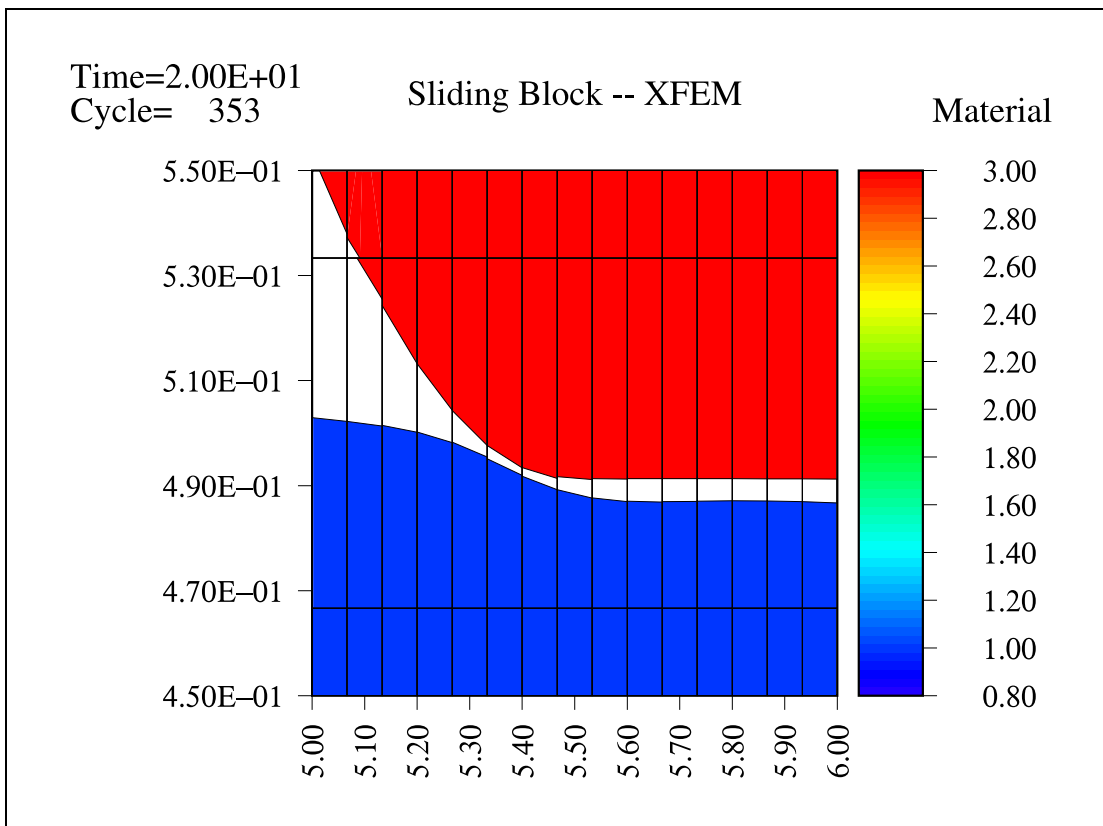


Figure V.13: Sliding Block: gap between materials with IIVF = 5%

V.13, which ultimately generates a larger friction force, while a value that is too small generates the opposite effect. In fact, a small amount of void material constantly appears and disappears between the two sliding surfaces during the simulation. Therefore, an excessively small IIVF can decouple the two solid materials in several nodal supports, and therefore, the contact areas of these nodal supports are not accounted, resulting in a smaller friction force. Future work aims to improve this aspect by compressing the void material that has reached the IIVF value out from the nodal support allowing a large IIVF to be employed in the simulation with higher accuracy. Note that figures V.13 and V.14 use a different scale for the  $x_1$ -direction and the  $x_2$ -direction. Also, that the errors

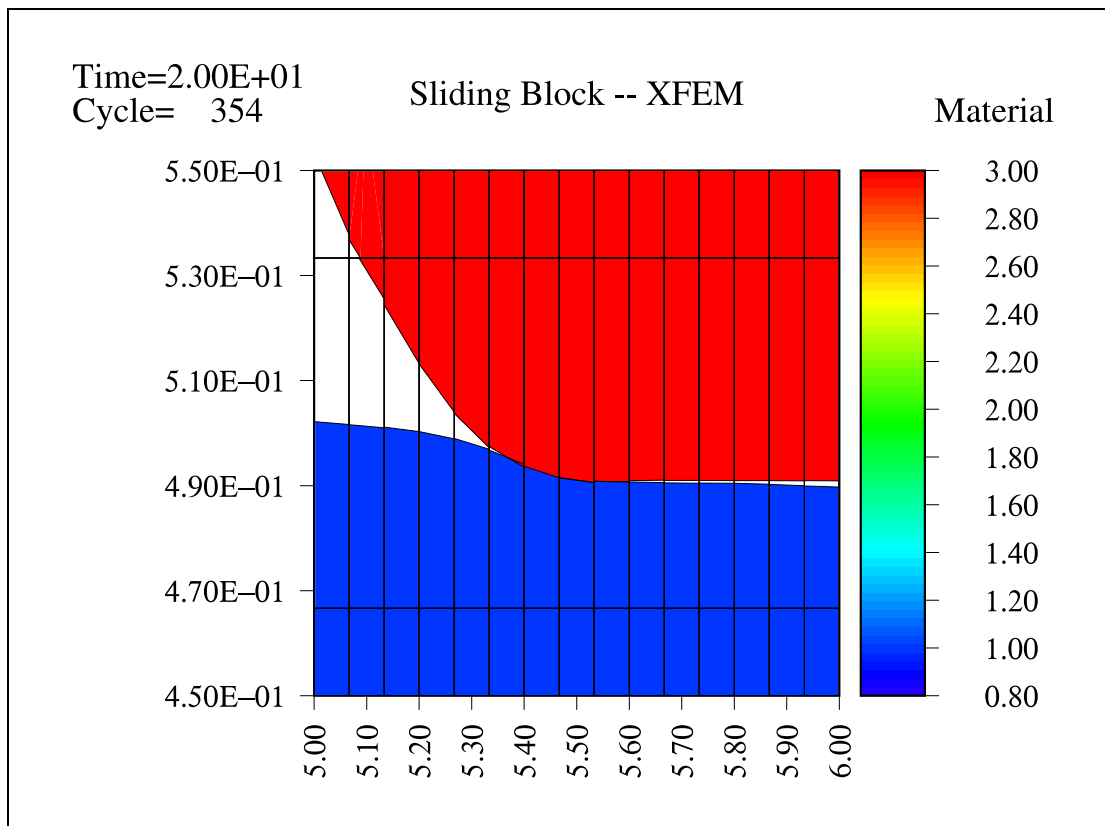


Figure V.14: Sliding Block: gap between materials with IIVF = 1%

associated with the IIVF decreases with the mesh size.

## V.C Taylor Anvil Test

In this example the X-FEM results for frictionless slip, slip with friction, and fully bonded contact are compared to the mean strain rate mixture theory and the LS-DYNA results. The problem consists of a bar made of magnesium with a diameter of  $3.0\text{ cm}$  and a height of  $6.0\text{ cm}$  striking a rigid block with an initial velocity of  $0.03\text{ cm}/\mu\text{s}$ . Figure V.15 displays the initial conditions, where the block is constrained in the normal

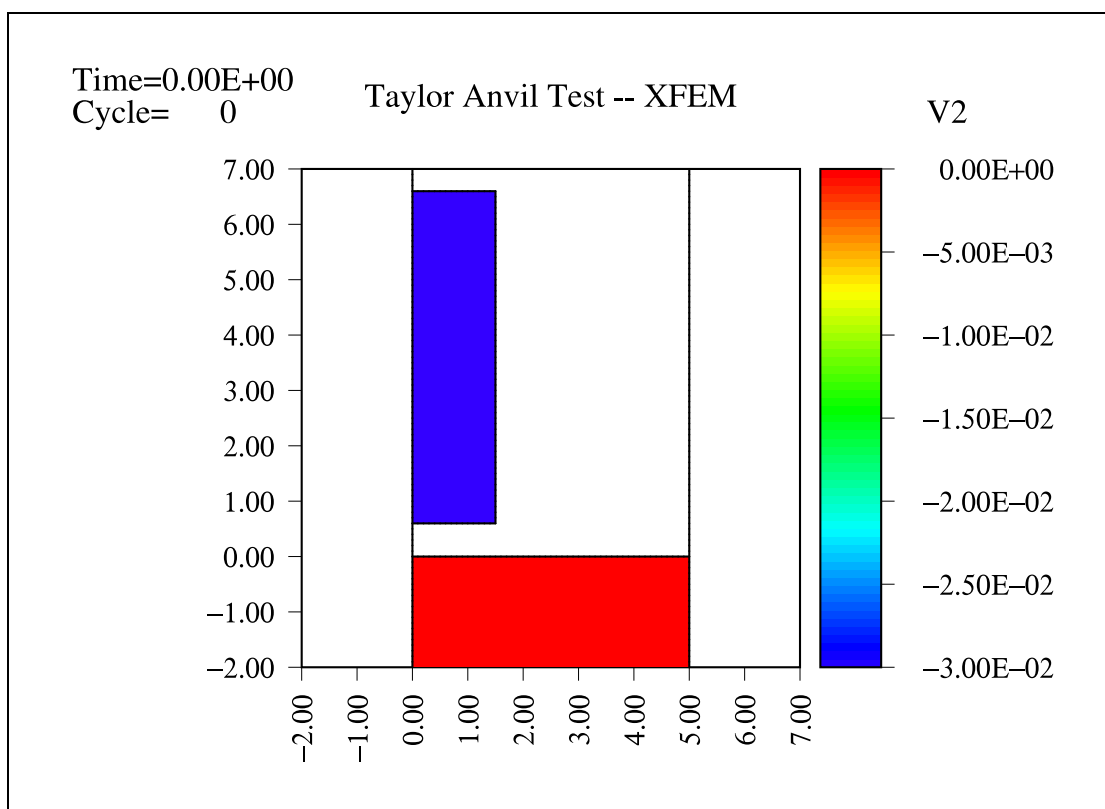


Figure V.15: Taylor Anvil Test: initial conditions

direction at the bottom boundary, symmetry is used on the left boundary, and the mesh resolution is 10 elements per centimeter in both directions. The bar is elastic-plastic with linear strain hardening, and the target behavior is purely elastic. Table V.3 shows the

materials constants, where the rigid body behavior of the block is simulated by setting

Table V.3: Taylor Anvil Test: material constants

	<b>Magnesium</b>	<b>Rigid Block</b>
$\rho$	1.74 $g/cm^3$	17.40 $g/cm^3$
$K$	0.49 $g/(cm \mu s^2)$	4.90 $g/(cm \mu s^2)$
$G$	0.16 $g/(cm \mu s^2)$	1.60 $g/(cm \mu s^2)$
$\sigma_y$	$0.69 \times 10^{-3} g/(cm \mu s^2)$	—
$H_1$	$1.0 \times 10^{-3}$	—

its constants to ten times the values of magnesium.

Figure V.16 shows the effective plastic strain in the mean strain rate mixture theory simulation. The lines drawn on the figures are contours of constant initial  $x_1$ , allowing the deformation to be visualized as with a Lagrangian mesh. The materials at the interface have not moved with respect to each other and the bar material has flowed over its lower right corner, generating a peak plastic strain of 3.00 in that region. Moreover, the overall form of the bar does not display the expected mushroom shape.

Figure V.17 displays the effective plastic strain in the X-FEM simulation where the frictionless contact is employed. The X-FEM simulation correctly predicts the mushroom shape and the relative slip between the two materials, with a peak plastic strain of 1.6. The height and bottom width of the bar in the X-FEM simulation after  $100 \mu s$  ( $80 \mu s$  since impact) are  $4.03 cm$  and  $3.89 cm$ , respectively.

Figure V.18 shows the results for the frictionless contact generated by LS-

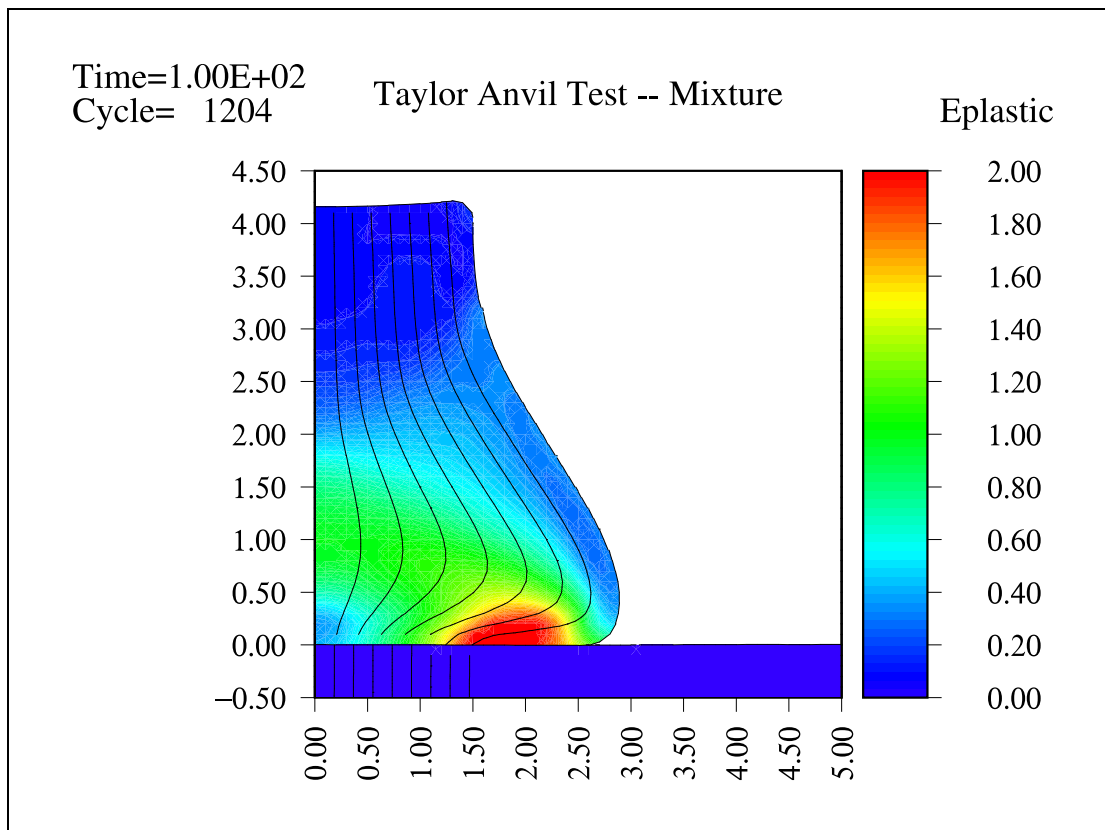


Figure V.16: Taylor Anvil Test: frictionless (Mixture Theory)

DYNA, which employed two-dimensional plane strain Lagrangian elements and the same mesh resolution as Raven. The height and bottom width of the bar in the LS-DYNA simulation after  $100\ \mu\text{s}$  are  $4.08\ \text{cm}$  and  $4.1\ \text{cm}$ , respectively. The difference between the width of the bar in the X-FEM simulation and in the LS-DYNA simulation can be attributed to better interface definition that is characteristic of Lagrangian formulations. However, the overall shape and plastic strain distribution of the two simulations agree.

Figure V.19 displays the result of the X-FEM simulation when a fully bonded contact is enforced. As expected, figure V.19 matches the image of the mixture theory simulation of figure V.16. The height and bottom width of the bar after  $100\ \mu\text{s}$  are

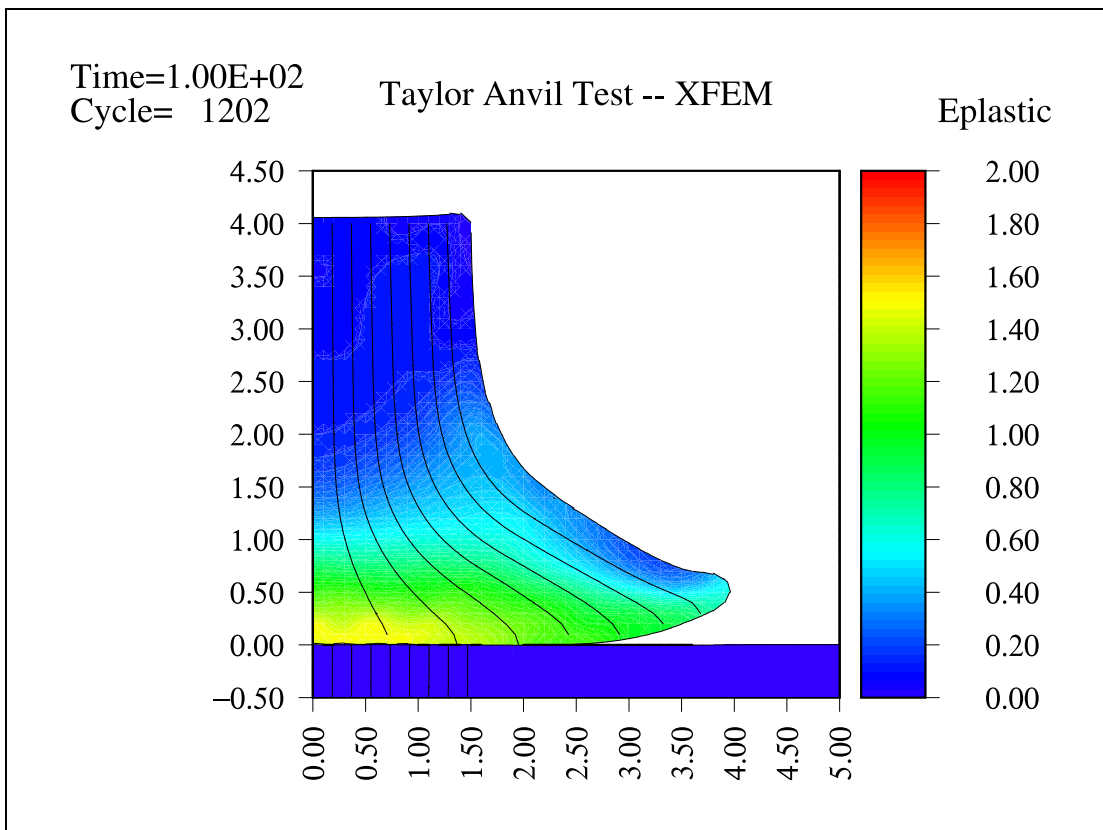


Figure V.17: Taylor Anvil Test: frictionless (X-FEM)

4.21 *cm* and 2.88 *cm*, respectively.

Figure V.20 shows the result of the LS-DYNA simulation with fully bonded contact. The height and bottom width of the bar after 100  $\mu s$  are 4.17 *cm* and 2.94 *cm*, respectively. The LS-DYNA simulation agrees with the X-FEM and the mixture theory simulations.

In the next three examples, which employ three different friction coefficients, the results of the X-FEM simulations are compared with the results obtained from LS-DYNA. A static and kinetic friction coefficient of 0.75 is employed in the simulations of figures V.21 and V.22. The X-FEM simulation of figure V.21 displays the deformed

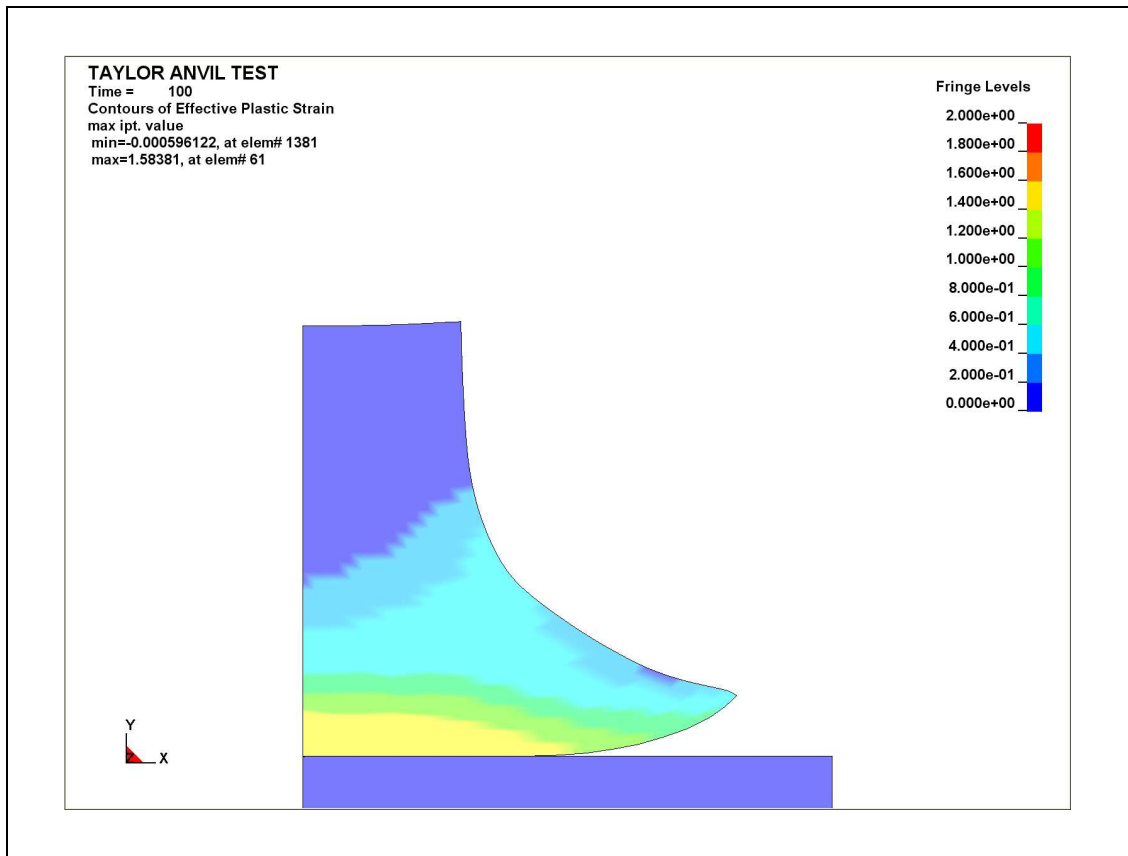


Figure V.18: Taylor Anvil Test: frictionless (LS-DYNA)

bar with a height and a bottom width of  $4.12\text{ cm}$  and  $3.10\text{ cm}$ , respectively, after  $100\ \mu\text{s}$ .

Figure V.22 shows the simulation obtained from LS-DYNA, where the height and bottom width of the bar after  $100\ \mu\text{s}$  are  $4.16\text{ cm}$  and  $3.07\text{ cm}$ , respectively.

A static and kinetic friction coefficient of 0.5 is employed in the simulations of figures V.23 and V.24. The X-FEM simulation of figure V.23 displays the deformed bar with a height and a bottom width of  $4.10\text{ cm}$  and  $3.31\text{ cm}$ , respectively, after  $100\ \mu\text{s}$ . Figure V.24 shows the results obtained from LS-DYNA, where the height and bottom width of the bar after  $100\ \mu\text{s}$  are  $4.15\text{ cm}$  and  $3.30\text{ cm}$ , respectively.

Finally, a static and kinetic friction coefficient of 0.25 is employed in the sim-



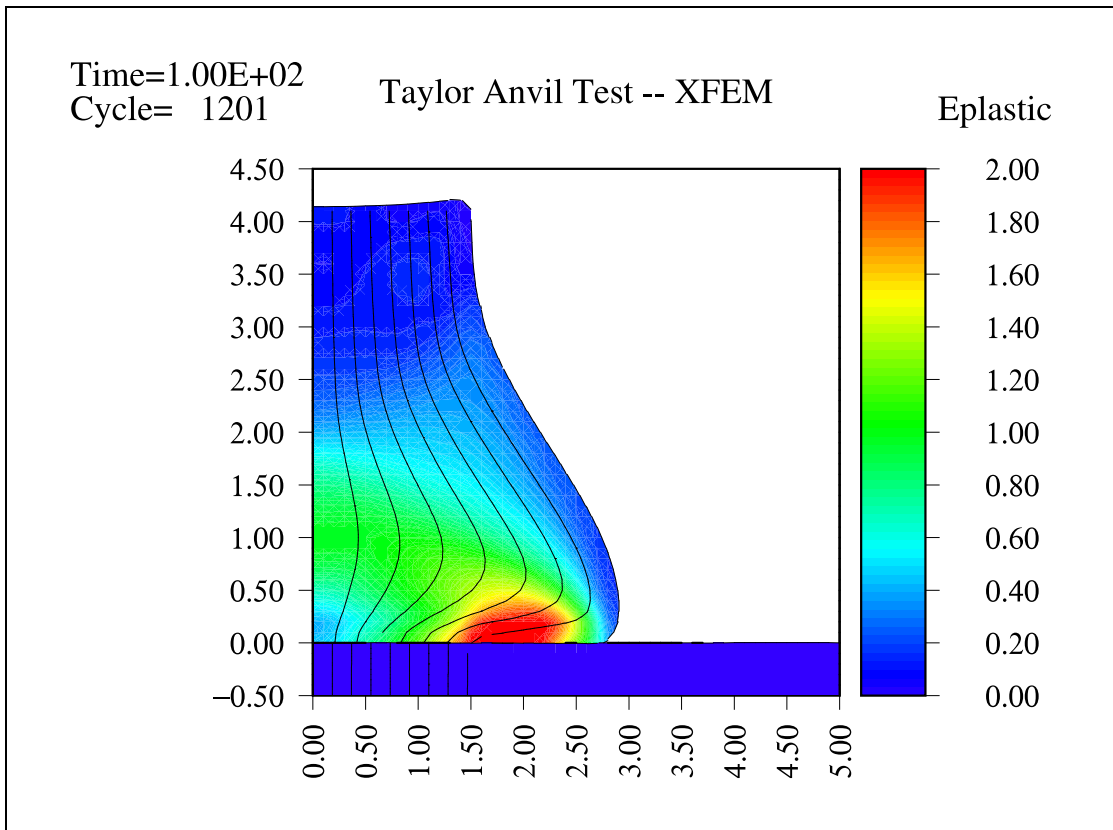


Figure V.19: Taylor Anvil Test: fully bonded (X-FEM)

ulations of figures V.25 and V.26. The X-FEM simulation of figure V.25 displays the deformed bar with a height and a bottom width of  $4.07\text{ cm}$  and  $3.61\text{ cm}$ , respectively, after  $100\ \mu\text{s}$ . Figure V.26 shows the results obtained from LS-DYNA, where the height and bottom width of the bar after  $100\ \mu\text{s}$  are  $4.12\text{ cm}$  and  $3.66\text{ cm}$ , respectively.

Note how the sequence of the figures V.19, V.21, V.23, V.25, and V.17 is in agreement with the respective contact enforcement. Moreover, the X-FEM results find a good agreement with the LS-DYNA results.

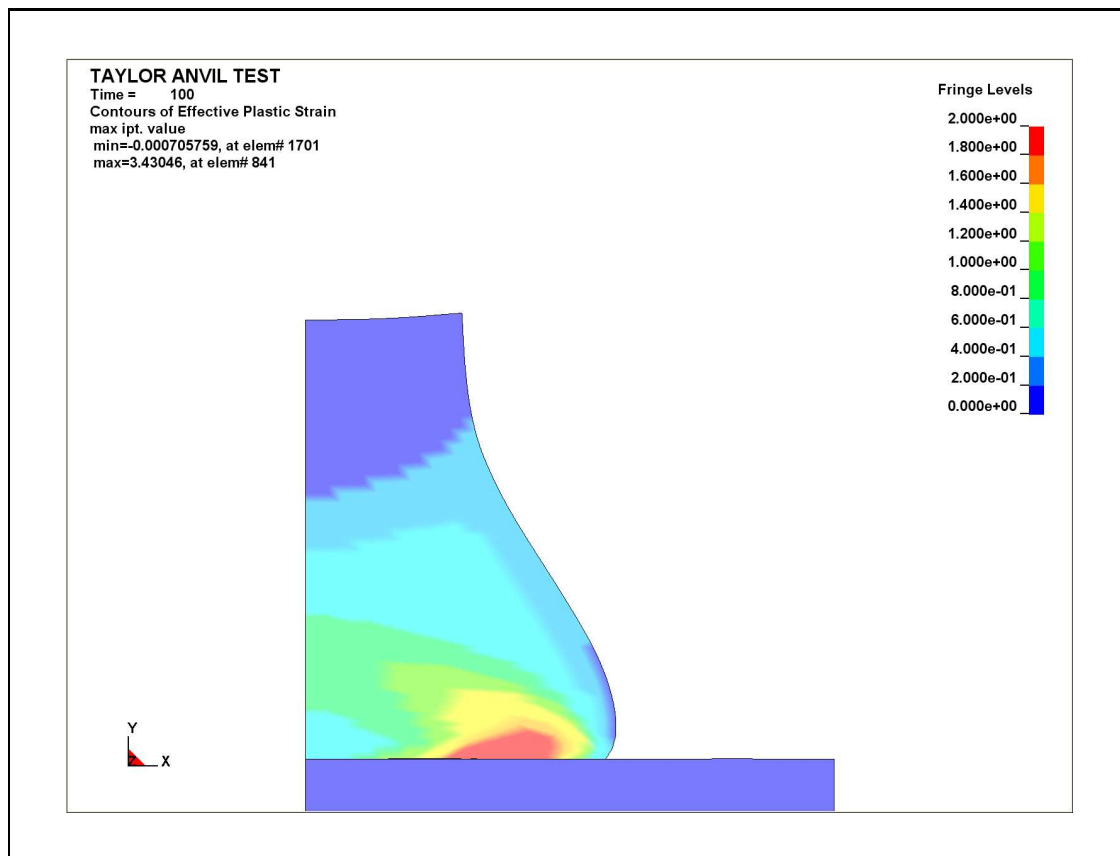


Figure V.20: Taylor Anvil Test: fully bonded (LS-DYNA)

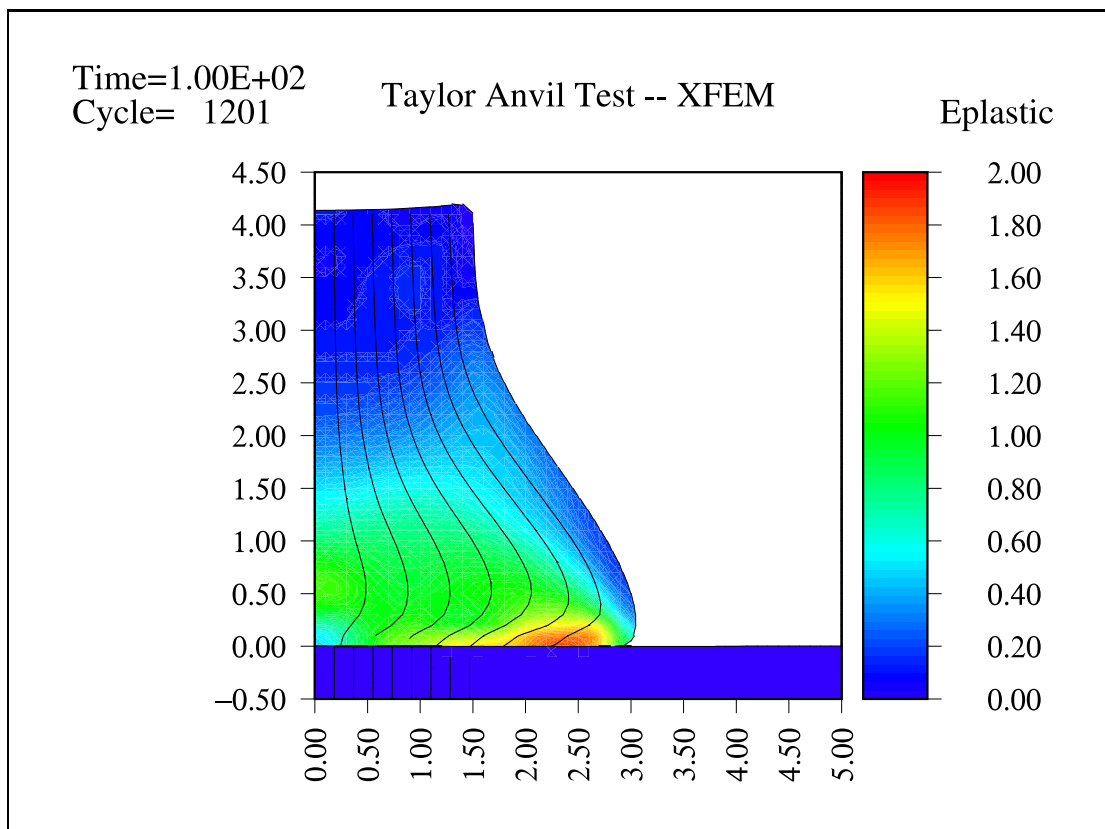


Figure V.21: Taylor Anvil Test: 0.75 friction (X-FEM)

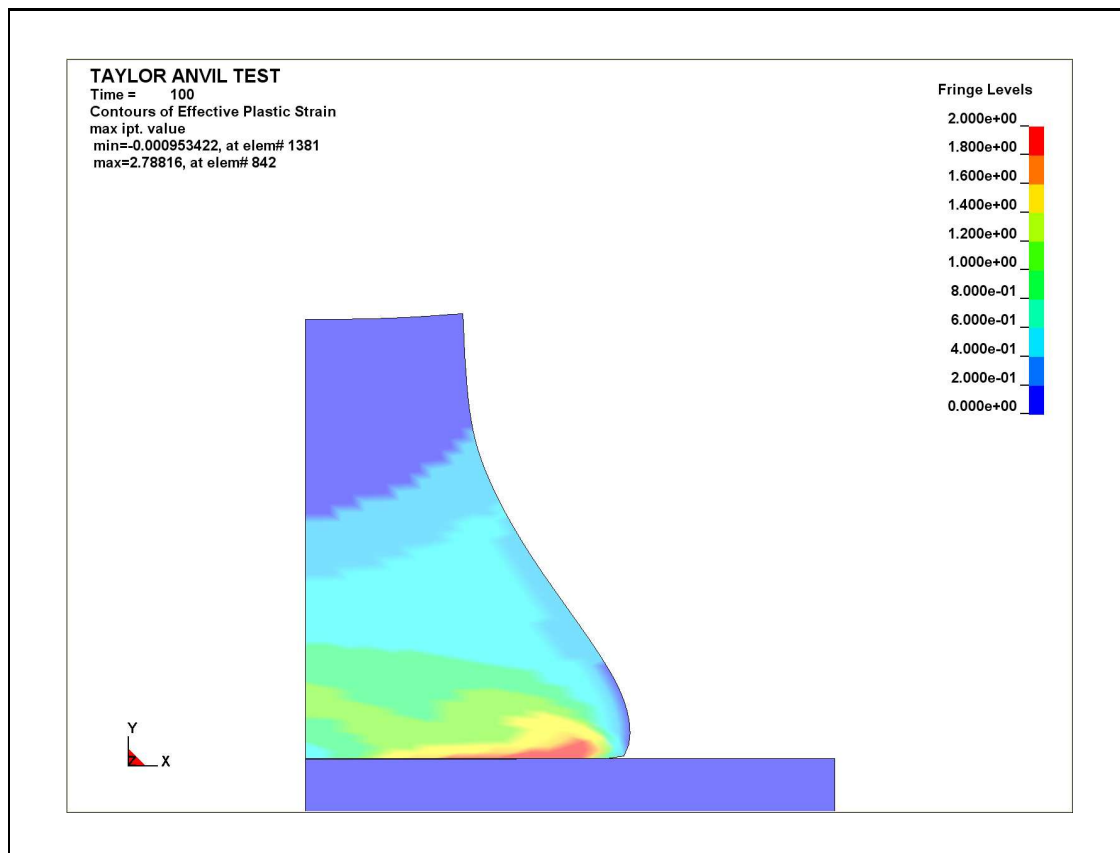


Figure V.22: Taylor Anvil Test: 0.75 friction (LS-DYNA)

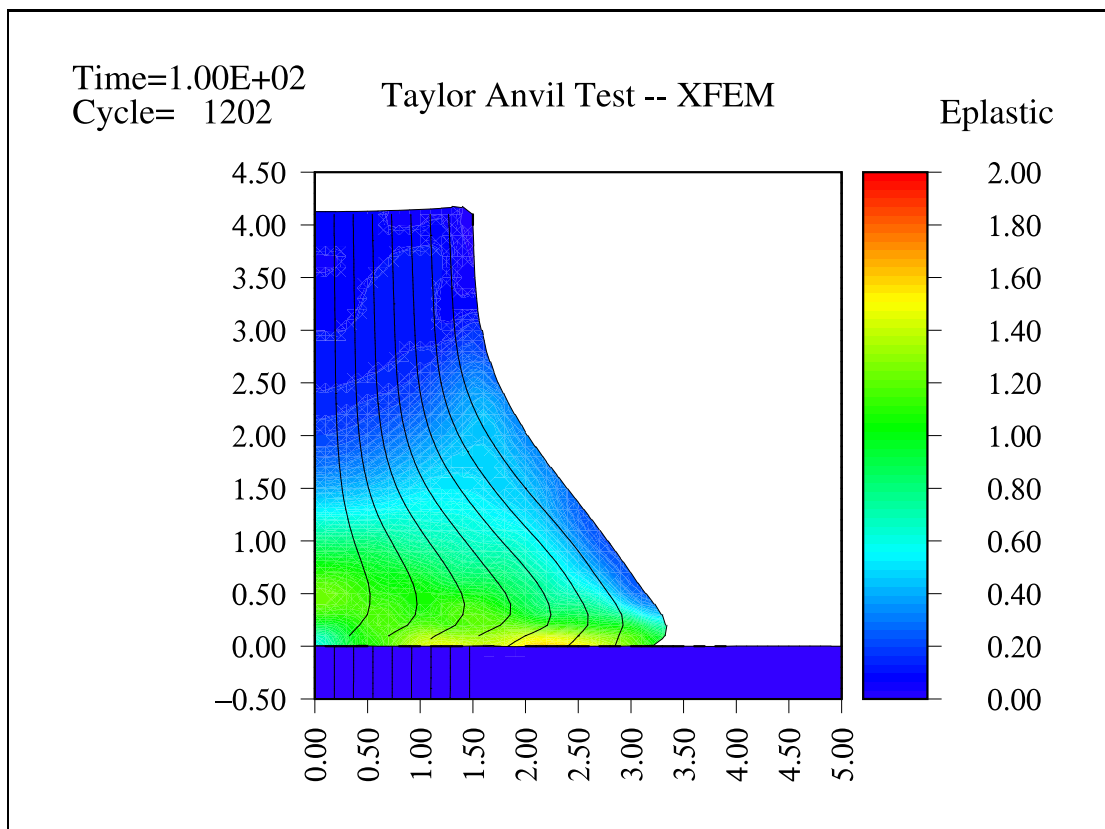


Figure V.23: Taylor Anvil Test: 0.5 friction (X-FEM)

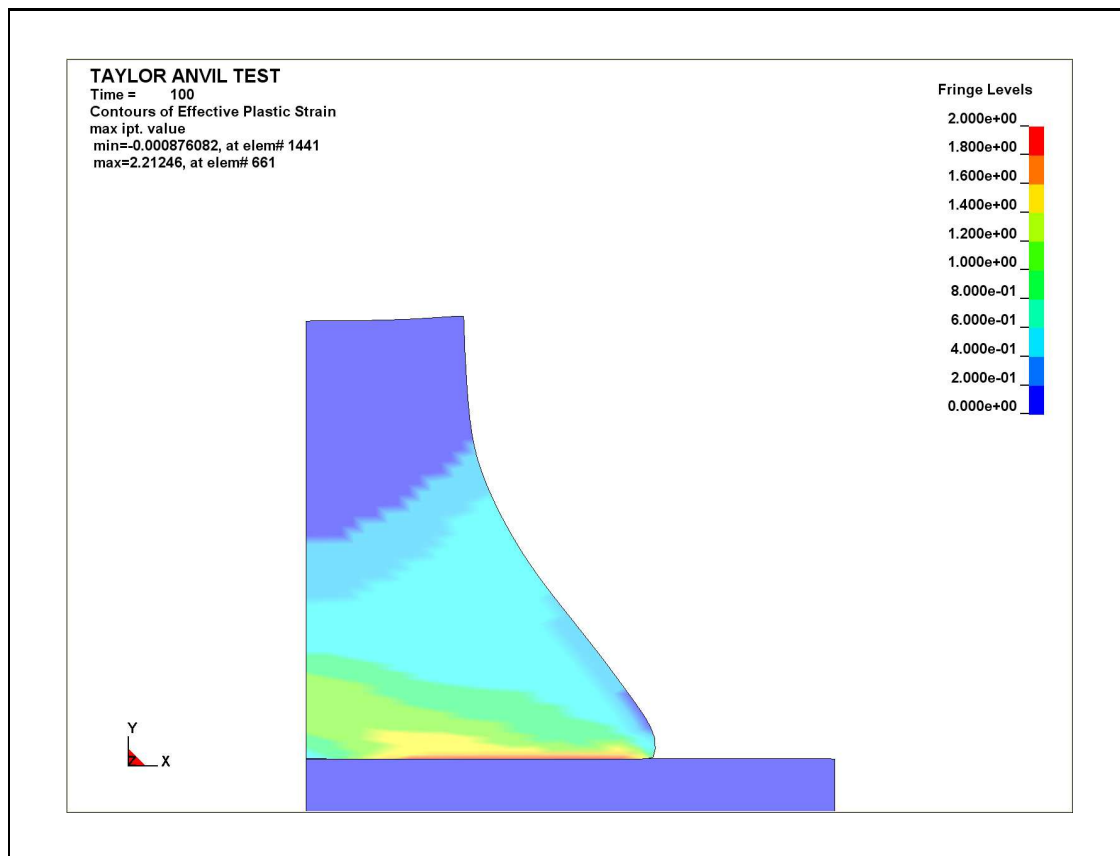


Figure V.24: Taylor Anvil Test: 0.5 friction (LS-DYNA)

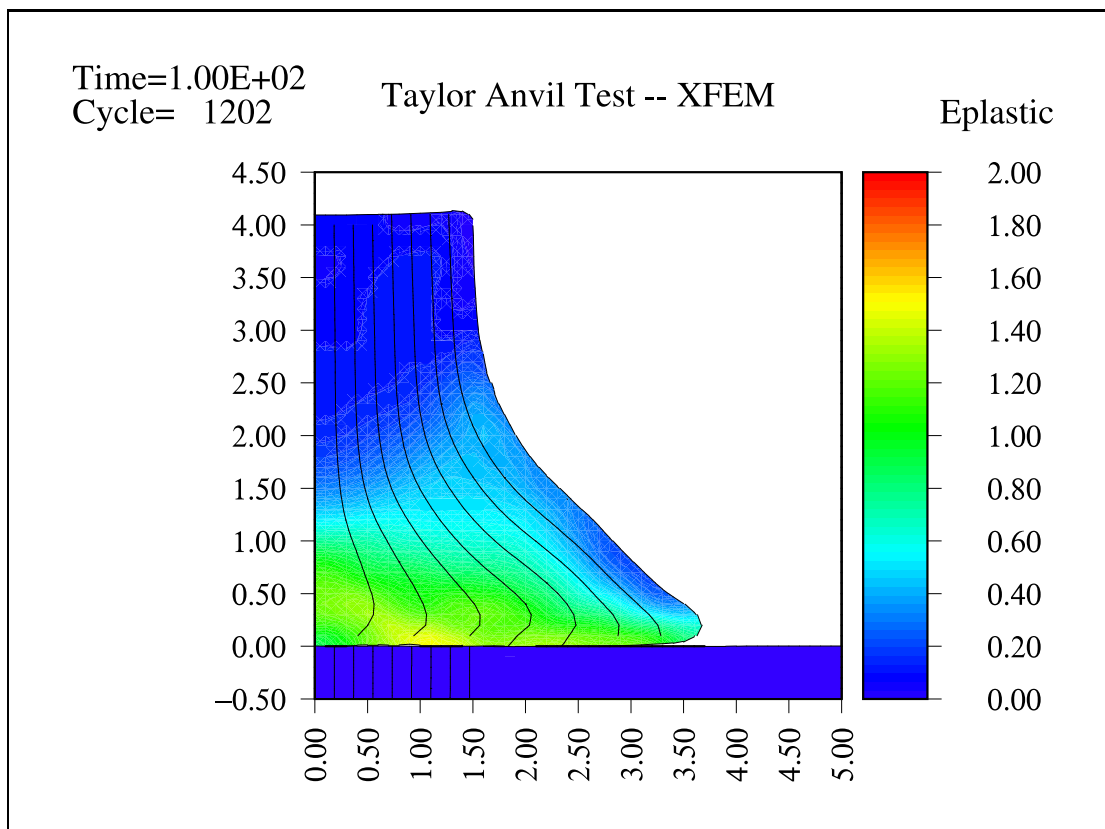


Figure V.25: Taylor Anvil Test: 0.25 friction (X-FEM)

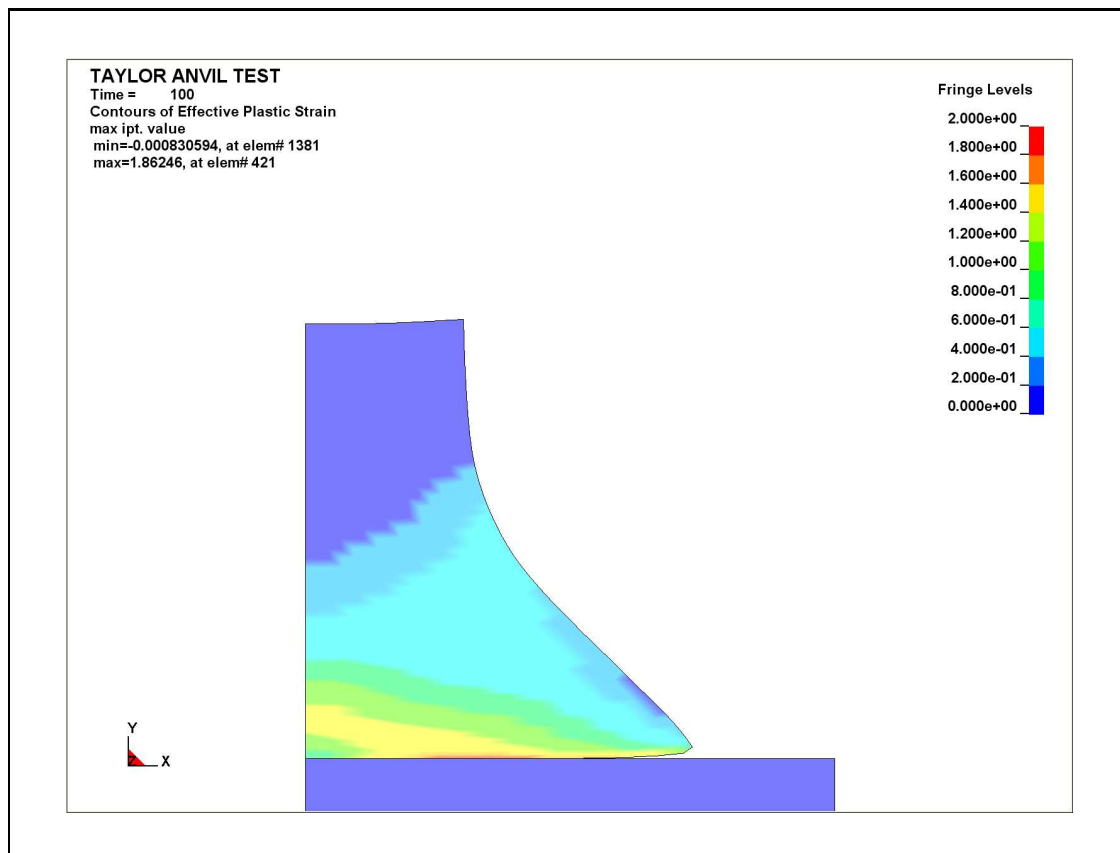


Figure V.26: Taylor Anvil Test: 0.25 friction (LS-DYNA)



## V.D Projectile Penetration

This example demonstrates the importance of accurately modeling slip with the simulation of a projectile penetrating a plate. While ballistic penetration is not frictionless, numerical friction is undesirable. The problem consists of a projectile made of steel with a diameter of  $10\text{ mm}$  and a height of  $24\text{ mm}$  striking a  $10\text{ mm}$  thick copper plate with an initial velocity of  $0.02\text{ cm}/\mu\text{s}$ . Figure V.27 shows the initial conditions, where

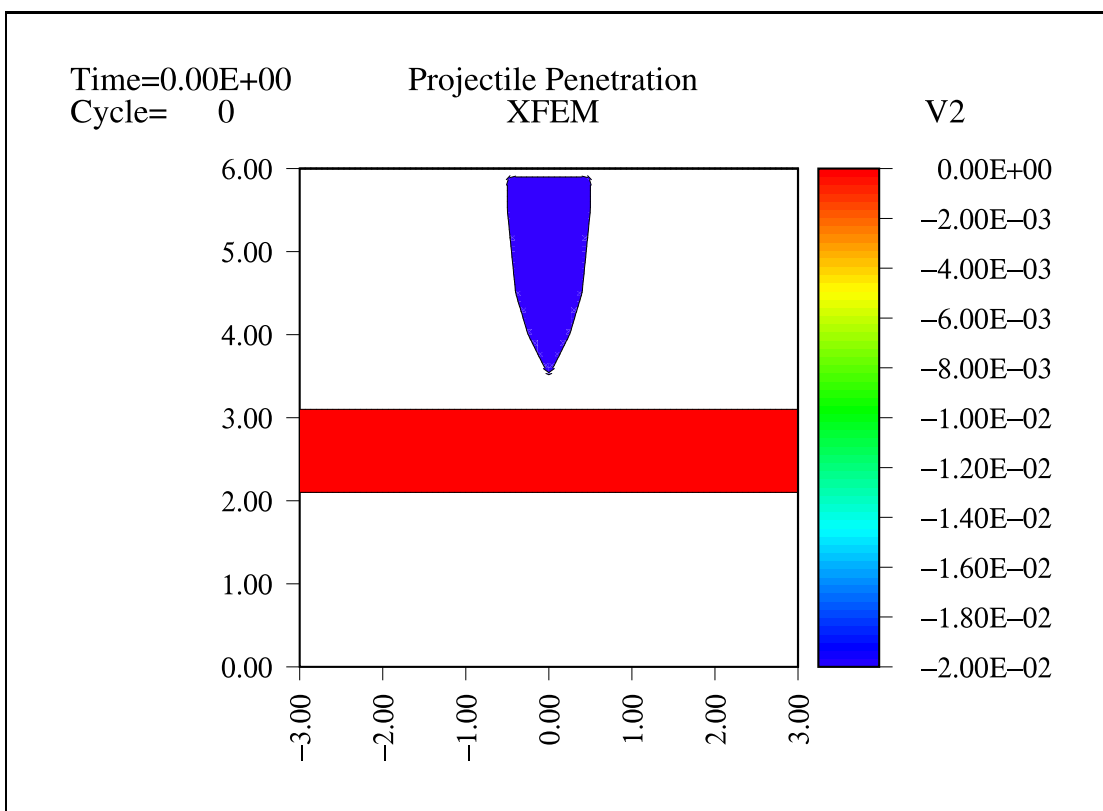


Figure V.27: Projectile Penetration: initial conditions

the left and right boundaries are constrained in the normal and tangential directions, and the mesh resolution is of 15 elements per centimeter in both directions. The behavior of the two materials is elastic-plastic with linear hardening, table V.4 summarizes the

materials constants.

Table V.4: Projectile Penetration: material constants

	<b>Steel</b>	<b>Copper</b>
$\rho$	$7.87 \text{ g/cm}^3$	$8.96 \text{ g/cm}^3$
$K$	$1.63 \text{ g/(cm } \mu\text{s}^2)$	$1.17 \text{ g/(cm } \mu\text{s}^2)$
$G$	$0.79 \text{ g/(cm } \mu\text{s}^2)$	$0.41 \text{ g/(cm } \mu\text{s}^2)$
$\sigma_y$	$2.85 \times 10^{-3} \text{ g/(cm } \mu\text{s}^2)$	$0.33 \times 10^{-3} \text{ g/(cm } \mu\text{s}^2)$
$H_1$	$1.0 \times 10^{-3}$	$1.0 \times 10^{-3}$

Figure V.28 shows the results of the mean strain rate mixture theory simulation. Note how the steel projectile does not flow past the copper plate because of the inability of the mixture theory to allow slip between the two materials.

Figure V.29 displays the results of the X-FEM simulation. In this case, the steel projectile penetrates the copper plate because the materials are allowed to slip with respect to each other, as a result, the simulation provides a more realistic solution. The difference between the mixture theory simulation of figure V.28, which is unable to allow slip, and the X-FEM simulation of figure V.29, with the frictionless slip contact enforced, is evident.

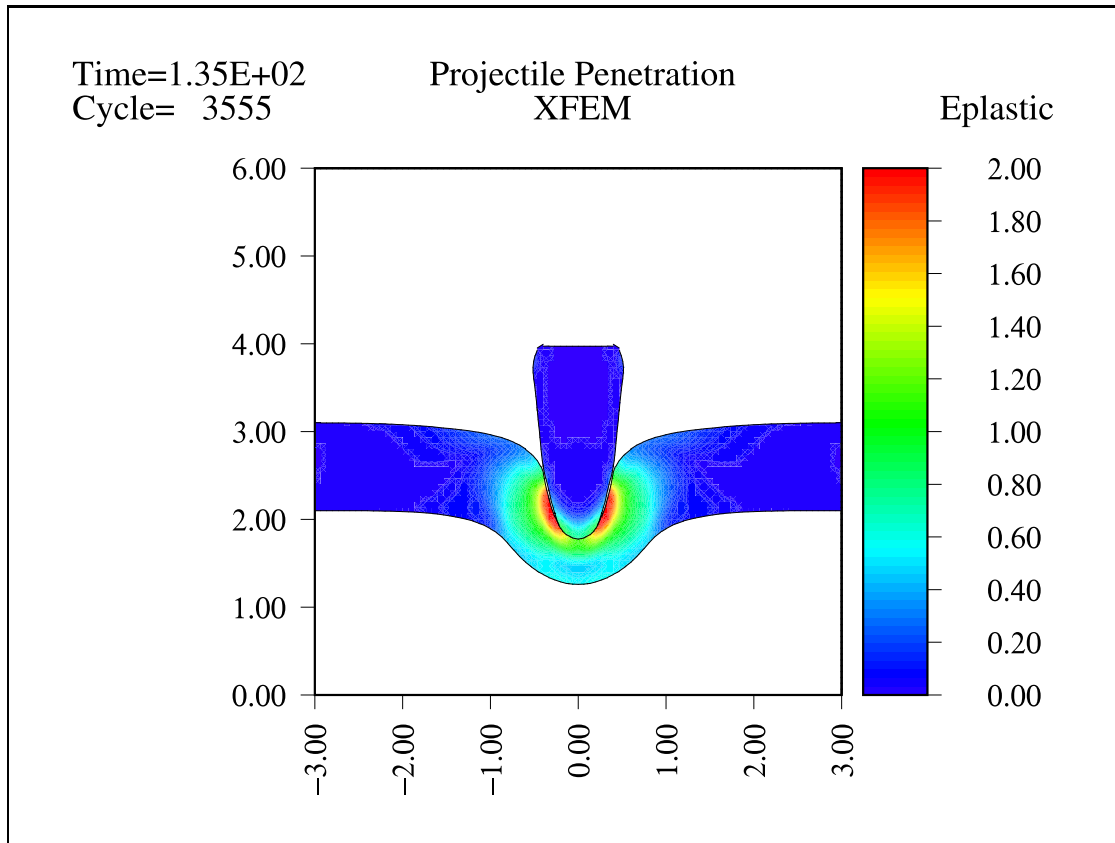


Figure V.28: Projectile Penetration (Mixture Theory)

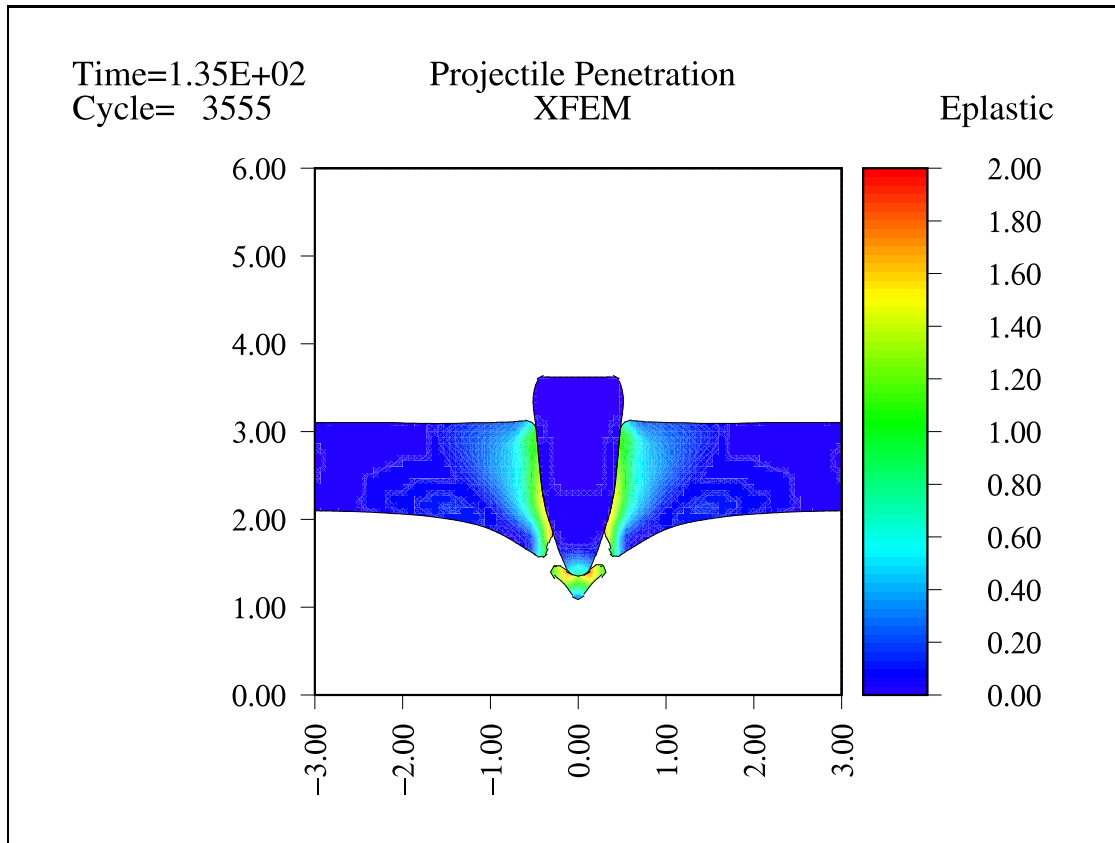


Figure V.29: Projectile Penetration (X-FEM)

## V.E High Velocity Shock Compression of a Steel Powder

The shock compression example demonstrates the robustness of the X-FEM algorithm and illustrates the energy conservation properties of the formulation. The problem consists of a  $0.2\text{ mm}$  thick rigid plate that strikes a steel powder with an initial velocity of  $0.1\text{ cm}/\mu\text{s}$ . Figure V.30 shows the initial conditions, where the mesh resolution

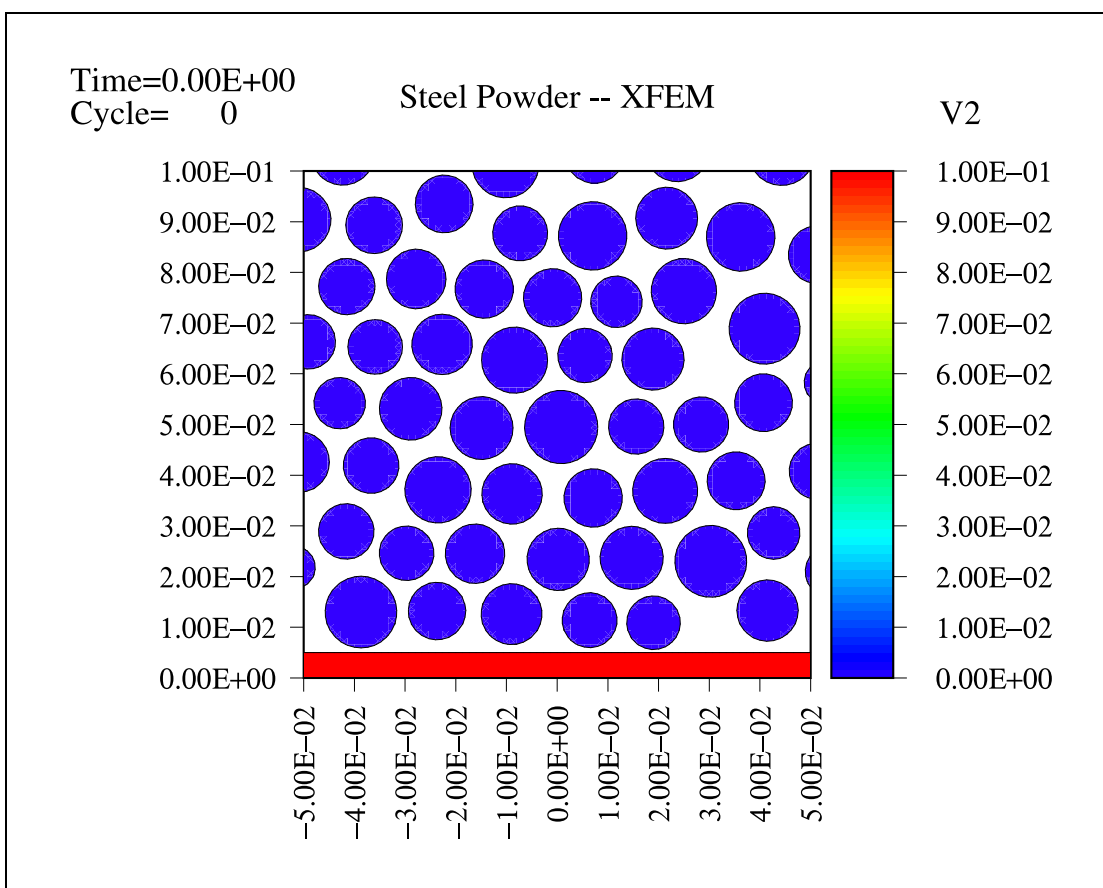


Figure V.30: Steel Powder: initial conditions

is 750 elements per centimeter in both directions. The behavior of the rigid plate is purely elastic, while the Steinberg-Guinan material model is used for the steel particles. Table V.5 shows the materials constants used in the simulation, where the left superscript \*

indicates the constants used to define the temperature  $T$  in equations (II.32) and (II.33). The procedure used to obtain  $T$  can be found in [38]. The rigid plate is simulated by setting its material constants to ten times the values of the steel particles.

Figure V.31 displays the internal energy per current volume in the materials after  $0.6 \mu s$ . The results prove the stability of the algorithm, moreover, it is noticeable

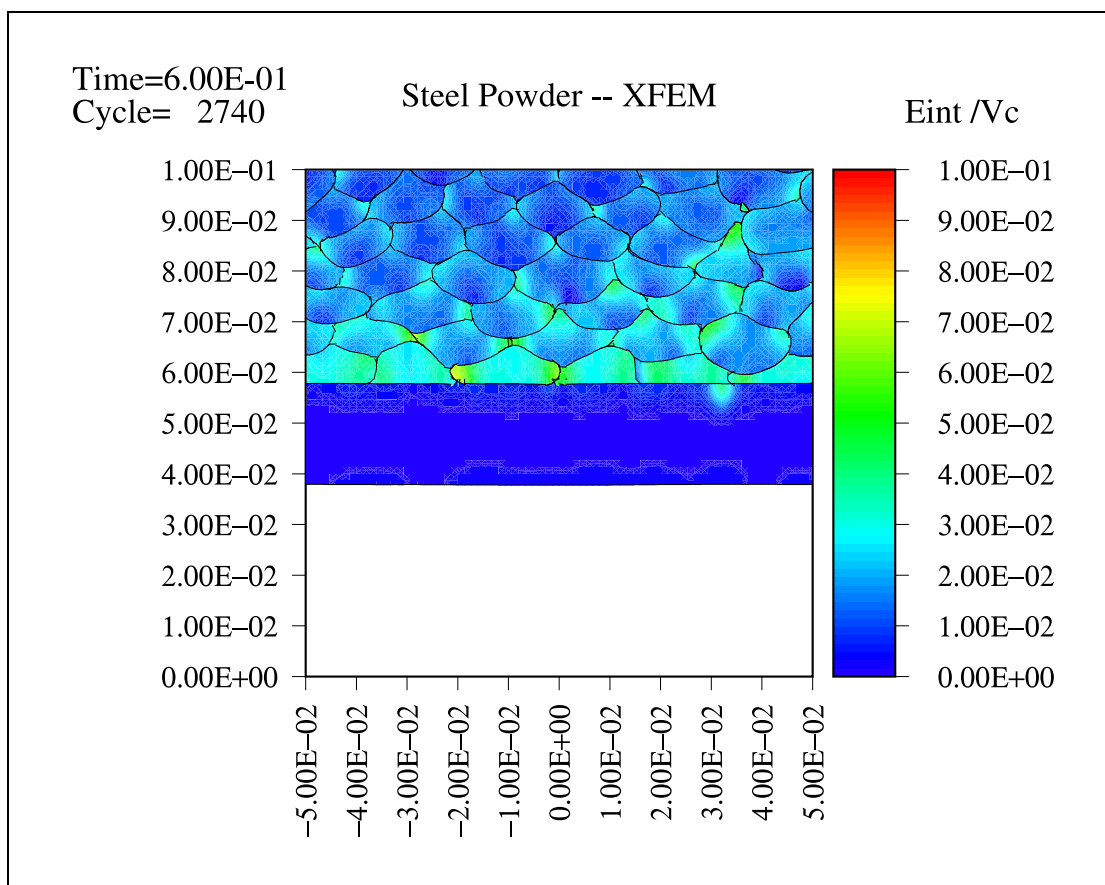


Figure V.31: Steel Powder: shock compression

how the multitude of interfaces are also handled well by the algorithm.

Figure V.32 shows the total, internal, and kinetic energies throughout the simulation. Note that the total energy decreases with time, and that the decrease in kinetic

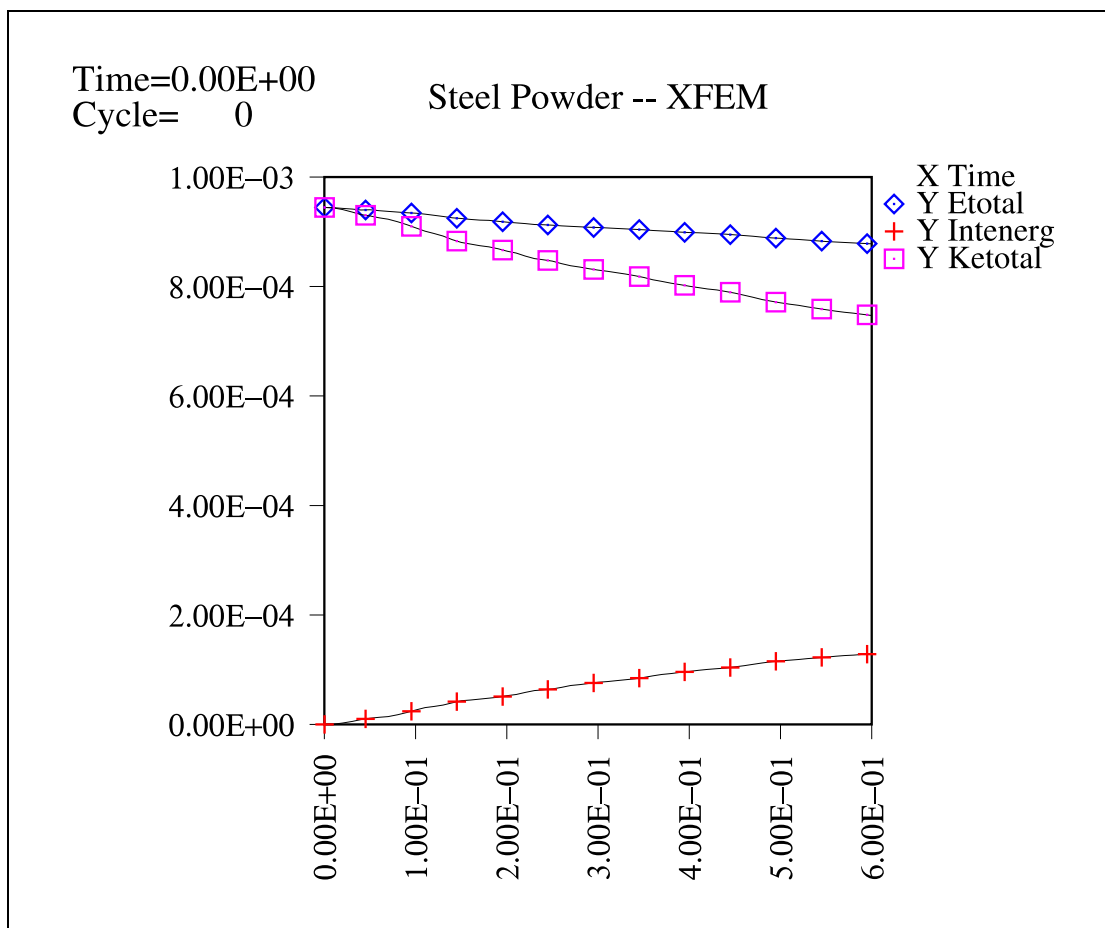


Figure V.32: Steel Powder: total, internal, and kinetic energies

energy is greater than the increase in internal energy. This loss of the kinetic energy is due to using the conservation of linear momentum for inelastic collisions to couple the velocity. The issue is not evident in the previous simulations because of the relatively small area of the interfaces. In this example, however, a large number of interfaces are present, and the problem is accentuated. The amount of kinetic energy loss decreases with the mesh size because less mass, and therefore kinetic energy, is involved in the velocity coupling. This problem is a subject for future research.

Table V.5: Steel Powder: material constants

	Steel Powder	Rigid Plate
$\rho$	$7.87 \text{ g/cm}^3$	$78.7 \text{ g/cm}^3$
$K$	$1.63 \text{ g/(cm } \mu\text{s}^2)$	$16.3 \text{ g/(cm } \mu\text{s}^2)$
$G_o$	$0.79 \text{ g/(cm } \mu\text{s}^2)$	(G) $7.9 \text{ g/(cm } \mu\text{s}^2)$
$\sigma_{y_o}$	$2.85 \times 10^{-3} \text{ g/(cm } \mu\text{s}^2)$	—
$\beta$	43.0	—
$n$	0.35	—
$^*\gamma_i$	0.0	—
$\sigma_{max}$	$2.4 \times 10^{-3} \text{ g/(cm } \mu\text{s}^2)$	—
$b$	$2.6 \text{ (cm } \mu\text{s}^2)/\text{g}$	—
$b'$	$2.6 \text{ (cm } \mu\text{s}^2)/\text{g}$	—
$h$	$-0.45 \times 10^{-3}$	—
$f$	$1.0 \times 10^{-3}$	—
$^*A$	$55.35 \text{ g/mol}$	—
$^*T_{m_o}$	2380.0 K	—
$^*\gamma_o$	1.93	—
$^*a$	0.53	—



# Chapter VI

## Conclusions and Future Work

### VI.A Summary and Conclusions

A new multi-material arbitrary Lagrangian Eulerian formulation method that can effectively simulate different types of contact has been developed. The method provides each node independent degrees of freedom for each material present in the nodal support. As a result, each material is able to move independently through the mesh. The interactions between the materials are controlled by coupling the accelerations and velocities of the multi-material nodes allowing perfectly bonded, frictionless slip, and slip with friction contact to be modeled. The effectiveness of the method has been demonstrated along with its superiority over mixture theories. Example V.A demonstrated the higher accuracy of the method with respect to the mean strain rate mixture theory upon the contact, or coupling, of two materials. In addition, the behavior of the separation condition was observed. The results of a small deformation impact simulation were successfully compared to the analytical solution of the problem. The friction algorithm

was validated in example V.B by comparing the results of the simulation to the analytical solution. In example V.C, the inability of the mixture theory to allow slip was emphasized. The results were compared to the X-FEM simulation, which did not show this limitation. Moreover, the X-FEM simulations were in good agreement with the Lagrangian simulations produced by LS-DYNA. Example V.D highlighted the importance of being able to correctly simulate the slip contact type with a projectile penetration problem. The simulations obtained from the mixture theory and the X-FEM formulation were compared, demonstrating the superiority of the new method. Finally, example V.E tested the robustness of the X-FEM formulation with good results.

The X-FEM formulation is suitable for a vast range of solid mechanics problems, however, its true effectiveness is achieved with problems presenting large deformations (e.g. materials processing).

## VI.B Future Work

The new contact algorithm is promising, however, it is at an early stage of development and the room for improvement is considerable. The following list presents a few possible areas of future research.

- A different approach to the velocity coupling algorithm of subsection IV.C.1 can improve the energy conservation of the formulation.
- The accuracy of the nodal normals in subsection IV.C.2 can be improved by volume weighting the mixed elements and intra-elements normals, such that the interface normals associated with small fragment of materials have little influence.

In addition, more representative nodal normals can be achieved by allowing all the materials inside the two elements that define an intra-element interfaces to be considered as materials at the interface.

- Projection matrices relating two non-adjacent materials can be improved to better describe the force and velocity contribution exchanged between the two materials.
- The dependency between the accuracy of the interface behavior and the IIVF value can be ameliorated by allowing the stress of the solid materials in contact to relax until the void material is completely compressed out (see examples V.A and V.B).
- The friction algorithm can be extended to include more than two solid materials per nodal support. In addition, the calculation for the contact area in the nodal support can be improved to achieve a more representative value.

# Bibliography

- [1] Lord Rayleigh (John William Strutt). *Theory of Sound*. Macmillan, London, 1877.
- [2] W. Ritz. Über eine neue methode zur lösung gewisser variations - probleme der mathematischen physik. *Journal für die Reine und Angewandte Mathematik*, 135:1–61, 1909.
- [3] B. Galerkin. Series solution of some problems of elastic equilibrium of rods and plates (in russian). *Vestnik Inzhenerov i Tekhnikov*, 19:897–908, 1915.
- [4] A. Hreinnkoff. Solution of problems in elasticity by the frame work method. *Journal of Applied Mechanics*, 8(4):169–175, December 1941.
- [5] R. Courant. Variational methods for the solution of problems of equilibrium and vibrations. *Bulletin of the American Mathematical Society*, 49:1–23, 1943.
- [6] M. Turner, R. Clough, H. Martin, and L. Topp. Stiffness and deflection analysis of complex structures. *Journal of Aeronautical Sciences*, 23(9):805–824, September 1956.
- [7] R. Clough. The finite element method in plane stress analysis. In *2nd Conference in Electronic Computation*, pages 345–378. American Society of Civil Engineers, Pittsburgh, PA, September 1960.
- [8] G. Maenchen and S. Sack. The tensor code. *Methods in Computational Physics*, pages 181–210, 1964.
- [9] M. Wilkins. Calculation of elastic-plastic flow. *Methods in Computational Physics*, pages 211–263, 1964.
- [10] Matrix methods in structural mechanics (affdl-tr-66-80). Wright-Patterson Air Force Base, Dayton, OH, 1965.
- [11] L. Malvern. *Introduction to the mechanics of a continuous medium*. Prentice-Hall, Upper Saddle River, NJ 07458, 1969.
- [12] B. van Leer. Towards the ultimate conservative difference scheme iv: A new approach to numerical convection. *Journal of Computational Physics*, 23:276–299, 1977.

- [13] A. Chorin, T. Hughes, M. McCracken, and J. Marsden. Product formulas and numerical algorithms. *Communications on Pure and Applied Mathematics*, 31:205–256, 1978.
- [14] D. Steinberg and M. Guinan. A high strain-rate constitutive model for metals. *Technical Report UCRL-80465, Lawrence Livermore Laboratories*, 1978.
- [15] D. Steinberg, S. Cochran, and M. Guinan. A constitutive model for metals applicable at high-strain rate. *Journal of Applied Physics*, 51(3):1498–1504, March 1980.
- [16] D. Youngs. Time dependent multi-material flow with large fluid distortion. *Numerical Methods for Fluid Dynamics*, pages 273–285, 1982.
- [17] K. Johnson. *Contact mechanics*. Cambridge University Press, Trumpington Street, Cambridge CB2 1RP, 1985.
- [18] D. Benson. Computational methods in lagrangian and eulerian hydrocodes. *Computer Methods in Applied Mechanics and Engineering*, 99:235–394, 1992.
- [19] Z. Zhong. *Finite element procedures for contact-impact problems*. Oxford University Press, Walton Street, Oxford OX2 6DP, 1993.
- [20] D. Benson. A multi-material eulerian formulation for the efficient solution of impact and penetration problems. *Computational Mechanics*, 15:558–571, 1995.
- [21] D. Benson. A mixture theory for contact in multi-material eulerian formulations. *Computer Methods in Applied Mechanics and Engineering*, 140:59–86, 1997.
- [22] M. Fleming, Y. Chu, B. Moran, and T. Belytschko. Enriched element-free galerkin methods for crack tip fields. *International Journal for Numerical Methods in Engineering*, 40:1483–1504, 1997.
- [23] J. Glimm, M. Graham, J. Grove, X. Li, T. Smith, D. Tan, F. Tangerman, and Q. Zhang. Front tracking in two and three dimensions. *Computers and Mathematics with Applications*, 35(7):1–11, 1998.
- [24] Y. Krongauz and T. Belytschko. Efg approximation with discontinuous derivatives. *International Journal for Numerical Methods in Engineering*, 41:1215–1233, 1998.
- [25] W. Rider and D. Kothe. Reconstructing volume tracking. *Journal of Computational Physics*, 141:112–152, 1998.
- [26] T. Belytschko and T. Black. Elastic crack growth in finite elements with minimal remeshing. *International Journal for Numerical Methods in Engineering*, 45(5):601–620, 1999.
- [27] J. Heinrich and D. Pepper. *The intermediate finite element method: fluid flow and heat transfer applications*. Taylor and Francis, first edition, 1999.
- [28] N. Moes, J. Dolbow, and T. Belytschko. A finite element method for crack growth without remeshing. *International Journal for Numerical Methods in Engineering*, 46:131–150, 1999.

- [29] T. Belytschko, W. Liu, and B. Moran. *Nonlinear finite elements for continua and structures*. Wiley, 605 Third Avenue, New York, NY 10158-0012, USA, 2000.
- [30] J. Glimm, J. Grove, X. Li, and D. Tan. Robust computational algorithms for dynamic interface tracking in three dimensions. *SIAM Journal of Scientific Computing*, 21(6):2240–2256, 2000.
- [31] N. Sukumar, N. Moes, B. Moran, and T. Belytschko. Extended finite element method for three-dimensional crack modeling. *International Journal for Numerical Methods in Engineering*, 48(11):1549–1570, 2000.
- [32] K. Huebner, D. Dewhurst, D. Smith, and T. Byrom. *The finite element method for engineers*. Wiley-Interscience, fourth edition, 2001.
- [33] N. Sukumar, D. Chop, N. Moes, and T. Belytschko. Modeling holes and inclusions by level sets in the extended finite-element method. *Computer methods in Applied Mechanics and Engineering*, 190(46–47):6183–6200, 2001.
- [34] D. Benson. Volume of fluid interface reconstruction methods for multi-material problems. *Applied Mechanics Reviews*, 55(2):151–165, 2002.
- [35] S. Osher and R. Fedkiw. *Level set methods and dynamic implicit surfaces*. Springer-Verlag, 2002.
- [36] D. Benson and S. Okazawa. Contact in a multi-material eulerian finite element formulation. *Computer methods in applied mechanics and engineering*, 193:4277–4298, 2004.
- [37] J. Chessa and T. Belytschko. Arbitrary discontinuities in space-time finite elements by level sets and x-fem. *International Journal for Numerical Methods in Engineering*, 61(15):2595–2614, 2004.
- [38] Livermore Software Technology Corporation. Ls-dyna keyword user’s manual, version 971. *Technical report*, 2006.
- [39] J. Song, P. Areias, and T. Belytschko. A method for dynamic crack and shear band propagation with phantom nodes. *International Journal for Numerical Methods in Engineering*, 67(6):868–893, 2006.
- [40] E. Vitali and D. Benson. An extended finite element formulation for contact in multi-material arbitrary lagrangian-eulerian calculations. *International Journal for Numerical Methods in Engineering*, 67(10):1420–1444, 2006.